EFFECTS OF MULTIDIMENSIONAL POTENTIAL-ENERGY SURFACE TOPOLOGY ON THE UNIMOLECULAR DISSOCIATION OF VINYL BROMIDE

By

ASIF RAHAMAN

Bachelor of Science
Calcutta University
Calcutta, India
1991

Master of Science
Indian Institute of Technology
Kanpur, India
1993

Submitted to the Faculty of the
Graduate College of the
Oklahoma State University
in partial fulfillment of
the requirements for
the Degree of
DOCTOR OF PHILOSOPHY
July, 2000

EFFECTS OF MULTIDIMENSIONAL POTENTIAL-ENERGY SURFACE TOPOLOGY ON THE UNIMOLECULAR DISSOCIATION OF VINYL BROMIDE

Thesis Approved:

Thesis Advisor

Dean of Graduate College

ACKNOWLEDGEMENTS

I wish to express my sincere appreciation to my research advisor, Dr. Lionel M. Raff for his guidance, patience and inspiration during my research work. His brilliant ideas and ability to explain the complex scientific subject will always be a treasure to me. I am grateful to have an opportunity to study under his supervision.

I would also like to extend my sincere appreciation to Dr. P. J. Devlin, Dr. D. L. Thompson, Dr. P. W. Westhaus and Dr. N. Kotov for serving my committee and taking time to read this thesis, and for their invaluable remarks, guidance, assistance and encouragement.

Moreover, I wish to express my sincere gratitude to my friends for their warm friendship, discussions and suggestions

I would also like to give my special appreciation to my mom and family members for their support and encouragement for all the time.

Finally, I would like to thank the Department of Chemistry for supporting during my studies.

TABLE OF CONTENTS

LIST OF TABLES

LIST OF FIGURES

CHAPTER I

INTRODUCTION

The theoretical investigation of reaction dynamics and spectroscopy of molecular systems requires the knowledge of potential energy-surface (PES). For two and three-atom molecules an accurate PES can be constructed using currently available *ab initio* theories provided proper basis sets are used. For larger molecules, the calculation of an accurate potential-energy surface is very difficult, primarily because of the dimensionality of the surface which precludes the possibility of high level of electronic structure calculations for a sufficiently large number of configurations to obtain a global representation of the PES that includes all the open reaction channels.

The level of difficulty associated with obtaining a global potential-energy surface for polyatomic systems has led to many attempts to predict reaction mechanisms based on the relative energies of stationary points on the surface without exploring the global potential-energy surface. These points are few in numbers. So their energies can be calculated with accurate configuration interaction (CI) or forth-order Möller-Plesset perturbation (MP4) theory with large basis sets. By assuming that a reaction follows the minimum-energy path, one can infer reaction mechanisms from the knowledge of stationary-points on the surface without performing any trajectory or semiclassical

scattering calculations on the global potential-energy surface. For thermal decompositions, this assumption is quite accurate. But for reactions occurring at energies well above the potential barrier, the major reaction pathways often do not follow the minimum-energy paths. Bakkas *et al.*[1] performed *ab initio* calculations on methanol-water dimer at both self-consistent field (SCF) and MP2 level of theory using 6-31G** basis sets. The results suggest that CH_3OH--OH_2 and CH_3OH--HOH are nearly isoenergic. So both complexes should be present in matrix isolation studies. However, IR absorption studies indicate that only the first complex is present in the matrix. Wladkowski *et al.*[2] investigated the proton transfer dynamics for CH_3OHF^- system using *ab initio* calculation with as many as 482 atomic orbitals. The stationery-point geometries were determined at the MP2 level whereas the energies were determined using MP4, configuration interaction (CI) and coupled cluster singles and doubles methods. Walch[3,4] used the complete active space self-consistent field (CASSCF) method to locate the stationery points followed by internally contracted CI calculations to determine the mechanisms and barrier heights for reaction between CH_3 + OH [3] and NH_2 + NO [4] systems. Robertson, Wardlaw and Hirst[5] have studied the minimum-energy pathway for the dissociation of C_2H_6 into two CH_3 radical using CI methods. Mebel *et al.*[6] studied the bimolecular reaction between NH and NO_2 using the UMP2 method to locate the stationery point geometries and CI methods to calculate the energies. They used 6-31G** basis sets for their calculations. The results indicate that oxygen-atom migration is a high barrier process. Consequently, both reaction channels are inferred to involve formation of the $HNNO_2$ complex. Maluendes *et al.*[7] used MP2-MP4 and quadratic CI methods to investigate the mechanism for the $C_3H^+ + H_2$ reaction. Dunning's[8] triple zeta (5s3p/3s)

valence contraction of Huzinaga's[9] (10s6p/5s) basis set was used for both the carbon and hydrogen atom with an added single polarization function. The results indicate that the H_2CCCH^+ product rearranges to cyclic $C_3H_3^+$ via two pathways which then dissociates to $C_3H_2^+$. H. Jensen, Morokuma and Gordon[10] studied the decomposition of ethylene using *ab initio* methods. They determined the molecular geometries of C_2H_4 at the stationery points at MP2 level and energies at these points at MP4 level of theory with 6-31(d,p) and 6-31G** basis sets. The three-center H_2 elimination channel leading to H_2 and vinylidene was found to have a barrier pf 93.8 kcal/mol. No transition state was found for four-center H_2 elimination. The barrier for the overall reaction involving 1,1-H_2 elimination followed by a hydrogen atom transfer from vinylidene was determined to be 109.5 kcal/mol which was in agreement with the experimental observations reported by Okabe and McNesby[11] and by Balko *et al.*[12] Therefore, they predicted that the H_2 dissociation mechanism is an α, α process. Riehl and Morokuma[13] used quadratic single and double CI methods which also included a triple contribution, with 6-31(d,p) basis sets at geometries obtained from MP2 calculations to examine the mechanism for decomposition of vinyl chloride. The calculated barriers for α,α HCl and α,β HCl elimination were 69.1 kcal/mol and 77.4 kcal/mol respectively. The α,α H_2 elimination has a barrier of 97.2 kcal/mol. No transition state was found for four-center H_2 elimination. Consequently, the energetically favored channel decomposition channels are, in the order of importance, α,α HCl and α,α H_2 . These results are in agreement with recent experiments[14-16] which showed that the large majority of the HCl product is formed by three-center elimination.

Another approach to develop the global potential-energy surface uses parameterized functional forms justified by physical and chemical considerations to fit thermochemical, spectroscopic, structural and kinetic data. This process works well provided the critical potential barriers of reactions are accurately estimated from measured activation energies. Sewell and Thompson[17] used this method to study the dissociation of activated 2-chloroethyl radicals. They used a PES which is a sum of Morse-type potentials for bond stretching, harmonic potentials for angle bending which are attenuated to zero whenever one of the bonds forming the angle is dissociated and a parameterized six-term cosine series for torsional forces. Classical trajectory calculations with this potential indicate that the C-H and C-Cl bond fission processes are statistical in nature. Marks[18] investigated –N=C > –C≡N isomerization in HD_2CNC. Only small mode-specific rate enhancement effects were found. Rice and Thompson[19] studied the dissociation of CH_3NO_2 to yield CH_3 + NO_2 and CH_3O + NO. The global PES is represented as a summation of channel potentials where each term represents one of the asymptotic limits CH_3NO_2 , CH_3 + NO_2 and CH_3O + NO. These channel potentials are connected by switching functions with parameters that control the barrier height for the reaction. Since the barrier height for the reaction was unknown, they studied the decomposition reactions as a function of barrier heights. The same method has been employed to obtain the PES for the study various other reactions[20-23]. Extensive calculations on the gas phase and matrix-isolated reaction dynamics have been conducted for the unimolecular decomposition of 1,2-difluoroethane and the bimolecular reaction between F_2 and ethylene[24-30] using the above method to obtain the PES.

The most successful approach to obtain a fairly accurate PES for polyatomic systems is a combination of the above methods. This method involves the use of high level *ab initio* calculations to obtain transition-state geometries, frequencies and energies. Cho *et al.*[31] Vande Linde and Hase[32,33], and Hase and Cho[34] have used this combined approach to obtain the PES for the [Cl^- ---CH_3Cl] system. The PES was developed by fitting the data obtained from *ab initio* calculations at HF level with 6-31G* basis sets and experimental data with bond-order-bond-energy type functions connected by appropriate switching functions. Trajectory studies on this surface indicate that the system behaves non-statistically and that there are excessive barrier recrossings. The intramolecular dynamics are not in accord with transition-state theory assumptions. Joshep, Steckler and Truhlar[35] developed the PES for $CH_4 + H \rightarrow CH_3 + H_2$, abstraction reaction by fitting the experimental data and *ab initio* data reported by Duchovic, Hase and Schlegel.[36] Jordon and Gilbert[37] modified the surface to incorporate nuclear permutation symmetry and reported classical trajectory studies for the above reaction. Klippenstein and Radivoyevitch[38] have used this method effectively to obtain an analytical potential for NO_2 dissociation. Hase *et al.*[39] have studied complex formation between Li^+ and H_2O using an analytical fit to the *ab initio* data obtained by Clementi and Popkie[40]. Hu and Hase[41] used a modified form of the Duchovic, Hase, Schlegel potential[36] to study both variational transition-state theory and trajectory calculations of the $H + CH_3 \rightarrow CH_4$ reaction. Truong and Truhlar[42] have also conducted variational transition-state calculations on $OH + CH_4 \rightarrow H_2O + CH_3$ using an Ekart potential fitted to *ab initio* calculations at MP2 level of theory with 6-31G** and 6-311G** bases sets.

Similarly, a PES for Si_2H_6 system has been developed using *the ab initio* calculations[43-48] and experimental data[49-51].

In the above studies, many of the topographical features of the PES are inaccurate. Although, the global surfaces often have more than one hundred of adjustable parameters, this is insufficient to fit all the *ab initio* and experimental data. Errors in the PES are sometime sufficiently serious, even in small systems that erroneous dynamical results are obtained. Therefore, whenever a PES for polyatomic system is developed, the computed dynamics are always open to numerous critical comments related to the reliability of the surface. Therefore, we intend to carry out detailed sensitivity studies to determine which topographical features of PES are critical to properties such as reaction pathways, product yields and ratios, energy partitioning, intramolecular vibrational energy relaxation (IVR) rates and reaction rates. That is, we need to know how important it is to accurately model all the fundamental vibrational frequencies for reactants, products and transition state. How critical are the long-range portions of the bonding potential and van der Waals interactions? Do we need to ensure that the geometry of transition state is accurately represented by the global potential energy surface. Are reaction-coordinate curvature and barrier heights in the polyatomic systems as critical as they are in the three or four body systems?

To answer the above questions, we choose to study the gas-phase decomposition reaction of vinyl bromide. This system is sufficiently large to represent a polyatomic system and at the same time not too large to be computationally intractable. Several reaction channels are energetically open and the vibrational modes are highly coupled to the reaction coordinate. There is a possibility of energy-transfer bottlenecks.

Furthermore, this system has been studied both experimentally and theoretically. So a sufficient quantity of *ab initio* and experimental data are available which permit a careful evaluation of the accuracy of the surface and the predicted dynamics. A brief summary of previous experimental and theoretical studies of the unimolecular decomposition of vinyl bromide is given below.

The thermal and photolytic unimolecular decomposition reactions of vinyl bromide and the reverse, bimolecular reaction of HBr with acetylene in gas phase have been studied both experimentally and theoretically. Using shock tube methods, Saito *et al.*[52] investigated the gas-phase decomposition of vinyl bromide over the temperature range 1300-2000 K. They reported that the decomposition proceeds solely via molecular elimination of HBr:

$$H_2C{=}CHBr \rightarrow HBr + HCCH \quad (r1)$$

The measured activation energy for reaction r1 is 1.80±0.069 eV. However, it is not known whether HBr elimination occurs via a three- or four-center elimination reaction. In case of three-center elimination, HBr is first eliminated from the same carbon atom then the vinylidene rapidly rearranges to acetylene, since the barrier for this rearrangement is less than 0.113 eV[53,54]. In case of four-center HBr elimination acetylene is formed directly.

$$H_2C{=}CHBr \rightarrow H_2C{=}C + HBr \quad (r2)$$

$$H_2C{=}C \rightarrow HC{\equiv}CH \quad (r3)$$

Wodtke *et al.*[55] have photolyzed a molecular beam of vinyl bromide at 193 nm. The product fragments were determined by mass analysis. From time-of-flight

measurements, they obtained the product translational energies. The results indicate that the predominate decomposition channel is Br atom dissociation.

$H_2C{=}CHBr \rightarrow Br + C_2H_3$ (r4)

The HBr elimination is a less important reaction channel in their studies. The measured Br/HBr product ratio is 1.28±0.05.

In contrast, the photolysis experiments reported by Johnston and Price[56], which employ xenon-filled lamps that emit in the 150–200 nm region, suggest that reaction r1 is the only important decomposition channel for vinyl bromide. The mass spectrum of the photolysis products indicates the presence of very low concentration vinyl radicals. Consequently, it was concluded that the reaction r4 played little role in the photolytic decomposition of vinyl bromide. No molecular H_2 or bromoacetylene was detected by either Jonston and Price[56] or Wodtke[55].

The photolytic dynamics of vinyl bromide are very different under matrix-isolated conditions. Experiments reported by Abrash *et al.*[57,58] showed that the only primary products are HBr and acetylene formed via reaction r1 in either a three- or four-center mechanism. No Br atom formation is observed. However, an important secondary channel leading to H_2 and bromoacetylene is seen

$H_2C{=}CHBr \rightarrow H_2 + HCCBr$ (r5)

The shape of the HBr-acetylene and bromoacetylene growth curves suggests that the reaction r1 is a primary, first-order process whereas r5 is a secondary reaction initiated by photolysis of the products of reaction r1. The experiments provide no information related to the molecular mechanisms involved in producing H_2 and bromoacetylene via

photolysis of a matrix-isolated HBr/acetylene pair. There is also no information about the participation of excited electronic states in these processes.

Abrash *et al.*[58] have studied the photochemistry of the hydrogen-bonded complex between HBr and acetylene in solid krypton using a medium pressure Hg lamp at 12K. For HBr-acetylene, the major product is bromoacetylene. Very little vinyl bromide is detected.

$$HBr + HCCH \rightarrow H_2 + HCCBr. \quad (r6)$$

In contrast, when a $HBr/C_2D_2/Kr$ mixture is photolyzed, the major reaction channel is

$$HBr + DCCD \rightarrow DBr + HCCD. \quad (r7)$$

The measured absorption intensities suggest that the channel forming HD and DCCBr via r6 is the second most important reaction channel among reactions leading to C_2 products. However, the relative importance of the various reaction channels is not certain since the extinction coefficients are unknown. Some decomposition of D_2 is observed via following mechanism:

$$HBr + DCCD \rightarrow D_2 + HCCBr \quad (r8)$$

The average r7/r8 intensity ratio is about 1.7±0.3. Finally, the only isomer found is cis-CDBrCHD via αβ-addition:

$$HBr + DCCD \rightarrow \text{cis-DBrCCHD} \quad (r9)$$

Except for r9, the mechanisms involved for the other reactions are not clearly known. If r6 takes place by αβ-addition to form an excited vinyl bromide which then eliminates H_2, it is difficult to understand why none of gas-phase photolysis studies[55,56] of vinyl bromide yield H_2 as a decomposition product. It is possible that r6 occurs via initial dissociation of HBr followed by the atomic abstraction of hydrogen and Br atom addition. Reaction r7

might occur via the sequence αβ-addition followed by three-center elimination of DBr and conversion of vinylidene to acetylene by hydrogen or deuterium atom migration. It might also involve an atomic mechanism. Reaction r8 apparently occurs via four-center D_2 elimination.

The results obtained upon photolysis of (DBR/HBr/C_2H_2/Kr) and (DBr/HBr/C_2D_2/Kr) mixtures raise additional mechanistic questions[57,58]. In the former case, the decomposition products are, in order of importance, HCCBr, HCCD, DCCBR, and cis-HDC=CHBr. No trans- product is observed. In the later case, the order of product importance is DCCBr, HCCD, cis-HDC=CDBr, trans-HDC=CDBr. No vinyl-1,1-d_2 bromide is seen. Relevant questions relate to why the trans isomer is seen in the later case but not in the former case and why there is no 1,1-d_2 isomer formed. It is possible that the answer of these questions may simply lie in the experimental signal-to-noise ratio[57,58].

One possible mechanism which could explain the anomalous matrix results would be dissociation of HBr followed by cage recombination to form excited HBr which then adds to acetylene. Thus, a study of the gas-phase reaction of vinyl bromide with acetylene can cast light on whether the above mechanism can account for the anomalous results obtained from the matrix photolysis of the HBr-acetylene complex.

Ebert *et al.*[59] investigated gas-phase collisions between HBr and acetylene, theoretically using classical trajectory methods. Their studies indicated that hydrogen exchange is the dominant reaction channel when both HBr and acetylene are in their vibrational ground states. Hydrogen-atom addition competes with hydrogen exchange as the translational energy of HBr is increased above 4.8 eV. Near the dissociation threshold of HBr, the collisional dissociation of HBr and bromine-atom addition are the

dominant reaction channels. Their studies also indicated large differences between the dependence of the reaction cross sections for the various reaction channels on HBr vibrational energy which suggest a very high degree of product selectivity in the HBr-acetylene collisions. They have suggested two distinct mechanisms for different reaction channels. One of these involves the initial formation of vibrationally excited vinyl bromide followed by unimolecular dissociation. The other mechanism avoids the formation of vinyl bromide. This mechanism suggests that HBr first dissociates then a hydrogen atom adds to acetylene. However, bromine-atom addition never takes place. As the bromine atom departs, it abstracts the hydrogen atom from the carbon adjacent to the one at which hydrogen-atom addition occurred. Although no experimental studies involving HBr and acetylene have been reported, there have been several studies involving vinyl chloride and acetylene[60] which provide very useful information.

Abrash *et al.*[61] reported classical trajectory studies of the gas-phase decomposition of vinyl bromide using a ground state, empirical potential-energy surface. The dissociation dynamics of vinyl bromide were investigated at several excitation energies in the range 4.0–6.44 eV. Their studies indicate that the decomposition dynamics follow a first-order rate law. At thermal energies, the only brominated decomposition product is HBr. The results indicate that previously reported activation energy is too small. At E=6.44 eV, the reaction channels are, in order of importance, H_2 elimination (48.1%), HBr elimination (44.5%), Br atom dissociation (4.6%) and C-H bond fission (2.6%). The fraction of the total excitation energy partitioned into product translational energy and HBr internal energy upon elimination of HBr is nearly independent of the total excitation energy. Comparison of the calculated and measured

relative translational energy distributions for Br atoms upon C-Br bond fission and time-of-flight spectra for C_2H_2 upon HBr elimination indicates that in previously reported photolysis experiments, Br atom dissociation is occurring from an excited state whereas HBr elimination is occurring on the ground-state potential-energy surface. Both H_2 and HBr elimination occur almost exclusively by a three-center mechanism. For both three- and four-center dissociation reactions, both C-X bonds rupture almost simultaneously. The computed branching ratios suggest that the dynamics on the ground-state potential energy surface are nonstatistical.

Mains *et al.*[62] studied the decomposition dynamics of vinyl bromide upon single-photon excitation at 193 nm using classical trajectory methods on an adiabatic excited-state PES that was obtained using empirical and *ab initio* configuration interaction (CI) methods. Their studies indicate that dissociation of vinyl bromide upon photolysis at 193 nm involves excitation to three or four repulsive C-Br states. Three hundred trajectories were computed to determine the effects of vertical excitation from ground state to the ($\pi\sigma^*$) and ($n\sigma^*$) excited-states. The results indicate that the only products for these excitations are vinyl radicals and either Br ($^2P_{3/2}$) or Br ($^2P_{1/2}$) atoms. No HBr is observed. These results are consistent with earlier studies[4,5]. Their calculated translational energy distributions for C_2H_3 and either Br ($^2P_{3/2}$) or Br ($^2P_{1/2}$) atoms are peaked at energies significantly in excess of those observed in the beam experiments. This indicates that the *ab initio* excited-states are too repulsive. Comparison with experimental data suggests that the *ab initio* energies near the C-Br equilibrium distance are too large by 16 kcal/mol. The computed full-width at half-maximum is much smaller than the experimental results suggesting that decomposition is occurring from more than one

excited-state. They have also shown that a good fit to the measured translational energy distribution can be obtained from a linear combination of the distributions calculated from three empirical potentials whose energy at C-Br equilibrium distance is reduced by 16 kcal/mol from that predicted by *ab initio* calculations.

Kay and Raff[63] investigated statistical and nonstatistical dynamics in the unimolecular decomposition of vinyl bromide in the gas phase. They computed the rate constants for three unimolecular decomposition reactions of vinyl bromide for several energies in the range 5.23 – 7.67 eV using statistical variational efficient micro-canonical sampling-transition-state theory (EMS-TST) on a global potential-energy surface. In order to assess the extent to which the unimolecular decomposition is governed by statistical dynamics, they compared the EMS-TST results with those obtained from the classical trajectory studies on the same potential-energy surface. For the three-center HBr elimination reaction, it is found that $k_{EMS\text{-}TST}$ (rate constant from EMS-TST calculations) is greater than $k_{trajectory}$ (rate constant from classical trajectory calculations) by a factor of 1.5 – 3.5 over the above energy range. For C-Br bond fission, at lower energies, EMS-TST and trajectory results are equal to within the statistical error in the trajectory calculations, while at higher energies $k_{EMS\text{-}TST}$ exceeds $k_{trajectory}$ by a factor of 1.4 – 2.9. The rate constants from EMS-TST calculations for three-center HBr elimination are an order of magnitude greater than those for C-Br bond fission throughout the above energy range. A similar trend has been observed in the trajectory calculations. The results indicate that three-center HBr elimination and C-Br bond fission are governed by statistical dynamics. On the other hand, for three-center H_2 elimination $k_{trajectory}$ is greater than $k_{EMS\text{-}TST}$ by a factor of 2-4 at lower energies and 5-7 at higher energies. This

necessarily indicates that the dynamics of three-center H_2 elimination are nonstatistical. The nonstatistical behavior for this reaction is attributed to a breakdown in the coupling among vibrational modes as H_2 fragment departs, which leaves energy in excess of the statistically predicted amount in the dissociation coordinate.

Pan and Raff[64,65] have investigated intramolecular energy transfer rates and pathways for vinyl bromide and deuterium substituted vinyl bromides using projection methods and continuous frequency modulated (CFM) line splitting. The projection method is based on the calculation of the temporal variation of a diagonal kinetic energy matrix. Energy transfer rates and pathways are extracted from the envelop functions of these temporal variations. Using the virial theorem, the average mode energies are calculated. Total energy decay rates and pathways for energy flow for initial excitation of each of the 12 vibrational modes in the equilibrium configuration and in initial configurations corresponding to points in the near vicinity of the minimum-energy structure on the optimum dividing surfaces for three-center HBr and H_2 elimination are reported. For the equilibrium configuration, the total energy relaxation rate for each mode is first order. The minimum decay rate among the 12 modes is 3.1 times greater than the decomposition of vinyl bromide with 6.44 eV excitation energy. Their studies indicate that the energy transfer is not globally rapid. In configurations near the minimum-energy structure on the optimum-dividing surface for three-center H_2 elimination, the intramolecular energy transfer rate for some mode-to-mode processes is slower than the unimolecular dissociation rate. Whereas, energy transfer in configurations near the minimum-energy structure on the optimum-dividing surface for three-center HBr elimination is globally rapid relative to the HBr elimination rate for all modes except the

C-C-Br bend. Based on the results, they have suggested that three-center HBr elimination can be described by statistical theories but three-center H_2 elimination will behave non-statistically.

In CFM line splitting, energy-transfer rate coefficients are extracted from the fine structure spacing of the numerically computed power spectrum of the bond coordinate. These individual rate coefficients are averaged over an ensemble of 5-10 trajectories and compared with results obtained from local-mode energy decay curves. The total IVR rate coefficients are large relative to the unimolecular dissociation which is in contrast to the previous study using projection methods[4].

The primary objective of this study is to determine the topographical features of the PES that are most important in determining the reaction and energy transfer dynamics in polyatomic systems. Our approach is to incorporate successive modifications to the presently available PES[61] for vinyl bromide and then assess the effect of the modifications on the dynamics. This requires sufficient *ab initio* electronic structure calculations to obtain a database to which the global potential will be fitted. It is never possible to correct one feature of the complex PES without simultaneous alteration of the other features. So the fitting must be done in an iterative way. The accuracy of the surface will be tested against the entire *ab initio* and experimental database. Once the new PES is developed, then certain topographical features of the PES will be altered one at a time and classical trajectory calculations will be performed on the PES to determine the extent to which they influence the reaction and energy transfer-dynamics. This thesis is divided into five parts. Following this introduction, a brief description of the PES is provided and the basis of the computational method is reviewed. In Section III, the effects of

multidimensional PES topology on the unimolecular dissociation rate of vinyl bromide are presented. In Section IV, after a brief introduction, we present the projection operator methods for IVR studies followed by results and discussion.

Reference:

1. N. Bakkas, Y. Bouteiller, Aloutellier, J. P. Perchard and S. Racine, *J. Chem. Phys.* **99**, 3335 (1993).

2. B. D. Waldlowski, A. L. L. East, J. E. Mihalick W. D. Allen and J. I. Brauman, *J. Chem. Phys.* **100**, 2058 (1994).

3. S. P. Walch, *J. Chem. Phys.* **98**, 3163 (1993).

4. S. P. Walch, *J. Chem. Phys.* **99**, 5295 (1993).

5. S. H. Robertson, D. M. Wardlaw and D. M. Hirst, *J. Chem. Phys.* **99**, 7748 (1993).

6. A. M. Mebel, K. Morokuma and M. C. Lin, *J. Chem. Phys.* **101**, 3916 (1994).

7. S. A. Maluendes, A. D. McLean, K. Yamashita and E. Herbst *J. Chem. Phys.* **99**, 2812 (1993).

8. T. H. Dunning, *J. Chem. Phys.* **55**, 716 (1971).

9. S. Huzinaga, *J. Chem. Phys.* **42**, 1293 (1965).

10. J. H. Jensen, K. Morokuma and M. S. Gordon, *J. Chem. Phys.* **100**, 1981 (1994).

11. H. Okabe and J. R. McNesby, *J. Chem. Phys.* **36**, 601 (1962).

12. B. A. Balko, J. Zhang and Y. T. Lee, *J. Chem. Phys.* **97**, 935 (1992).

13. J. F. Riehl and K. Morokuma *J. Chem. Phys.* **100**, 8976 (1994).

14. P. Ausloos, R. E. Rebbert and M. H. Wijnen, *J. Res, Nat. Bur. Std.* **77a**, 243 (1973).

15. C. Reiser, F. M. Lussier, C. C. Jensen and J. I. Steinfeld, *J. Am. Chem. Soc.* **101**, 350 (1979).

16. Y. Huang, Y. Yang, G. He and R. J. Gordon, *J. Chem. Phys.* **99**, 2752 (1993).

17. T. D. Swell and D. L. Thompson, *J. Chem. Phys.* **93**, 4077 (1990).

18. A. J. Marks, *J. Chem. Phys.* **100**, 8096(1994).

19. B. M. Rice and D. L. Thompson, *J. Chem. Phys.* **93**, 7986 (1990).

20. R. Alimi, V. A. Apkarian R. B. Gerber, *J. Chem. Phys.* **98,** 331 (1993).

21. G. Lendvay and G. C. Schatz, *J. Chem. Phys.* **96**, 4356 (1992).

22. G. Lendvay and G. C. Schatz, *J. Chem. Phys.* **98**, 1034 (1993).

23. F. E. Budenholzer, M. Y. Chang and K. C. Huang, *J. Phys. Chem.* **98**, 12501 (1994).

28. L. M. Raff, *J. Phys. Chem.* **91**, 3266 (1987).

29. L. M. Raff, *J. Phys. Chem.* **92**, 141 (1988).

30. L. M. Raff and R. W. Graham. *J. Phys. Chem.* **92**, 5111 (1988).

31. Y. J. Cho, S. R. Vande Linde, L. Zhu and W. L. Hase, *J. Chem. Phys.* **96**, 7962 (1990)

32. S. R. Vande Linde and W. L. Hase, *J. Chem. Phys.* **93**, 7962 (1990).

33. S. R. Vande Linde and W. L. Hase, *J. Phys. Chem.* **94**, 6148 (1990).

34. W. L. Hase and Y. J. Cho, *J. Chem. Phys.* **98**, 8626 (1993).

35. T. R. Joshep, R. Steckler and D. G. Truhlar, *J. Chem. Phys.* **87**, 7036 (1987).

36. R. Duchovic, W. L. Hase and H. B. Schlege, *J. Phys. Chem.* **88**, 1339 (1984).

37. M. J. T. Jordan and R. G. Gilbert, *J. Chem. Phys.* **102**, 5669 (1995)

38. S. J. Klippenstein and T. Radivoyevitch, *J. Chem. Phys.* **99**, 3644 (1993).

39. W. L. Hase, C. L. Darling and L. Zhu, *J. Chem. Phys.* **96**, 8295 (1992).

40. D. Clementi and H. Popkie, *J. Chem. Phys.* **57**, 1077 (1972).

41. X. Hu and W. L. Hase, *J. Chem. Phys.* **95**, 8073 (1991); *ibid,* **96**, 5558 (1992).

42. T. N. Truong and D. G. Truhlar, *J. Chem. Phys.* **93**, 1761 (1990); *ibid,* **97**, 8820 (1992).

43. P. Ho, M. E. Coltrin, J. S. Binkley and C. F. Melius, *J. Phys. Chem.* **89**, 4647 (1986).

44. P. Ho, M. E. Coltrin, J. S. Binkley and C. F. Melius, *J. Phys. Chem.* **90**, 3399 (1986).

45. M. S. Gordon, T. N. Truong and E. K. Bonderson, *J. Am. Chem. Soc.* **108**, 2191 (1986).

46. M. S. Gordon, D. R. Gano, J. S. Binkley and M. J. Frisch, *J. Am. Chem. Soc.* **108,** 2191 (1986).

47. J. S. Binkley, *J. Am. Chem. Soc.* **106**, 603 (1982)

48. P. M. Agrawal, D. L. Thompson and L. M. Raff, *J. Chem. Phys.* **92**, 1069 (1990).

49. J. Berkowitz, J. P. Greene, H. Cho and B. Ruscic, *J. Chem. Phys.* **86**, 1235 (1987).

50. J. M. Jasinski, *J. Phys. Chem.* **90**, 555 (1986).

51. G. Inoue and M. Suzuki, *Chem. Phys. Lett.* **122**, 361 (1985).

52. K. Saito, T. Yokubo, T. Fuse, H. Tahara, O. Kondo, T. Higashihara and I. Murakami, *Bull. Chem. Soc. Jpn.* **52**,3507 (1979).

53. R. Krishnan, M. J. Frisch, J. A. Pople and P. v. R. Schleyer, *Chem. Phys. Lett.* **79**, 408 (1981).

54. (a) Y. Osamura, H. F., III. Schaefer, S. K. Gray, W. H. Miller, *J. Am.Chem. Soc.* **103**, 1904, (1981).

(b) B. J. Smith, R. Smernik, L. Radom. *Chem. Phys. Lett.* **188**, 589 (1992).

(c) Ph. Halvick, D. Liotard, J. C. Rayez, *Chem. Phys.* **177**, 69 (1993).

55. (a) A. M. Wodtke, E. J. Hintsa, J. Somorjai, Y. T. Lee, *Isr. J. Chem.* **29**, 383 (1989).

(b) A. M. Wodtke, Y. T. Lee, *J. Phys. Chem.* **89**, 4744 (1985).

56. G. R. Johnston and D. Price, *Dyn. Mass Spectrom.* **3**, 183 (1973).

57. S. A. Abrash Ph. D. Dissertation, Univ. of California at Berkeley (1987).

58. S. A. Abrash, M. T. McMahon, R. W. Zehner, *J. Phys. Chem.* **98**, 11909 (1994).

59. M. E. Ebert, S. A. Abrash, L. M. Raff, *J. Phys. Chem.* **99**, 17691 (1995).

60. (a) B. A. Balko, J. Zhang, Y. T. Lee, *J. Chem. Phys.* **97**, 935, (1992).

(b) P. Ausloos, R. E. Robberts, M. H. Wijnen, *J. Res. Natl. Bur. Stand.* **77A**, 243 (1973).

(c) C. Reiser, F. M. Lussier, C. C. Jensen, I. J. Steinfeld, *J. Am. Chem. Soc.* **101**, 350 (1979).

61. S. A. Abrash, R. W. Zehner, G. J. Mains, L. M. Raff, *J. Phys. Chem.* **99**, 2959 (1995).

62. G. J. Mains, L. M. Raff, S. A. Abrash, *J. Phys. Chem.* **99**, 3532 (1995).

63. R. D. Kay and L. M. Raff, *J. Phys. Chem.* **101**, 1007, (1997).

64. R. Pan and L. M. Raff, *J. Phys. Chem.* **100**, 8085 (1996).

65. R. Pan and L. M. Raff, *J. Phys. Chem.* **106**, 1382 (1997).

CHAPTER II

DESCRIPTION OF POTENTIAL-ENERGY SURFACES

A. *Ab Initio* Calculations

To obtain an accurate global potential-energy surface, it is important to know exactly how the potential varies due to stretching of bonds, bending of angles and torsion of dihedral angles. This requires high-level of *ab initio* calculations for a large number of configurations. We have carried out a series of *ab initio* calculations at the MP4(SDT) level of theory using the GAUSSIAN 94[1] package. For C and H atoms, we have used 6-31G(d,p) basis sets. Huzinaga's (4333/433/4) basis sets[2] augmented with split outer s and p orbitals (43321/4321/4) are used for the Br atom to improve the flexibility of the Br electron density. A polarization f orbital is added with an exponent of 0.5 for more accurate description of the Br atom. We have performed a relaxed potential energy scan for all bonds, angles and dihedral angles. That is, each bond is stretched or compressed in increments of 0.1 Å from its equilibrium value for a reasonable length. At each increment, the molecule (C_2H_3Br) is relaxed by optimizing the geometry keeping the bond which is being stretched or compressed to a fixed value and the energy of the molecule at that particular geometry is calculated. In this way, we scan the potential for all bonds one at time. Once the *ab initio* data points are obtained, then we fit those data points with appropriate functions using least-square methods. For bond stretching, usually a modified

Morse potential function is used (see the analytical PES for the functional form). We use these fitted analytical functions to describe the ground state PES for vinyl bromide.

Similarly, each angle is varied from its equilibrium value in increments of 5^{o} and at each increment, the geometry of the molecule is optimized keeping the angle to a fixed value. The energy at that optimized point is calculated to obtain the bending potential. The data points are then fitted to an analytic function using least-square methods. We scan the PES to obtain the potential functions for all the angles and use those functions to develop the ground state PES for vinyl bromide.

Dihedral angles are coupled to each other. The change in one of the dihedral angles causes other dihedral angles to change. It is very difficult to determine how much contribution only one dihedral angle makes to the total potential. To overcome this difficulty, we assume that all the dihedral angles make same contributions to the total potential energy. We perform the relaxed potential energy scan for the dihedral angles in the same way as for bonds and angles. With the above assumption, *ab initio* data points are divided by four (as four dihedral angles are involved) and fitted to a seven-terms cosine series to obtain torsional potential functions.

B. Analytic Potential-Energy Surface

In order to study the sensitivities of different topographical features of PES on the dynamics, we have modified the presently available surface[3] for vinyl bromide. The new surface has been developed using the 'combined method' which has been employed to obtain the global potential energy-surfaces for SiH_2,[4] SiH_4,[5] Si_2H_4,[4] Si_2H_6,[6] C_2H_4,[7-13]

H_2FCCH_2F,[7-13] $H_2C{=}CHF$,[7-13] H_3CCHCl[14] systems. At first, accurate global potentials for each of the open reaction channels are developed using functional form suggested by physical and chemical considerations. The parameters of these functions are expressed as appropriate functions of the system's geometry. These channel potentials are connected smoothly with parameterized switching functions. The calculated barriers or activation energies can be accurately fitted by the adjustment of the switching function parameters. The reaction channels of primary interest in the vinyl bromide reaction dynamics are given in Table 2.1.

TABLE 2.1

Reaction channels represented by the empirical C_2H_3Br global potential-energy surface developed by Abrash *et al.*[a]

Channel	Reaction
I	$C_2H_3Br \rightarrow C_2H_3 + Br$
IIA	$C_2H_3Br \rightarrow H^5Br + C_2H_2$
IIB	$C_2H_3Br \rightarrow H^5 + Br + C_2H_2$
IIIA	$C_2H_3Br \rightarrow H^4Br + C_2H_2$
IIIB	$C_2H_3Br \rightarrow H^4 + Br + C_2H_2$
IVA	$C_2H_3Br \rightarrow H^3H^4 + HC{\equiv}CBr$
IVB	$C_2H_3Br \rightarrow H^3 + H^4 + HC{\equiv}CBr$
VA	$C_2H_3Br \rightarrow H^3H^5 + HC{\equiv}CBr$
VB	$C_2H_3Br \rightarrow H^3 + H^5 + HC{\equiv}CBr$
VI	$C_2H_3Br \rightarrow H^3Br + H_2C{=}C$
	$H_2C{=}C \rightarrow HC{\equiv}CH$
VII	$C_2H_3Br \rightarrow H^4H^5 + C{=}CHBr$

[a] Superscripts denote the atom number given in Fig. 2.1

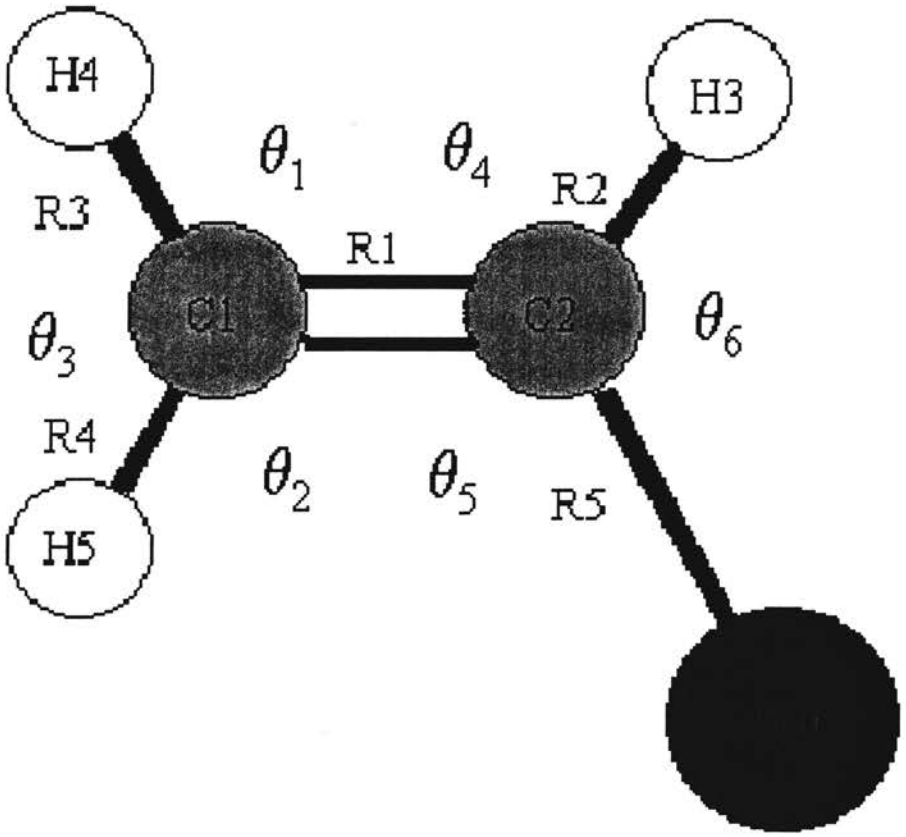

Figure 2.1

Definition of atom numbers used in the analytic potential-energy surface (PES)

The labeling of atoms and angles used in the description of analytical fit for the ground state PES of vinyl bromide is shown in Figure 2.1. The definitions of the 15 interatomic distances are given in Table 2.2.

Table 2.2

Definitions of internulear distances

Internuclear Distance	Atom i	Atom j
R_1	1	2
R_2	2	3
R_3	1	4
R_4	1	3
R_5	2	4
R_6	3	4
R_7	1	5
R_8	2	5
R_9	4	5
R_{10}	5	3
R_{11}	1	6
R_{12}	2	6
R_{13}	3	6
R_{14}	4	6
R_{15}	5	6

Previous studies by Abrash *et. al.*[3] indicate that at higher energy, the dissociation of vinyl bromide occurs primarily via three-center HBr elimination followed by three-center H_2 elimination and then Br atom dissociation and H atom dissociation. To keep the model potential simple, we have considered only the important reaction channels,

namely: three-center HBr elimination (V_{VI}), three-center H_2 elimination (V_{VII}), Br atom dissociation and H atom dissociation. The overall potential-energy surface (V_T) for C_2H_3Br is then written in terms of channel potentials as:

$$V_T = ([[\{(V_I S_3)S_4\}S_5 + V_{VI}S_6]S_7]S_8)S_9 + V_{VII}S_{10} \quad (2.1)$$

where the S_i (i = 3,4,.....10) are the switching functions that smoothly connect the various channel potentials. The notation for these channel potentials are chosen so as to be consistent with that employed by Abrash *et al.*[3] for the original empirical vinyl bromide potential and V_I, V_{VI} and V_{VII} are the channel potential for the atom dissociation, three-center HBr elimination and three-center H_2 dissociation, respectively. The switching functions are given as follows:

$$S_3 = 1 - A_7A_{12}\,(1 - A_3)(1 - A_2) \quad (2.2)$$

$$S_4 = 1 - A_3A_{12}(1 - A_2)(1 - A_7) \quad (2.3)$$

$$S_5 = 1 - E_2E_{12} \quad (2.4)$$

$$S_6 = F_2F_{12} \quad (2.5)$$

$$S_7 = 1 - C_2C_7(1 - C_{12})(1 - C_3) \quad (2.6)$$

$$S_8 = 1 - C_2C_3(1 - C_{12})(1 - C_7) \quad (2.7)$$

$$S_9 = 1 - G_3G_7 \quad (2.8)$$

$$S_{10} = H_3H_7 \quad (2.9)$$

In the above definitions of switching functions, subscripts on A, C, E, F, G and H indicate the interatomic distances used. These functions are defined below:

$$A_7 = \tanh[\exp\{a_7(R_7 - R_{35}^{o})^2\} - 1] \quad (2.10)$$

$$A_{12} = \tanh[\exp\{a_8(R_{12} - R_2^{o})^2\} - 1] \quad (2.11)$$

$$A_3 = \tanh[\exp\{a_7(R_3 - R_{34}^{o})^2\} - 1] \quad (2.12)$$

$$A_2 = \tanh[\exp\{a_7(R_2 - R_{33}^{o})^2\} - 1] \quad (2.13)$$

$$C_7 = \tanh[a_9(R_7 - R_{35}^{o})^2] \quad (2.14)$$

$$C_{12} = \tanh[a_{10}(R_{12} - R_2^{o})^2] \quad (2.15)$$

$$C_3 = \tanh[a_9(R_3 - R_{34}^{o})^2] \quad (2.16)$$

$$C_2 = \tanh[a_9(R_2 - R_{33}^{o})^2] \quad (2.17)$$

$$E_2 = \tanh[a_{11}(R_2 - R_{33}^{o})^2] \quad (2.18)$$

$$E_{12} = \tanh[a_{12}(R_{12} - R_2^{o})^2] \quad (2.19)$$

$$F_2 = \tanh[a_{13}(R_2 - R_{33}^{o})^2] \quad (2.20)$$

$$F_{12} = \tanh[a_{14}(R_{12} - R_2^{o})^2] \quad (2.21)$$

$$G_3 = \tanh[a_{15}(R_3 - R_{34}^{o})^2] \quad (2.22)$$

$$G_7 = \tanh[a_{16}(R_7 - R_{35}^{o})^2] \quad (2.23)$$

$$H_3 = \tanh[a_{17}(R_3 - R_{34}^{o})^2] \quad (2.24)$$

$$H_7 = \tanh[a_{18}(R_7 - R_{35}^{o})^2] \quad (2.25)$$

In the above Equations 2.10–2.25, the R_k^{o} are the ground-state equilibrium bond lengths and the a_i are the parameters used to fit the potential barrier for various reaction channels. The values of these parameters are given in Table 2.3.

It is clear from Equation 2.1 that when $S_3 = S_4 = S_5 = S_7 = S_8 = S_9 = 1$ and $S_6 = S_{10} = 0$, the system is in the reactant or product configuration space for the atomic dissociation. In the same way, by choosing appropriate switching functions to have values equal to 1 or 0, we can represent the system in the product configuration space for either channel VI or channel VII.

Table 2.3

Switching function parameters

Parameter	Value			Parameter	Value		
	PES1	PES2	PES3		PES1	PES2	PES3
a_1	0.400 $Å^{-2}$	3.800 $Å^{-2}$	3.800 $Å^{-2}$	a_{17}	8.578 $Å^{-2}$	8.918 $Å^{-2}$	9.300 $Å^{-2}$
a_7	5.000 $Å^{-2}$	5.000 $Å^{-2}$	5.000 $Å^{-2}$	a_{18}	8.058 $Å^{-2}$	7.878 $Å^{-2}$	8.478 $Å^{-2}$
a_8	5.000 $Å^{-2}$	5.000 $Å^{-2}$	5.000 $Å^{-2}$	R_2^o	1.9229 Å	1.9229 Å	1.9229Å
a_9	7.825 $Å^{-2}$	7.825 $Å^{-2}$	7.825 $Å^{-2}$	R_{33}^o	1.0785 Å	1.0785 Å	1.0785Å
a_{10}	7.500 $Å^{-2}$	7.500 $Å^{-2}$	7.500 $Å^{-2}$	R_{34}^o	1.0811 Å	1.0811 Å	1.0811Å
a_{11}	6.700 $Å^{-2}$	3.900 $Å^{-2}$	3.900 $Å^{-2}$	R_{35}^o	1.0803 Å	1.0803 Å	1.0803Å
a_{12}	6.700 $Å^{-2}$	3.900 $Å^{-2}$	3.900 $Å^{-2}$				
a_{13}	7.500 $Å^{-2}$	5.500 $Å^{-2}$	5.900 $Å^{-2}$				
a_{14}	7.000 $Å^{-2}$	4.050 $Å^{-2}$	4.050 $Å^{-2}$				
a_{15}	7.820 $Å^{-2}$	7.820 $Å^{-2}$	7.200 $Å^{-2}$				
a_{16}	7.820 $Å^{-2}$	7.820 $Å^{-2}$	7.200 $Å^{-2}$				

The channel I potential, V_I, represents the system when its configuration corresponds to either reactant, products or transition state for vinyl bromide undergoing Br atom or H atom dissociation. It is written as a sum of stretching potentials for bonds, bending potentials for angles and torsion potentials for dihedral angles;

$$V_I = V_{CC} + V_{CBr} + V_{CH^3} + V_{CH^4} + V_{CH^5} + \sum_{i=1}^{6} V_{\alpha\beta\gamma}(\theta_i) + \sum_{i=1}^{4} V_{ABCD}(\phi_i), \qquad (2.26)$$

where superscripts denote the atom numbers defined in Figure 2.1.

In Eq. 2.26, V_{CC} represents the interaction potential for C=C bond stretching. For $R1 \leq 1.6$,

$$V_{CC} = D_{CC}[\exp\{-2\alpha_{CC}(R_1 - R_{CC}^o)\} -$$

$$2\exp\{-\alpha_{CC}(R_1 - R_{CC}^{o})\}] + \beta^1(R_1 - R_{CC}^{o}) \quad (2.27)$$

A linear term is added to the Morse potential to fit the *ab initio* data.

For R1 > 1.6,

$$V_{CC} = [\lambda^1 - \mu^1(R_1 - R_{CC}^{o})]\exp\{-(R_1 - R_{CC}^{o})^2\} \quad (2.28)$$

with

$$D_{CC} = D_4 + (D_1 - D_4)S_1(R_{12}) \quad (2.29)$$

$$\alpha_{CC} = \alpha_4 + (\alpha_1 - \alpha_4)S_1(R_{12}) \quad (2.30)$$

and

$$R_{CC}^{o} = R_4^{o} + (R_1^{o} - R_4^{o})S_1(R_{12}) \quad (2.31)$$

The β^1, λ^1 and μ^1 are parameters adjusted to fit the *ab inito* data. It is important that the potential reaches to zero limits when two atoms forming a bond are separated far from each other. To ensure this fact, we use the exponential functional for V_{CC} in Eq. 2.28. To ensure continuity of the surface, we adjust the parameters of Eq. 2.28 such that the first derivatives and magnitude of potential are same for Eqs. 2.27 and 2.28. The switching function $S_1(R_{12})$ varies the C=C bond energy, equilibrium bond length and curvature as the bromine atom dissociates. The parameters of Equations 2.29-2.31 are chosen to fit thermochemical, structural and spectroscopic data for vinyl bromide and vinyl radical. The switching function $S_1(R_{12})$ has the following functional form:

$$S_1(R_{12}) = 1.0 - \tanh[a_1(R_{12} - a_2)^2] \quad (2.32)$$

The variation of potential energy with C=C bond stretching is shown in the figure below. Our fit to the *ab initio* data is excellent for $r_{cc} \leq 1.6$ Å. Although it seems that for $r_{cc} > 1.6$ Å our fit is not good, actually our fitted function will represent the potential more realistically than the *ab initio* data points. Because *ab initio* theories overestimate the

potential when the bonds are stretched far from its equilibrium by imposing the ionic behavior.

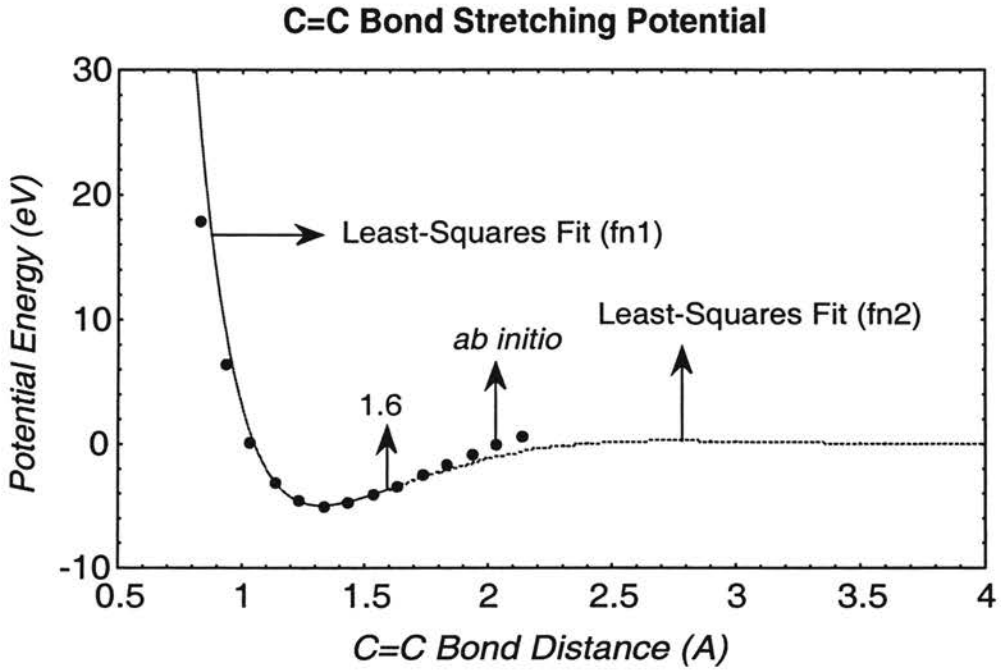

Figure 2.2 Shows variation of potential energy with C=C bond distance. Filled circles are *ab initio* data points and lines are the least-square fit to those points. Fn1 and fn2 denote two functions used for the fit at $r_{cc} \leq 1.6$ Å and $r_{cc} > 1.6$ Å respectively.

The following Table 2.4, shows the *ab initio* potential energy in at different C=C bond distances. In the column 'shifted potential', we have tabulated the potential energy in eV after shifting the equilibrium potential-energy to zero and subtracting the bond dissociation energy from *ab initio* value. The equilibrium potential-energy is the energy when the molecule is totally relaxed.

Table 2.4

C=C bond stretching potential energy.

C=C bond distance(Å)	*ab initio* potential (hartree)	Shifted potential (eV)
0.73120	-2646.34190	37.2890560139957
0.83120	-2647.05651	17.8398014879957
0.93120	-2647.47302	6.50381542199722
1.03120	-2647.70558	0.174322926005349
1.13120	-2647.82666	-3.12106300200429
1.23120	-2647.88049	-4.58613258000440
1.33120	-2647.89419(eqm)	-4.95900000000000(eqm)
1.43120	-2647.88460	-4.69799280600017
1.53120	-2647.86222	-4.08888529799622
1.63120	-2647.83353	-3.30804104399902
1.73120	-2647.80252	-2.46405427800817
1.83120	-2647.77153	-1.62061184399971
1.93120	-2647.74182	-0.81200665799877
2.03120	-2647.71383	-0.05.021402401069
2.13120	-2647.68772	0.660411402003607

The C-Br potential $V_{C\text{-}Br}$ has the following form:

For $R_{12} \leq 3.0$

$$V_{CBr} = D_2[\exp\{-2\alpha_2(R_{12} - R_2^o)\} - 2\exp\{-\alpha_2(R_{12} - R_2^o)\}] + \beta^2(R_{12} - R_2^o) \quad (2.33)$$

For $R_{12} > 3.0$

$$V_{CBr} = [\lambda^2 - \mu^2(R_{12} - R_2^o)]\exp\{-(R_{12} - R_2^o)^2\} \quad (2.34)$$

Figure 2.3 shows the variation of potential energy (V_{CBr}) with C-Br bond stretching. The filled circles are computed using *ab initio* theories and lines are the least-square fit to those data points. The Fn1 and Fn2 have functional form similar to Eq. 2.33 and 2.34. Likewise C=C potential, the fitting for the V_{CBr} is excellent.

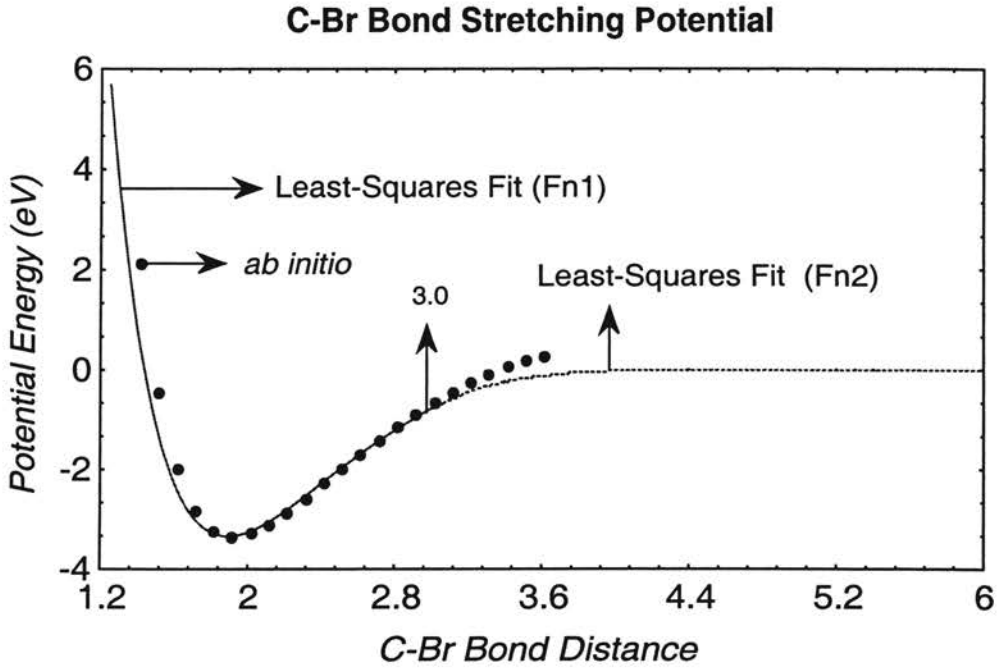

Figure 2.3 The variation of V_{CBr} with C-Br bond distance. Filled circles are *ab initio* data points and lines are the least-squares fit to those data points. The solid line indicates the function represented by Eq 2.33 and the dotted line indicates the function represented by Eq. 2.34.

Table 2.5 shows the *ab initio* potential energy in hartree at different C-Br bond distances (at each point the whole molecule is totally relaxed). In the column 'shifted potential', we have performed the same conversion of data points as in Table 2.4.

Table 2.5

Shows *ab initio* potential energy at different C-Br bond distances and potential energy used for construction of present potential-energy surfaces.

C-Br bond distance	*ab intio* potential energy(hartree)	Shifted potential energy(eV)
1.41490	-2647.69300	2.13589125598804
1.51490	-2647.78776	-0.443153760010377
1.61490	-2647.84382	-1.96891635601793
1.71490	-2647.87490	-2.81480828399805
1.81490	-2647.88977	-3.21951912601804
1.91490	-2647.89416	-3.33900000000000
2.01490	-2647.89186	-3.27640182001784
2.11490	-2647.88536	-3.09949392001005
2.21490	-2647.87636	-2.85454452002165
2.31490	-2647.86601	-2.57285271002189
2.41490	-2647.85508	-2.27537527200917
2.51490	-2647.84406	-1.97544834001025
2.61490	-2647.83327	-1.68178122601972
2.71490	-2647.82292	-1.40008941600542
2.81490	-2647.81312	-1.13336673600867
2.91490	-2647.80391	-0.882701850008802
3.01490	-2647.79536	-0.649999920009635
3.11490	-2647.78748	-0.435533112009638
3.21490	-2647.78033	-0.240934422014165
3.31490	-2647.77399	-0.068381178010954
3.41490	-2647.76857	0.079132793987752
3.51490	-2647.76424	0.196980671993457
3.61490	-2647.76120	0.279719135993160

The three C–H interaction terms have the following form.

When $R \leq 2.0$

$$V_{CH}^{k} = D_{CH}[\exp\{-2\alpha_{CH}^{k}(R - R_k^{o})\} - 2\exp\{-\alpha_{CH}^{k}(R - R_k^{o})\}] + \beta^{k}(R_{12} - R_2^{o}) \qquad \{\text{for } k=3, 4, 5\} \tag{2.35}$$

When $R > 2.0$

$$V_{CH}^{k} = [\lambda^{k} - \mu^{k}(R - R_k^{o})]\exp\{-(R - R_k^{o})^2\} \tag{2.36}$$

where R denotes the appropriate C–H bond distances, β^k, λ^k and μ^k are fitting parameters given in the Table 2.6 and

$$D_{CH} = D_5 + (D_3 - D_5)S_1(R_{12}) \quad (2.37)$$

$$\alpha_{CH}{}^k = \alpha_{5k} + (\alpha_{3k} - \alpha_{5k})S_1(R_{12}) \quad (2.38)$$

and

$$R_k{}^o = R_4{}^o + (R_1{}^o - R_4{}^o)S_1(R_{12}) \quad (2.39)$$

Table 2.6

Fitting parameters for bond stretching potential

Parameter	Value		Parameter	Value	
	PES1	PES2/PES3		PES1	PES2/PES3
β^1	0.52108	0.52108 eV/ Å^{-1}	λ^4	3.71996	3.50072 eV
β^2	0.42846	0.42846 eV/ Å^{-1}	λ^5	4.63733	4.41136 eV
β^3	0.31771	0.31771 eV/ Å^{-1}	μ^1	5.12142	4.07508 eV/ Å^{-1}
β^4	0.12409	0.12409 eV/ Å^{-1}	μ^2	1.11067	2.07047 eV/ Å^{-1}
β^5	0.37247	0.37247 eV/ Å^{-1}	μ^3	1.95433	0.96350 eV/ Å^{-1}
λ^1	5.28036	5.22718 eV	μ^4	0.74808	0.23177 eV/ Å^{-1}
λ^2	3.69015	4.22412 eV	μ^5	2.29598	1.30761 eV/ Å^{-1}
λ^3	4.44046	4.21223 eV			

The variation of potential energy ($V_{CH}{}^3$, $V_{CH}{}^4$, $V_{CH}{}^5$) with three C-H bonds respectively are shown in Figures 2.4a-2.4c. Inspection of Figures 2.4a-2.4c indicates that the fittings are excellent as they are in the case of V_{CC} and V_{CBr} potentials.

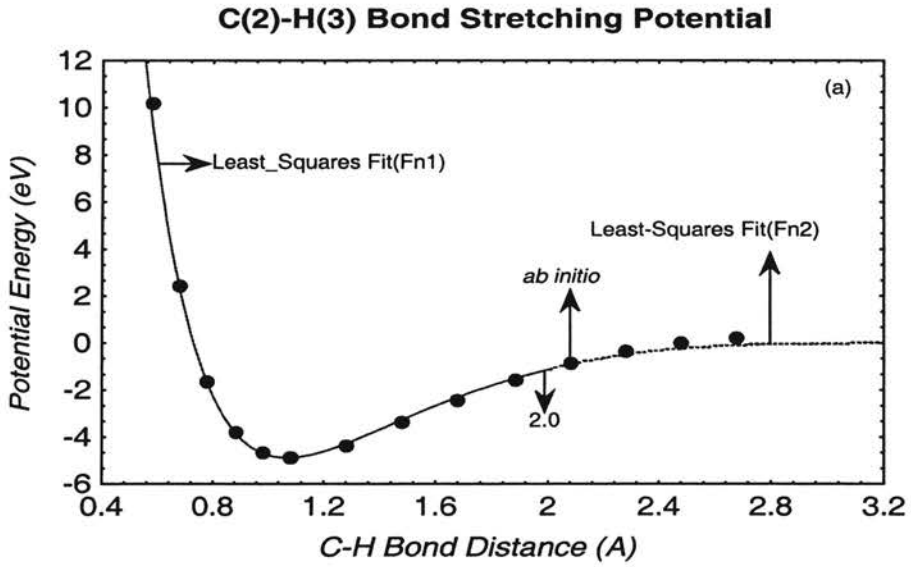
C(2)-H(3) Bond Stretching Potential
(a)
Least_Squares Fit(Fn1)
Least-Squares Fit(Fn2)
ab initio
2.0
Potential Energy (eV)
C-H Bond Distance (A)
12
10
8
6
4
2
0
-2
-4
-6
0.4
0.8
1.2
1.6
2
2.4
2.8
3.2

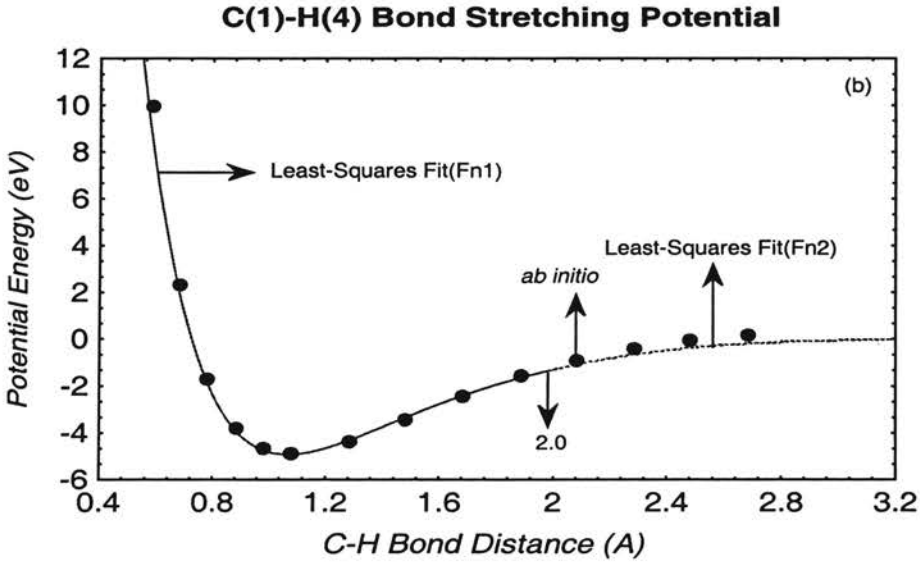
C(1)-H(4) Bond Stretching Potential
(b)
Least-Squares Fit(Fn1)
Least-Squares Fit(Fn2)
ab initio
2.0
Potential Energy (eV)
C-H Bond Distance (A)
12
10
8
6
4
2
0
-2
-4
-6
0.4
0.8
1.2
1.6
2
2.4
2.8
3.2

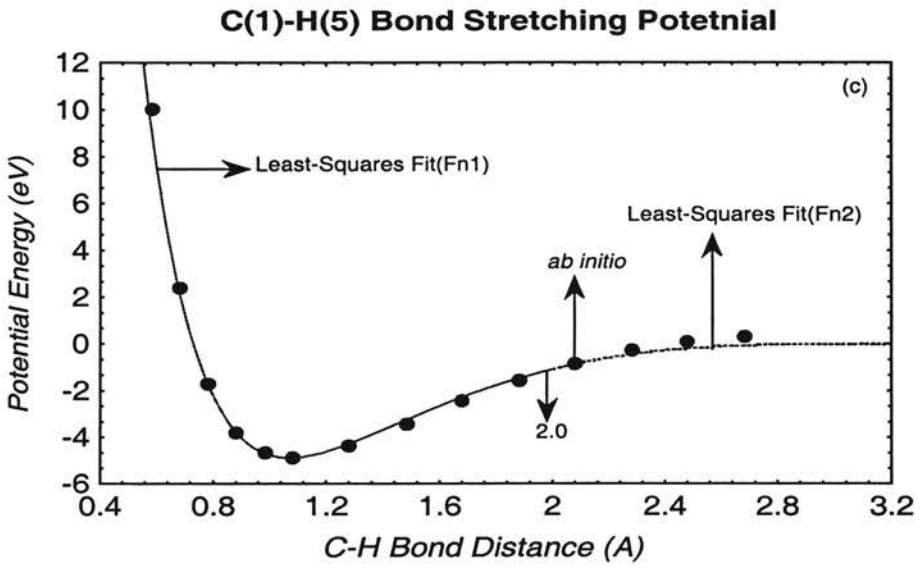

Figures 2.4a-c show the bond stretching potentials for three C-H bonds respectively. The filled circles are *ab intio* data points. Solid and dotted lines in the figures indicate the least-squares fit to those data whose functional forms are represented by Eq.2.35 and 2.36, respectively.

In Table 2.7a-c, three C-H bond stretching potentials are presented (in hartree) respectively. In the column titled 'shifted potential' we have performed the same data conversion as in Table 2.4.

Table 2.7a

C(2)-H(3) bond Distance	*ab intio* potential energy(hartree)	Shifted potential energy(eV)
0.5787	-2647.33903	10.2335676559926
0.6787	-2647.62424	2.47112116999435
0.7787	-2647.77588	-1.65600405400235
0.8787	-2647.85245	-3.73997911599488
0.9787	-2647.88579	-4.64738055999239
1.0787	-2647.89419	-4.87600000000000
1.2787	-2647.87504	-4.35480210999574
1.4787	-2647.83916	-3.37827050199464
1.6787	-2647.80255	-2.38187077600358
1.8787	-2647.77088	-1.51992105399747
2.0787	-2647.74568	-0.834062734003761
2.2787	-2647.72687	-0.322118488005596
2.4787	-2647.71406	0.026526158010005
2.6787	-2647.70683	0.223302175993216

Table 2.7b

C(1)-H(4) bond Distance	*ab intio* potential energy(hartree)	Shifted potential energy(eV)
0.4811	-2646.82718	24.1643843659878
0.5811	-2647.34824	9.98290277000726
0.6811	-2647.62846	2.35626711800089
0.7811	-2647.77757	-1.70200010800525
0.8811	-2647.85293	-3.75304308399407
0.9811	-2647.88582	-4.64819705800235
1.0811	-2647.89419	-4.87600000000000
1.2811	-2647.87551	-4.36759391199646
1.4811	-2647.84023	-3.40739226399071
1.6811	-2647.80398	-2.42079051400267
1.8811	-2647.77237	-1.56047378800192
2.0811	-2647.74695	-0.868627816012828
2.2811	-2647.72779	-0.347157759995549
2.4811	-2647.71463	0.011012695995508
2.6811	-2647.70720	0.213232034006272

Table 2.7c

C(1)-H(5) bond Distance	*ab intio* potential energy(hartree)	Shifted potential energy(eV)
0.58000	-2647.34464	10.0808825300084
0.68000	-2647.62676	2.40253533800226
0.78000	-2647.77684	-1.68213199000072
0.88000	-2647.85270	-3.74678326600022
0.98000	-2647.88579	-4.64738055999239
1.08000	-2647.89419	-4.87600000000000
1.28000	-2647.87528	-4.36133409400261
1.48000	-2647.83955	-3.38888497600763
1.68000	-2647.80276	-2.38758626200049
1.88000	-2647.77059	-1.51202823999827
2.08000	-2647.74466	-0.806301802000031
2.28000	-2647.72505	-0.272584276008071
2.48000	-2647.71151	0.095928487997502
2.68000	-2647.70373	0.307673635998275

Table2.7a-c: The above three tables show the *ab initio* potential energy in hartree at various C—H bond distances for three different C—H bonds namely C—H^3, C—H^4, and C—H^5. *ab initio* data are converted to generate the potential energy in eV in the same way as in Table2.4. And atom numbers are given in the parenthesis.

The angular terms, $V_{\alpha\beta\gamma}(\theta_i)$ (i = 1 – 6), represent the bending potentials for the θ_i defined in Fig. 2.1. These terms are written as

$$V_{\alpha\beta\gamma}(\theta_i) = 0.5k_{\alpha\beta\gamma}[\theta_i - \theta_i^o]^2, \quad (2.40)$$

where

$$k_{\alpha\beta\gamma} = k_i^o S_2(R_u, R_v) \quad (2.41)$$

The $S_2(R_u,R_v)$ function in Eq. 2.41 attenuates the bending potentials as either R_u or R_v becomes large. It is clear from Fig 2.1 that C=C bond is common to all angles. Since the

C=C bond does not rupture in any energetically open reaction channel we have assumed that $S_2(R_u,R_v)$ can be written as $S_2(R_v)$. The $S_2(R_v)$ has the functional form

$$S_2(R_v) = 1.0 - \tanh[a_3^k(R_v - R_v^o)^j], \quad (2.42)$$

where R_v and R_v^o represent the bond distances other than C=C forming angle θ_i in vinyl bromide. For the C-Br bond, R_{12}, j=1 and for all other bonds j=2. The force constants k_i^o are given by

$$k_1^o = xk_7^o + (xk_1^o - xk_7^o)S_1(R_{12}), \quad (2.43)$$

$$k_2^o = xk_8^o + (xk_2^o - xk_8^o)S_1(R_{12}), \quad (2.44)$$

$$k_3^o = xk_9^o + (xk_3^o - xk_9^o)S_1(R_{12}), \quad (2.45)$$

$$k_4^o = xk_{10}^o + (xk_4^o - xk_{10}^o)S_1(R_{12}), \quad (2.46)$$

$$k_5^o = xk_5^o, \quad (2.47)$$

$$\text{and } k_6^o = xk_6^o \quad (2.48)$$

The equilibrium angles in Eq. 2.40 are defined as

$$\theta_1^o = \Theta_7^o + (\Theta_1^o - \Theta_7^o)S_1(R_{12}), \quad (2.49)$$

$$\theta_2^o = \Theta_8^o + (\Theta_2^o - \Theta_8^o)S_1(R_{12}), \quad (2.50)$$

$$\theta_3^o = \Theta_9^o + (\Theta_3^o - \Theta_9^o)S_1(R_{12}), \quad (2.51)$$

$$\theta_4^o = \Theta_{10}^o + (\Theta_4^o - \Theta_{10}^o)S_1(R_{12}), \quad (2.52)$$

$$\theta_5^o = \Theta_5^o, \quad (2.53)$$

$$\text{and } \theta_6^o = \Theta_6^o, \quad (2.54)$$

where xk_i^o and Θ_i^o for $i \leq 6$ are the bending force constants and equilibrium angles, respectively, for vinyl bromide and xk_i^o and Θ_i^o for $i > 6$ are the corresponding constants for the vinyl radical. The following Figures 2.5-2.8 and Tables 2.8-2.11 show the potential energy for bending motions for various angles.

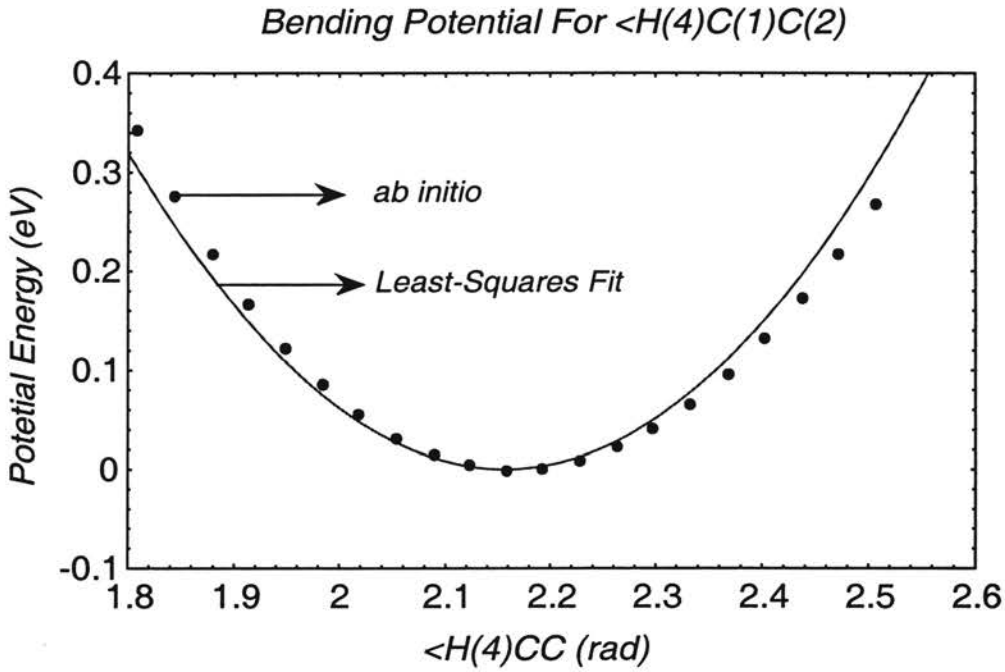

Figure 2.5 Shows the variation of potential with <H(4)CC angle. The number in the parenthesis is atom number. The filled circles are *ab initio* data points and solid line is the least-squares fit to those data.

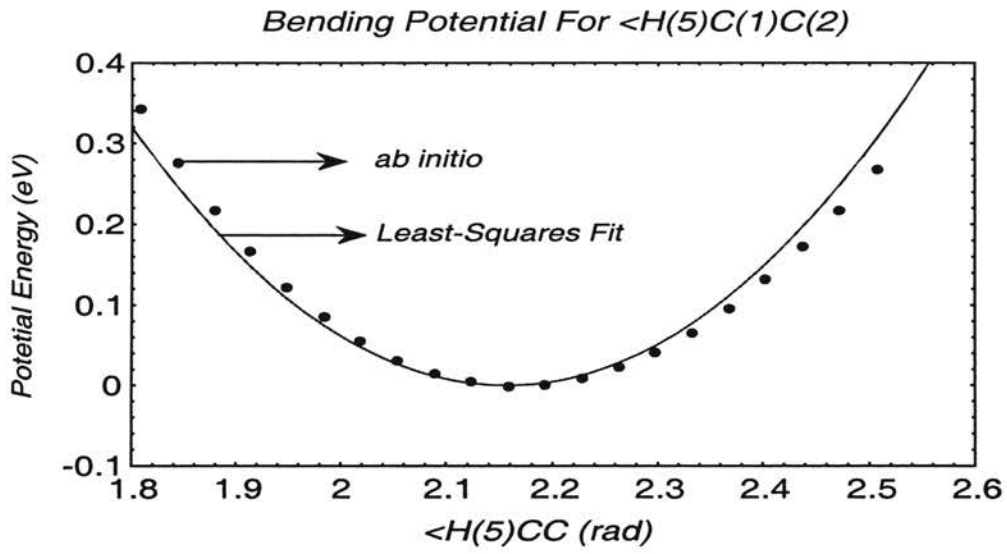

Figure2.6 Shows the variation of potential with <H(5)CC angle. The number in the parenthesis is atom number. The filled circles are *ab initio* data points and solid line is the least-squares fit to those data.

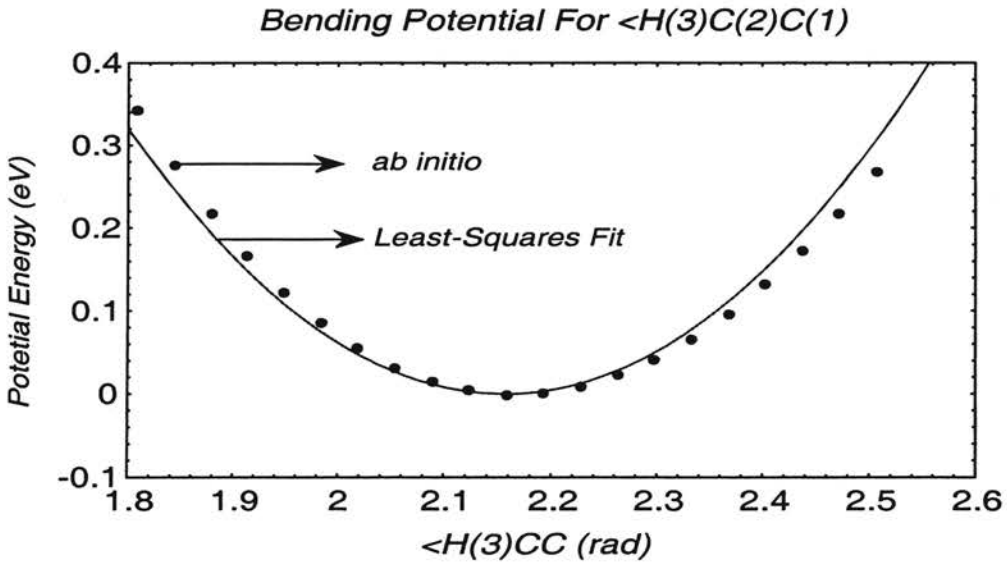

Figure2.7 Shows the variation of potential with <H(3)CC angle. The number in the parenthesis is atom number. The filled circles are *ab initio* data points and solid line is the least-squares fit to those data.

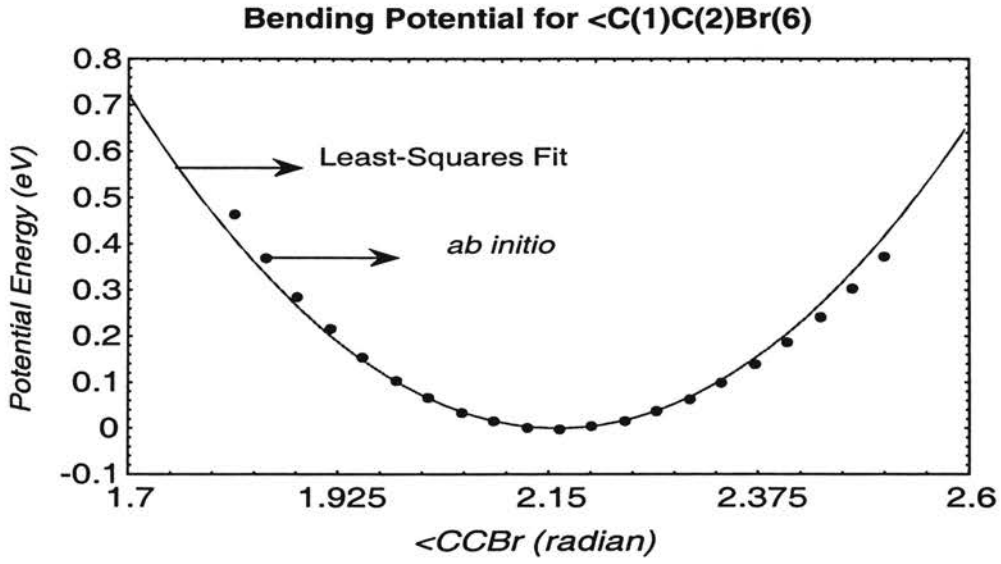

Figure2.8 Shows the variation of potential with <CCBr angle. The number in the parenthesis is atom number. The filled circles are *ab initio* data points and solid line is the least-squares fit to those data.

Table 2.8

<C(2)C(1)H(4) (degree)	*ab intio* potential energy(hartree)	Shifted potential Energy(eV)
103.61530	-2647.88160	0.342384827992646
105.61530	-2647.88403	0.276248490001308
107.61530	-2647.88618	0.217732799996156
109.61530	-2647.88806	0.166565591993276
111.61530	-2647.88968	0.122474699994200
113.61530	-2647.89104	8.546012399892788E-002
115.61530	-2647.89215	5.524969799444079E-002
117.61530	-2647.89301	3.184342200984247E-002
119.61530	-2647.89363	1.496913000300992E-002
121.61530	-2647.89402	4.354655990027823E-003
123.61530	-2647.89418	0.000000000000000E+000
125.61530	-2647.89412	1.632996005355380E-003
127.61530	-2647.89384	9.253643991542049E-003
129.61530	-2647.89334	2.286194400221575E-002
131.61530	-2647.89263	4.218573000980541E-002
133.61530	-2647.89172	6.695283600129187E-002
135.61530	-2647.89062	9.689109599275980E-002
137.61530	-2647.88931	0.132544841995696
139.61530	-2647.88782	0.173097576000146
141.61530	-2647.88614	0.218821464004577
143.61530	-2647.88429	0.269172173997504

Table 2.9

<C(2)C(1)H(5) (degree)	*ab intio* potential energy(hartree)	Shifted potential Energy(eV)
102.27060	-2647.88206	0.330137358003412
104.27060	-2647.88444	0.265361850004410
106.27060	-2647.88655	0.207934823993128
108.27060	-2647.88838	0.158128445997136
110.27060	-2647.88995	0.115398383990396
112.27060	-2647.89127	7.947247200354468E-002
114.27060	-2647.89233	5.062287599139381E-002
116.27060	-2647.89314	2.857742999913171E-002
118.27060	-2647.89372	1.279180200072005E-002
120.27060	-2647.89407	3.265992010710761E-003
122.27060	-2647.89419	0.000000000000000E+000
124.27060	-2647.89409	2.721659999224357E-003
126.27060	-2647.89377	1.143097199383192E-002
128.27060	-2647.89325	2.558360400144011E-002
130.27060	-2647.89252	4.545172200596426E-002
132.27060	-2647.89160	7.049099399591796E-002
134.27060	-2647.89048	0.100973585998872
136.27060	-2647.88918	0.136355165988789
138.27060	-2647.88769	0.176907899993239
140.27060	-2647.88603	0.222087456000736
142.27060	-2647.88420	0.271893833996728

Table 2.10

<C(1)C(2)H(3) (degree)	*ab intio* potential energy(hartree)	Shifted potential Energy(eV)
99.51410	-2647.88241	0.320611547998851
101.51410	-2647.88469	0.258557699999074
103.51410	-2647.88672	0.203308002004633
105.51410	-2647.88849	0.155134619999444
107.51410	-2647.89001	0.113765387999592
109.51410	-2647.89128	7.920030600507744E-002
111.51410	-2647.89232	5.089504200441297E-002
113.51410	-2647.89313	2.884959599759895E-002
115.51410	-2647.89370	1.333613399765454E-002
117.51410	-2647.89405	3.810324007645249E-003
119.51410	-2647.89419	0.000000000000000E+000
121.51410	-2647.89410	2.449494000757113E-003
123.51410	-2647.89381	1.034230799996294E-002
125.51410	-2647.89331	2.395060799608473E-002
127.51410	-2647.89260	4.327439398912247E-002
129.51410	-2647.89170	6.776933399669360E-002
131.51410	-2647.89061	9.743542800424621E-002
133.51410	-2647.88932	0.132544841995696
135.51410	-2647.88785	0.172553244003211
137.51410	-2647.88620	0.217460633997689
139.51410	-2647.88437	0.267267011993681

Table 2.11

<C(1)C(2)Br(6) (degree)	*ab intio* potential energy(hartree)	Shifted potential Energy(eV)
103.79680	-2647.87717	0.463226531996042
105.79680	-2647.88064	0.368784930004040
107.79680	-2647.88367	0.286318631988252
109.79680	-2647.88628	0.215283305995399
111.79680	-2647.88848	0.155406785997911
113.79680	-2647.89030	0.105872574000387
115.79680	-2647.89175	6.640850400435738E-002
117.79680	-2647.89285	3.647024399833754E-002
119.79680	-2647.89362	1.551346199994441E-002
121.79680	-2647.89406	3.538157994626090E-003
123.79680	-2647.89419	0.000000000000000E+000
125.79680	-2647.89401	4.898988001514226E-003
127.79680	-2647.89355	1.741862400376704E-002
129.79680	-2647.89282	3.728674199373927E-002
131.79680	-2647.89181	6.477550799900200E-002
133.79680	-2647.89053	9.961275599198416E-002
135.79680	-2647.88901	0.140981988006388
137.79680	-2647.88724	0.189155369997025
139.79680	-2647.88522	0.244132901992998
141.79680	-2647.88298	0.305098085998907
143.79680	-2647.88051	0.372323087998666

Tables 2.8-2.11 Show the variation of potential energy for the bending motion for four different angles. The numbers in the parenthesis indicate the atom number. In the column shifted potential we have shifted the equilibrium potential energy to zero and converted in eV.

We have also performed *ab initio* energy calculations to obtain the data points for the switching functions $S_2(R_v)$. At each point, the bond, R_v, is stretched from its equilibrium position, the geometry of the molecule is optimized and energy (E_i) is calculated. Keeping the same optimized geometry, the angle associated with the bond is

changed by 2^{o} and the energy (E_f) is calculated again (single point calculation). We calculate the data points (D_i) for the $S_2(R_v)$ in the following way:

$$D_i = \frac{E_f - E_i}{E_f^{eq} - E_i^{eq}}, \tag{2.55}$$

where E_i^{eq} is the energy of the molecule in its equilibrium geometry and E_f^{eq} is the energy when the angle (which is associated with the bond, R_v) is changed by 2^{o} from its equilibrium keeping the other internal coordinates in their equilibrium values. We have plotted these switching functions, $S_2(R_v)$, in the following Figures 2.10a-d for four different bonds and the corresponding *ab initio* data points are given in Tables 2.12a-d .

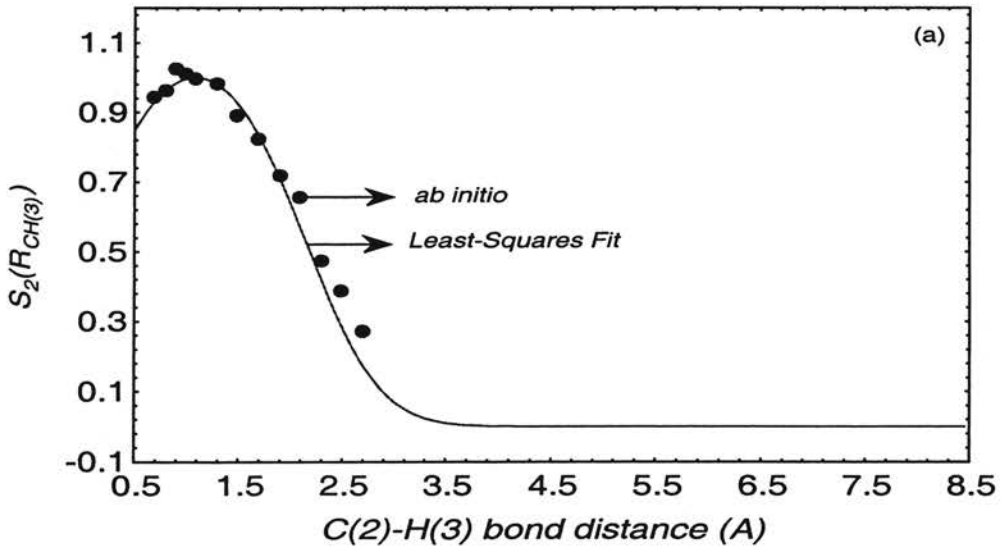

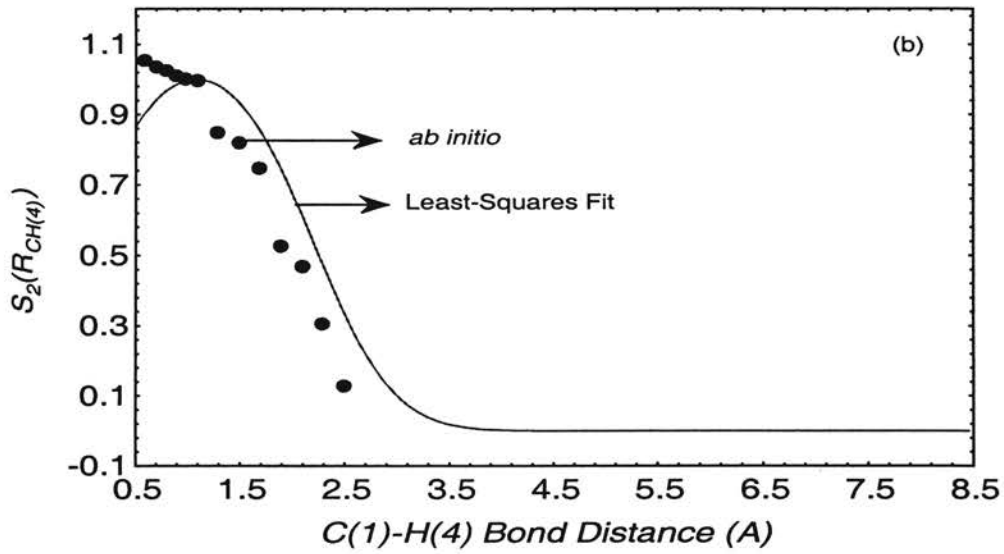
(b)
ab initio
Least-Squares Fit
$S_2(R_{CH(4)})$
1.1
0.9
0.7
0.5
0.3
0.1
-0.1
0.5
1.5
2.5
3.5
4.5
5.5
6.5
7.5
8.5
C(1)-H(4) Bond Distance (A)

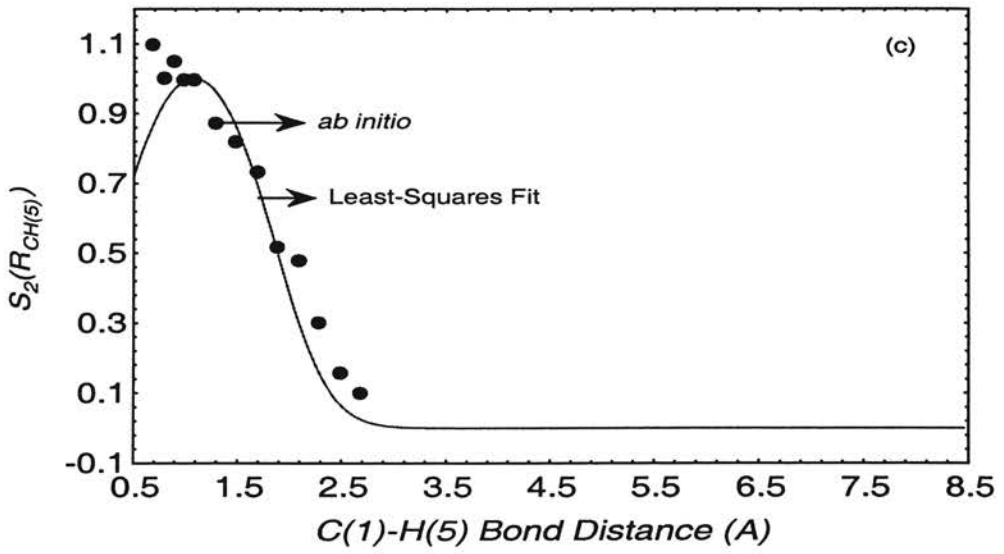
(c)
ab initio
Least-Squares Fit
$S_2(R_{CH(5)})$
1.1
0.9
0.7
0.5
0.3
0.1
-0.1
0.5
1.5
2.5
3.5
4.5
5.5
6.5
7.5
8.5
C(1)-H(5) Bond Distance (A)

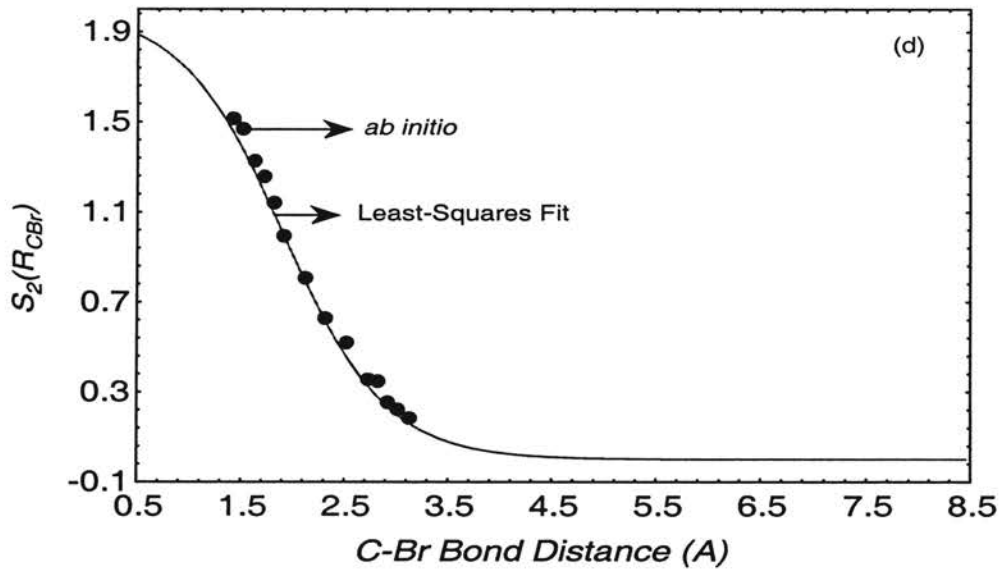

Figure 2.9a-d Show the plots for the switching functions $S_2(R_v)$ versus R_v for different bonds C-H[3], C-H[4], C-H[5] and CBr.

Table 2.12a

C(2)-H(3) Bond Distance(Å)	E_i	E_f	D_i
0.67870	-2647.62424	-2647.6240981	0.946631087525165
0.77870	-2647.77588	-2647.7757352	0.965977320041654
0.87870	-2647.85245	-2647.8522963	1.02535023236376
0.97870	-2647.88579	-2647.8856384	1.01134089230822
1.07870	-2647.89419	-2647.8940401	1.00000000000000
1.27870	-2647.87504	-2647.8748923	0.985323549524471
1.47870	-2647.83916	-2647.8390259	0.894596398923986
1.67870	-2647.80255	-2647.8024261	0.826551032939950
1.87870	-2647.77088	-2647.7707721	0.719813207990280
2.07870	-2647.74568	-2647.7455813	0.658438958340853
2.27870	-2647.72687	-2647.726799	0.473649098972579
2.47870	-2647.71406	-2647.7140019	0.387591727379382
2.67870	-2647.70683	-2647.7067886	0.276184123422423

Table 2.12b

C(1)-H(4) Bond Distance(Å)	E_i	E_f	D_i
0.58110	-2647.34824	-2647.3480932	1.05384063045755
0.68110	-2647.62846	-2647.6283156	1.03661163093101
0.78110	-2647.77757	-2647.7774268	1.02799713279999
0.88110	-2647.85293	-2647.8527889	1.01292175209330
0.98110	-2647.88582	-2647.8856803	1.00287150264152
1.08110	-2647.89419	-2647.8940507	1.00000000000000
1.28110	-2647.87551	-2647.8753916	0.849964106135368
1.48110	-2647.84023	-2647.8401158	0.819813351251010
1.68110	-2647.80398	-2647.8038754	0.750897346615799
1.88110	-2647.77237	-2647.7722965	0.527638194153673
2.08110	-2647.74695	-2647.7468841	0.473079686403484
2.28110	-2647.72779	-2647.7277469	0.309404163152916
2.48110	-2647.71463	-2647.714612	0.129217514403927

Table 2.12c

C(1)-H(5) Bond Distance(Å)	E_i	E_f	D_i
0.68000	-2647.62676	-2647.6266012	1.09744298581517
0.78000	-2647.77684	-2647.7766947	1.00414651016842
0.88000	-2647.85270	-2647.8525477	1.05252246108575
0.98000	-2647.88579	-2647.8856454	0.999308912876803
1.08000	-2647.89419	-2647.8940453	1.00000000000000
1.28000	-2647.87528	-2647.8751533	0.875604701232797
1.48000	-2647.83955	-2647.8394315	0.818935729978628
1.68000	-2647.80276	-2647.8026537	0.734623358649226
1.88000	-2647.77059	-2647.7705148	0.519695923299992
2.08000	-2647.74466	-2647.7445904	0.480995160680514
2.28000	-2647.72505	-2647.7250063	0.302004145743352
2.48000	-2647.71151	-2647.7114873	0.156876296134052
2.68000	-2647.70373	-2647.7037154	0.100898412003080

Table 2.12d

C(2)-Br Bond Distance (Å)	E_i	E_f	D_i
1.4149	-2647.69300	-2647.6927103	1.52073491086821
1.5149	-2647.78776	-2647.7874801	1.46929134106378
1.6149	-2647.84382	-2647.8435665	1.33070866132334
1.7149	-2647.87490	-2647.8746595	1.26246719224639
1.8149	-2647.88977	-2647.8895526	1.14120735015902
1.9149	-2647.89416	-2647.8939695	1.00000000000000
2.1149	-2647.88536	-2647.8852064	0.806299215211106
2.3149	-2647.86601	-2647.8658892	0.634120736925602
2.5149	-2647.84406	-2647.843961	0.519685038881376
2.7149	-2647.82292	-2647.8228522	0.355905512619263
2.8149	-2647.81312	-2647.8130538	0.347506560595872
2.9149	-2647.80391	-2647.8038608	0.258267716234693
3.0149	-2647.79536	-2647.7953165	0.228346457707912
3.1149	-2647.78748	-2647.7874445	0.186351704752334

Table2.12a-d. Represent the data points obtained for the switching functions $S_2(R_v)$. Data in the column D_i is calculated using Eq. 2.55.

Table 2.13

Definitions of dihedral angles in vinyl bromide and vinyl radical

Dihedral Angle	Atoms i-j-k-m			
	i	j	k	m
ϕ_1	4	1	2	3
ϕ_2	4	1	2	6
ϕ_3	5	1	2	3
ϕ_4	5	1	2	6

The $V_{ABCD}(\phi_i)$ functions represent dihedral interactions for different dihedral angles formed by four atoms with a common bond. The dihedral angles, ϕ_i (i = 1–4) are defined in Table 2.13. The four dihedral interactions are given by

$$V_{ABCD}(\phi_1) = V_1^{o}S_{31}(R_3)S_{31}(R_2)Sum(\phi_1)T_1, \quad (2.56)$$

$$V_{ABCD}(\phi_2) = V_1^{o}S_{32}(R_3)S_{32}(R_{12})Sum(\phi_2)T_2, \quad (2.57)$$

$$V_{ABCD}(\phi_3) = V_1^{o}S_{33}(R_7)S_{33}(R_{12})Sum(\phi_3)T_3, \quad (2.58)$$

$$\text{and } V_{ABCD}(\phi_4) = V_1^{o}S_{34}(R_7)S_{34}(R_2)Sum(\phi_4)T_4 \quad (2.59)$$

With

$$V_1^{o} = \Delta_5^{o} + (\Delta_1^{o} - \Delta_5^{o})S_1(R_{12}), \quad (2.60)$$

$$V_2^{o} = \Delta_6^{o} + (\Delta_2^{o} - \Delta_6^{o})S_1(R_{12}), \quad (2.61)$$

$$V_3^{o} = \Delta_7^{o} + (\Delta_3^{o} - \Delta_7^{o})S_1(R_{12}), \quad (2.62)$$

$$V_4^{o} = \Delta_8^{o} + (\Delta_4^{o} - \Delta_8^{o})S_1(R_{12}), \quad (2.63)$$

and

$$Sum(\phi_i) = \sum_{j=0}^{6} b_j \cos(j\phi_i). \quad (2.64)$$

The $S_{3i}(R_v)$ are switching functions which attenuate V_i^{o} as R_v becomes large. Each dihedral potential has two switching functions which ensures that if one of the bonds dissociates, the dihedral potential will vanish. These switching functions are written as

$$S_{31}(R_2) = 1.0 - \tanh[0.13(R_2 - R_{33}^{o})], \quad (2.65a)$$

$$S_{31}(R_3) = 1.0 - \tanh[0.5(R_3 - R_{34}^{o})], \quad (2.65b)$$

$$S_{32}(R_3) = 1.0 - \tanh[0.5(R_3 - R_{34}^{o})], \quad (2.66a)$$

$$S_{32}(R_{12}) = 1.0 - \tanh[0.55(R_{12} - R_2^{o})], \quad (2.66b)$$

$$S_{33}(R_7) = 1.0 - \tanh[0.25(R_7 - R_{35}^{o})], \quad (2.67a)$$

$$S_{33}(R_2) = 1.0 - \tanh[0.22(R_2 - R_{33}^{o})], \quad (2.67b)$$

$$S_{34}(R_{12}) = 1.0 - \tanh[0.55(R_{12} - R_2^{o})], \quad (2.68a)$$

$$\text{and } S_{34}(R_7) = 1.0 - \tanh[0.16(R_7 - R_{35}^{o})], \quad (2.68b)$$

where the parameters are obtained by fitting the *ab initio* data. In Eqs. 2.56-2.59, for $i \leq 4$, the Δ_i^o determine the magnitude of the dihedral potential in vinyl bromide. For $i > 4$, the Δ_i^o determine the corresponding potential for the vinyl bromide radical. T_i values help us adjust the vibrational frequencies and T_i are set to 1.0 initially. The functional form of the dihedral potential for vinyl radical are kept similar to that used by Abrash *et al.*[3] The parameters for the Channel I potential are given in Table 2.14 (in the next page).

The following Figures2.10a-b, show the variations of potential energy with different dihedral angles. The *ab initio* data points are calculated by rotating the molecule along C=C bond with an increment of 5^0 keeping the molecule in its equilibrium geometry. This enables us to determine the change in potential energy due to the change in dihedral angles. As dihedral angles are coupled, it is very difficult to determine the contribution of each dihedral angle to the total potential. So we have assumed that each dihedral angle makes equal contribution towards the total potential energy. We have used a seven-term cosine series to fit the data points which is given as line in the Figure 2.10a-b. The filled circles in the Figures 2.10a-b are the *ab initio* data points. In Tables 2.15a-b, potential energy at different dihedral angles are given.

In Figures 2.11-2.16, we have also plotted the S_{3i} type switching functions for bonds R_2, R_3, R_7 and R_{12} to attenuate the V_i^o, dihedral potential. The data points for these switching functions are given in Tables 2.16-2.21. The *ab initio* data points are altered in the same way as in the case of S_2 type switching function given by Eq. 2.55 by replacing $S_2(R_v)$ with $S_{3I}(R_v)$. With vinyl bromide in its equilibrium geometry, energy of the system (E_i^{eq}) is computed. One of the dihedral angles (ϕ_1, ϕ_3 or ϕ_4) is then changed by 5^o and the

new system energy (E_f^{eq}) is calculated. The bond distance R_v is then altered to a new value and the above calculation is repeated to obtain E_i and E_f.

Table 2.14

Potential parameters for the Channel I potential

Parameter	Value		Parameter	Value	
	PES1	PES2/PES3		PES1	PES2/PES3
D_1	4.959	4.959 eV	Δ_5^o	1.100	1.100 eV
D_2	3.339	3.339 eV	Δ_6^o	0.000	0.000 eV
D_3	4.786	4.786 eV	Δ_7^o	0.000	0.000 eV
D_4	5.197	5.197 eV	Δ_8^o	1.100	1.100 eV
D_5	4.786	4.786 eV	Θ_1^o	2.086000	2.086000 rad
α_1	2.500	2.180 $Å^{-1}$	Θ_2^o	2.134000	2.134000 rad
α_2	1.459	1.599 $Å^{-1}$	Θ_3^o	2.058342	2.058342 rad
α_{33}	2.000	1.775 $Å^{-1}$	Θ_4^o	2.157000	2.157000 rad
α_{34}	2.000	1.775 $Å^{-1}$	Θ_5^o	2.160000	2.160000 rad
α_{35}	2.000	1.775 $Å^{-1}$	Θ_6^o	1.960720	1.960720 rad
α_{53}	1.981	1.981 $Å^{-1}$	Θ_7^o	2.122320	2.122320 rad
α_{54}	1.990	1.990 $Å^{-1}$	Θ_8^o	2.127556	2.127556 rad
α_{55}	2.030	2.030 $Å^{-1}$	Θ_9^o	2.033309	2.033309 rad
α_4	2.350	2.350 $Å^{-1}$	Θ_{10}^o	2.363180	2.363180 rad
a_2	1.9229	1.9229 Å	xk_1^o	4.82270	5.304970 eV/rad^2
a_3^1	0.4000	0.4000 $Å^{-2}$	xk_2^o	4.93756	5.875696 eV/rad^2
a_3^2	0.7500	0.7500 $Å^{-2}$	xk_3^o	0.00000	0.450370 eV/rad^2
a_3^3	0.4000	0.4000 $Å^{-2}$	xk_4^o	5.01250	3.308250 eV/rad^2
a_3^4	0.4500	0.4500 $Å^{-2}$	xk_5^o	6.82044	6.615827 eV/rad^2
a_3^5	1.0000	1.0000 $Å^{-2}$	xk_6^o	0.00000	0.0000001 eV/rad^2
a_3^6	1.0000	1.0000 $Å^{-2}$	xk_7^o	3.80000	3.80000 eV/rad^2
R_1^o	1.3307	1.3035 Å	xk_8^o	3.80000	3.80000 eV/rad^2
R_4^o	1.342	1.342 Å	xk_9^o	2.45000	2.45000 eV/rad^2
Δ_1^o	1.000	1.000 eV	xk_{10}^o	4.60000	4.60000 eV/rad^2
Δ_2^o	1.000	1.000 eV	b_0	0.33250	0.33250
Δ_3^o	1.000	1.000 eV	b_1	0.00000	0.00000
Δ_4^o	1.000	1.000 eV	b_2	-0.40250	- 0.40250
R_2^o	1.9229	1.9229 Å	b_3	0.00000	0.00000
R_{53}^o	1.097	1.097 Å	b_4	0.10275	0.10275
R_{55}^o	1.099	1.099 Å	b_5	0.00000	0.00000
R_{54}^o	1.105	1.105 Å	b_6	-0.03275	-0.03275
T_1	1.000	0.580	T_3	1.00000	0.98000
T_2	1.000	0.890	T_4	1.00000	0.85000

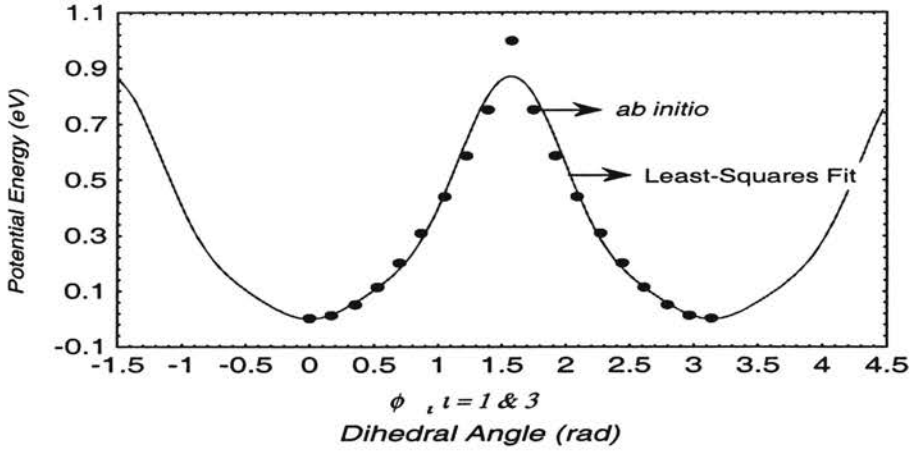

Figure 2.10a Shows the plot of potential energy versus dihedral angle. The plot is similar for the dihedral angle ϕ_1 and ϕ_3. The filled circles are obtained from *ab initio* calculation and the line is the least –squares fit to those data points with a six-term cosine series.

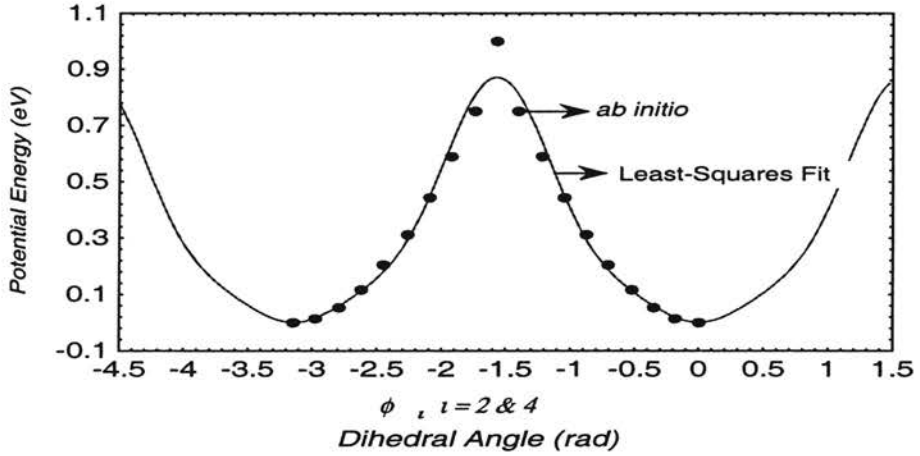

Figure 2.10b Shows the plot of potential energy versus dihedral angle. The plot is similar for the dihedral angle ϕ_2 and ϕ_4. The filled circles are obtained from *ab initio* calculation and the line is the least –squares fit to those data points with a six-term cosine series.

Table 2.15

Potential energy for different dihedral angles

ab initio	ϕ_1	ϕ_2	ϕ_3	ϕ_4	Potential Energy(eV)
-2647.8941900	00	-180	-180	00	0.00000000000000
-2647.8923050	10	-170	-170	10	0.05.13032910035
-2647.8866855	20	-160	-160	20	0.20424697469641
-2647.8774116	30	-150	-150	30	0.45665100144057
-2647.8646286	40	-140	-140	40	0.80456079924402
-2647.8485598	50	-130	-130	50	1.24189890131395
-2647.8295186	60	-120	-120	60	1.76013562523869
-2647.8079112	70	-110	-110	70	2.34821558807852
-2647.7841632	80	-100	-100	80	2.99455540488039
-2647.7473747	90	-90	-90	90	3.99581329398194
-2647.7841632	100	-80	-80	100	2.99455540488039
-2647.7841632	110	-70	-70	110	2.34821558807852
-2647.8295186	120	-60	-60	120	1.76013562523869
-2647.8485598	130	-50	-50	130	1.24189890131395
-2647.8646286	140	-40	-40	140	0.80456079924402
-2647.8774116	150	-30	-30	150	0.45665100144057
-2647.8866855	160	-20	-20	160	0.20424697469641
-2647.8923050	170	-10	-10	170	0.05130329100352
-2647.8941900	180	-00	-00	180	0.00000000000000

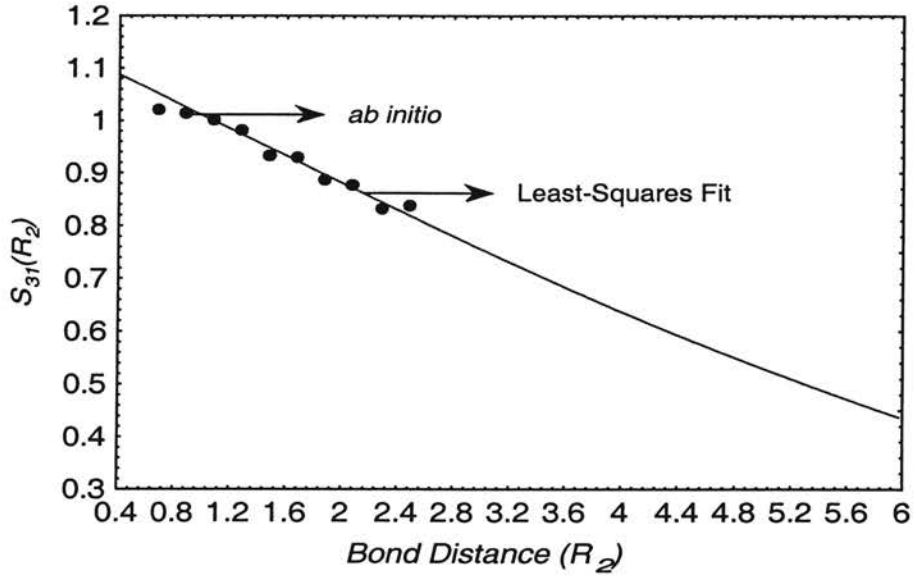

Figure 2.11 Plot of $S_{31}(R_2)$ versus R_2 for the dihedral angle H(3)C(2)C(1)H(4)

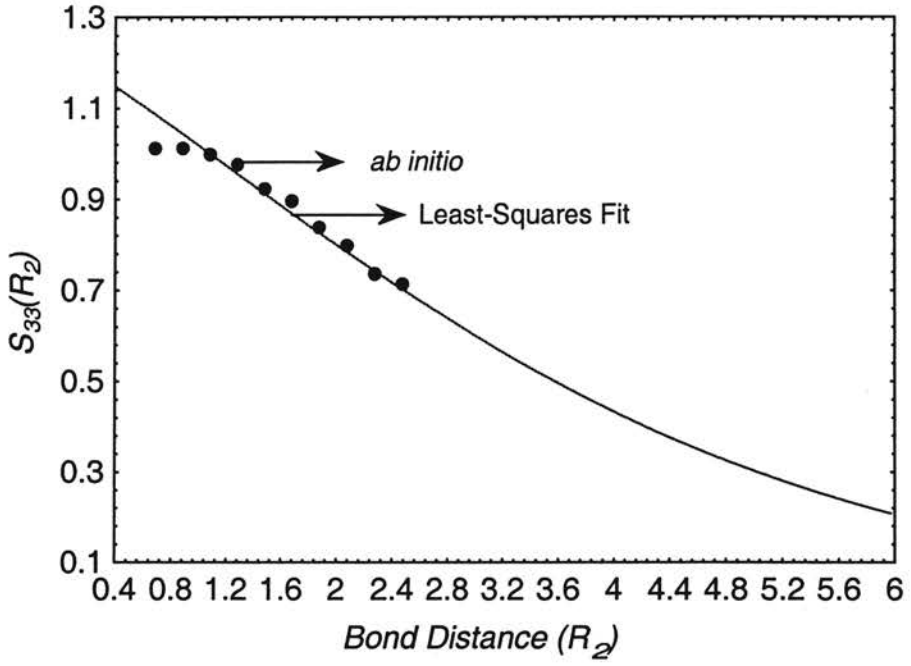

Figure 2.12 Plot of $S_{33}(R_2)$ versus R_2 for the dihedral angle H(3)C(2)C(1)H(5)

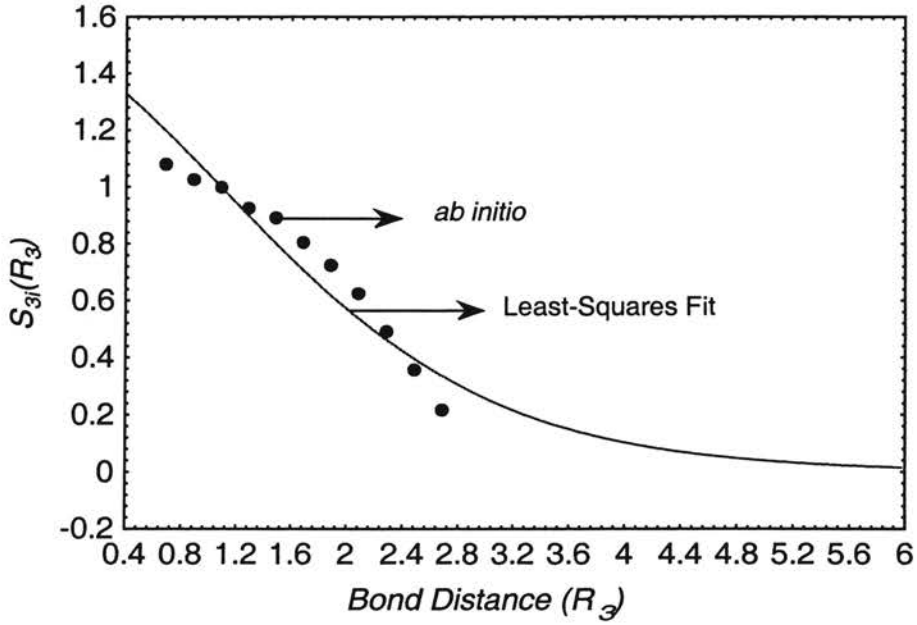

Figure 2.13 Plot of $S_{31}(R_3)$ and $S_{32}(R_3)$ versus R_3 for the dihedral angle H(3)C(2)C(1)H(4) and Br(6)C(2)C(1)H(4).

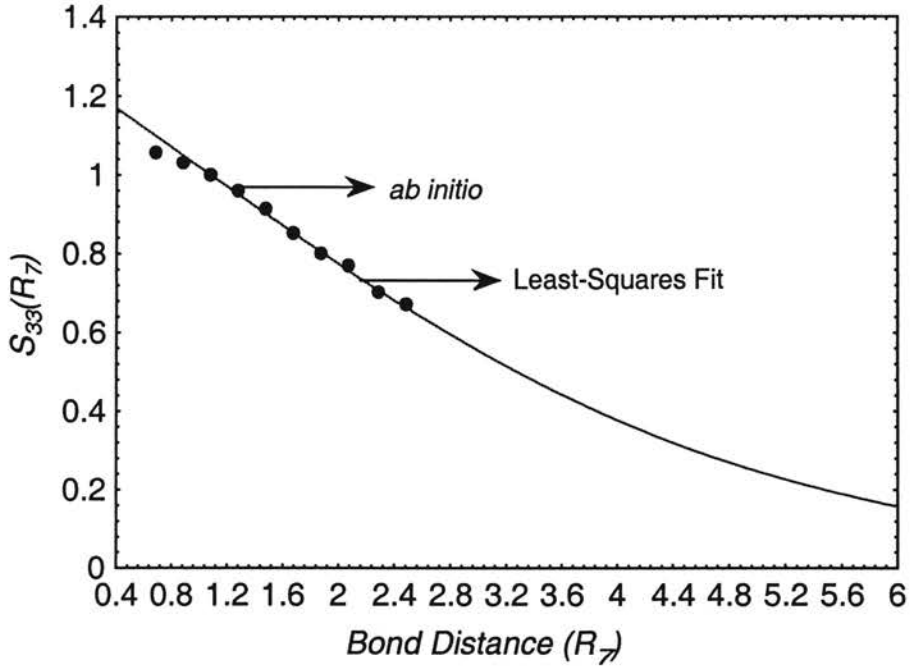

Figure2.14 Plot of $S_{33}(R_7)$ versus R_7 for the dihedral angle H(3)C(2)C(1)H(5)

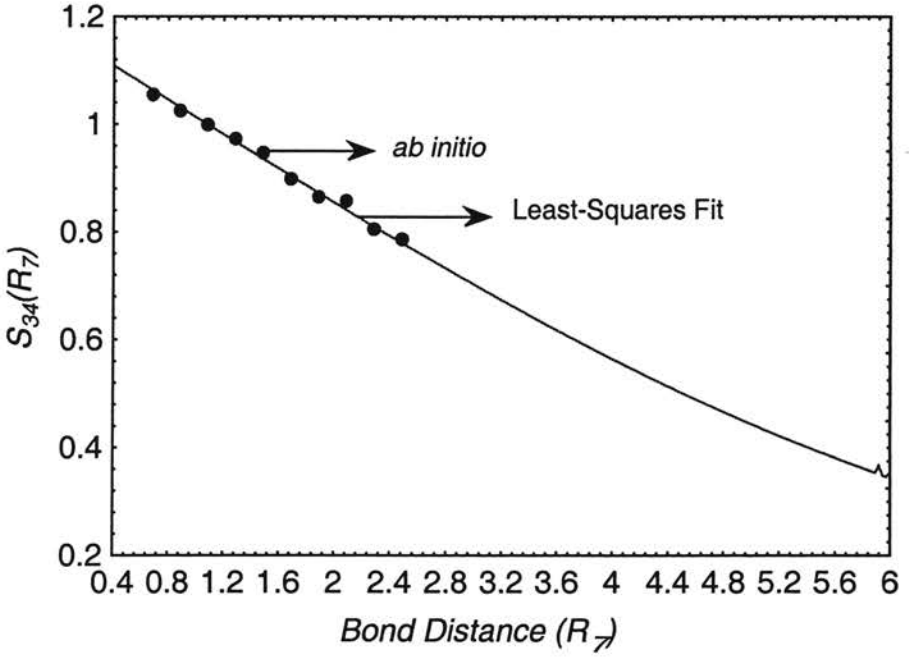

Figure 2.15 Plot of $S_{34}(R_7)$ versus R_7 for dihedral angle Br(6)C(2)C(1)H(5)

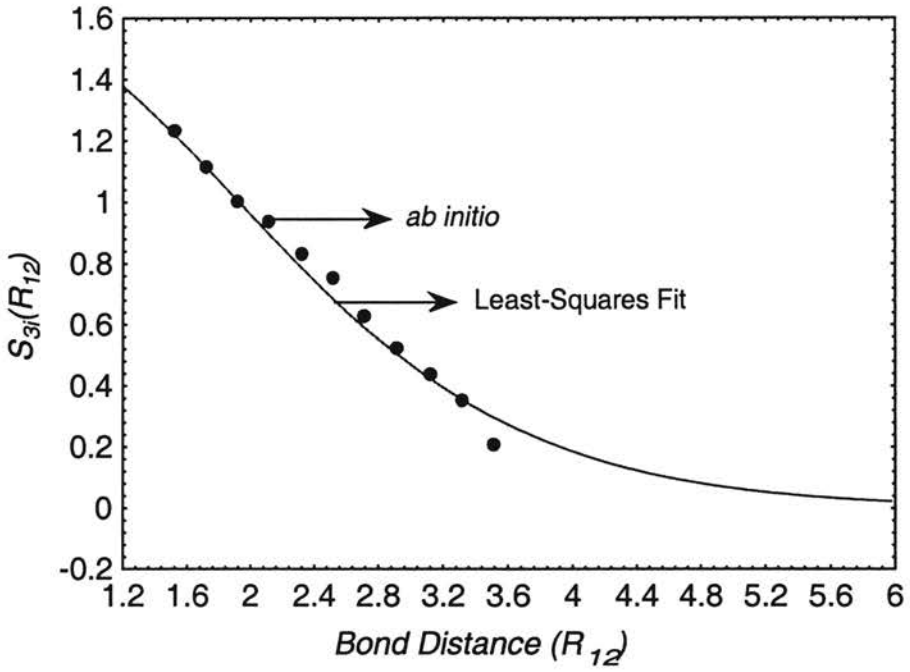

Figure 2.16 Plot of $S_{34}(R_{12})$ and $S_{32}(R_{12})$ versus R_{12} for dihedral angle H(5)C(1)C(2)Br(6) and H(4)C(1)C(2)Br(6)

Table 2.16 (Figure2.11)

Shows the data points for $S_{31}(R_2)$ for the dihedral angle H(3)C(2)C(1)H(4). The row with 'eq' indicates the data point associated with equilibrium geometry.

R_2, Bond Distance (Å)	E_i	E_f	D_i
0.67870	-2647.62424	-2647.6239617	1.01978746865139
0.87870	-2647.85245	-2647.8521736	1.01282521171839
1.07870	-2647.89419	-2647.8939171(eq)	1.00000000000000
1.27870	-2647.87504	-2647.8747724	0.980578967064171
1.47870	-2647.83916	-2647.8389055	0.932576036631581
1.67870	-2647.80255	-2647.8022966	0.928545255424922
1.87870	-2647.77088	-2647.7706378	0.887504581925332
2.07870	-2647.74568	-2647.7454408	0.876511543785673
2.27870	-2647.72687	-2647.7266433	0.830707219314663
2.47870	-2647.71406	-2647.7138314	0.837669476247663

Table 2.17(Figure2.12)

Shows the data points for $S_{33}(R_2)$ for the dihedral angle H(3)C(2)C(1)H(5). The row with 'eq' indicates the data point associated with equilibrium geometry.

R_2, Bond Distance (Å)	E_i	E_f	D_i
0.67870	-2647.62424	-2647.6238559	1.01025775943406
0.87870	-2647.85245	-2647.8520654	1.01157285600002
1.07870	-2647.89419	-2647.8938098(eq)	1.00000000000000
1.27870	-2647.87504	-2647.874669	0.975802209311900
1.47870	-2647.83916	-2647.8388086	0.924250394263681
1.67870	-2647.80255	-2647.8022089	0.897159388977538
1.87870	-2647.77088	-2647.7705614	0.837980010019321
2.07870	-2647.74568	-2647.7453764	0.798527090315151
2.27870	-2647.72687	-2647.7265907	0.734613360848905
2.47870	-2647.71406	-2647.7137889	0.713045764488797

Table 2.18(Figure2.13)

Shows the data points for $S_3(R_3)$ for the dihedral angles H(3)C(2)C(1)H(4) and Br(6)C(2)C(1)H(4). The row with 'eq' indicates the data point associated with equilibrium geometry.

R_3, Bond Distance (Å)	E_i	E_f	D_i
0.68110	-2647.62846	-2647.6281648	1.08092273902285
0.88110	-2647.85293	-2647.8526509	1.02196997514880
1.08110	-2647.89419	-2647.8939169(eq)	1.00000000000000
1.28110	-2647.87551	-2647.8752577	0.923837421704341
1.48110	-2647.84023	-2647.8399861	0.893079458161155
1.68110	-2647.80398	-2647.80376	0.805565728258792
1.88110	-2647.77237	-2647.7721723	0.723910656175933
2.08110	-2647.74695	-2647.7467801	0.622116442426852
2.28110	-2647.72779	-2647.7276561	0.490296594864325
2.48110	-2647.71463	-2647.7145326	0.356645917149485
2.68110	-2647.70720	-2647.7071413	0.214939582435130

Table 2.19(Figure2.14)

Shows the data points for $S_3(R_7)$ for the dihedral angle H(3)C(2)C(1)H(5). The row with 'eq' indicates the data point associated with equilibrium geometry.

R_4, Bond Distance (Å)	E_i	E_f	D_i
0.68000	-2647.62676	-2647.6263579	1.05732316596220
0.88000	-2647.85270	-2647.8523081	1.03050223536244
1.08000	-2647.89419	-2647.8938097(eq)	1.00000000000000
1.28000	-2647.87528	-2647.874916	0.957139100783856
1.48000	-2647.83955	-2647.8392025	0.913752301741443
1.68000	-2647.80276	-2647.8024367	0.850118328297942
1.88000	-2647.77059	-2647.7702863	0.798580068795011
2.08000	-2647.74466	-2647.744368	0.767814882323678
2.28000	-2647.72505	-2647.7247823	0.703917960162802
2.48000	-2647.71151	-2647.7112543	0.672363923952066

Table 2.20(Figure2.15)

Shows the data points for $S_3(R_7)$ for the dihedral angle Br(6)C(2)C(1)H(5). The row with 'eq' indicates the data point associated with equilibrium geometry.

R_7, Bond Distance (Å)	E_i	E_f	D_i
0.68000	-2647.62676	-2647.6264315	1.05288461577703
0.88000	-2647.85270	-2647.8523804	1.02435897326770
1.08000	-2647.89419	-2647.893878(eq)	1.00000000000000
1.28000	-2647.87528	-2647.8749767	0.972115385097489
1.48000	-2647.83955	-2647.8392546	0.946794871877091
1.68000	-2647.80276	-2647.8024798	0.898076922426643
1.88000	-2647.77059	-2647.7703199	0.865705128851671
2.08000	-2647.74466	-2647.7443928	0.856410256245818
2.28000	-2647.72505	-2647.7247991	0.804166666618082
2.48000	-2647.71151	-2647.7112651	0.784935896714610

Table 2.21(Figure2.16)

Shows the data points for $S_3(R_{12})$ for the dihedral angles Br(6)C(2)C(1)H(5) and Br(6)C(2)C(1)H(4). The row with 'eq' indicates the data point associated with equilibrium geometry.

R_{12}, Bond Distance (Å)	E_i	E_f	D_i
1.5149	-2647.78776	-2647.7873829	1.23517851328449
1.7149	-2647.87490	-2647.8745606	1.11169341478767
1.9149	-2647.89419	-2647.8938547 (eq)	1.00000000000000
2.1149	-2647.88536	-2647.885074	0.936783492894591
2.3149	-2647.86601	-2647.865757	0.828693089180826
2.5149	-2647.84406	-2647.8438305	0.751719619734099
2.7149	-2647.82292	-2647.8227284	0.627579430345903
2.9149	-2647.80391	-2647.8037496	0.525384866997199
3.1149	-2647.78748	-2647.7873459	0.439240090812435
3.3149	-2647.77399	-2647.7738831	0.350147395934651
3.5149	-2647.76424	-2647.764177	0.206354405329585

The three-center HBr elimination channel leading to HBr and vinylidene is written as

$$V_{VI} = V_{HBr}(R_{13}) + V_{C2H2}(R_1,R_3,R_5,R_7,R_8), \quad (2.69)$$

where the $V_{HBr}(R_{13})$ term is the simple Morse potential for HBr formed from the three-center HBr elimination reaction. The parameters for this potential are taken from the ref.15. The $V_{C2H2}(R_1,R_3,R_5,R_7,R_8)$ term is the vinylidene/acetylene potential. This potential has been previously fitted[3] to the results of ab initio calculations[16,17]. The functional form of V_{C2H2} is

$$V_{C2H2} = G_{CC}(R_1,R_3) + G_{CH4}(R_3,R_5) + G_{CH4}(R_7,R_3) + G_{CCH4}(\theta_5,R_3) + G_{CCH4}(\theta_7,R_3) + G(\Phi) \quad (2.70)$$

The term $G_{CC}(R_1,R_3)$ is a Morse type potential and written as

$$G_{CC}(R_1,R_3) = \epsilon_{CC}^{\circ} [\exp\{-2\omega_{CC}(R_1 - \sigma_{CC}^{\circ})\} - 2\exp\{-\omega_{CC}(R_1 - \sigma_{CC}^{\circ})\}] \quad (2.71)$$

With

$$\epsilon_{CC}^{\circ} = \epsilon^{cc}{}_{v} + (\epsilon^{cc}{}_{a} - \epsilon^{cc}{}_{v})S_{13}(R_3), \quad (2.72)$$

$$\omega_{CC}^{\circ} = \omega^{cc}{}_{v} + (\omega^{cc}{}_{a} - \omega^{cc}{}_{v})S_{13}(R_3), \quad (2.73)$$

and

$$\sigma_{CC}^{\circ} = \sigma^{cc}{}_{v} + (\sigma^{cc}{}_{a} - \sigma^{cc}{}_{v})S_{13}(R_3), \quad (2.74)$$

where the subscripts "$_v$" and "a" denote vinylidene and acetylene respectively. The switching function, $S_{13}(R_3)$ varies the C=C bond energy, equilibrium distance and curvature as the hydrogen atom 4 migrates from carbon atom 1 to carbon atom 2 to form the acetylene. The functional form of $S_{13}(R_3)$ is

$$S_{13}(R_3) = [\ 1.0 - \tanh\ \{b_1(R_3 - b_2)^2\}] \quad (2.75)$$

The $G_{CH4}(R_3,R_5)$ term represents the interactions between hydrogen atom 4 and two carbon atoms at points along the vinylidene → acetylene reaction coordinate. It is written as

$$G_{CH4}(R_3,R_5) = \epsilon_{CH}^{\circ} [\exp\{-2\omega_{CH}(R_3 - \sigma_{CH}^{\circ})\} - 2\exp\{-\omega_{CH}(R_3 - \sigma_{CH}^{\circ})\}]$$
$$+\epsilon'_{CH}{}^{\circ} [\exp\{-2\omega'_{CH}(R_5 - \sigma'_{CH}{}^{\circ})\} - 2\exp\{-\omega'_{CH}(R_5 - \sigma'_{CH}{}^{\circ})\}] \quad (2.76)$$

with

$$\epsilon_{CH}^{\circ} = \epsilon^{ch}{}_{v}S_{14}(R_5), \quad (2.77)$$

$$\omega_{CH}^{\circ} = \omega^{ch}{}_{v} + (\omega^{ch}{}_{a} - \omega^{ch}{}_{v})S_{13}(R_3), \quad (2.78)$$

$$\sigma_{CH}^{\circ} = \sigma^{ch}{}_{v} + (\sigma^{ch}{}_{a} - \sigma^{ch}{}_{v})S_{13}(R_3), \quad (2.79)$$

$$\epsilon'_{CH}{}^{\circ} = \epsilon^{ch}{}_{v}S_{15}(R_3), \quad (2.80)$$

$$\omega'_{CH}{}^{\circ} = \omega^{ch}{}_{v} + (\omega^{ch}{}_{a} - \omega^{ch}{}_{v})S_{13}(R_5), \quad (2.81)$$

and $\sigma'^{o}_{CH} = \sigma^{ch}_{v} + (\sigma^{ch}_{a} - \sigma^{ch}_{v})S_{13}(R_5)$. (2.82)

The switching functions $S_{14}(R_5)$ and $S_{15}(R_3)$ are given by

$S_{14}(R_5) = \tanh[b_3(R_5 - b_4)^2]$ (2.83)

and $S_{15}(R_3) = \tanh[b_5(R_3 - b_6)^2]$. (2.84)

In the above equations, the b parameters determine the barrier and rate at which the rearrangement occurs. The $G_{CH4}(R_7,R_3)$ term has the form similar to $G_{CC}(R_1,R_3)$ as described in Eqs. 2.71–2.74. The corresponding parameters are denoted via 'ch' subscript instead of 'cc'.

Table 2.22

Parameters for the Channel VI Potetnial

Parameter	Value	Parameter	Value
ϵ_v^{cc}	6.3250 eV	θ_v^o	2.101 376 4 rad
ϵ_a^{cc}	7.9482 eV	θ_a^o	3.141 592 7 rad
ϵ_v^{ch}	4.6190 eV	κ_v^o	0.000 eV
ϵ_a^{ch}	4.8000 eV	κ_a^o	1.720 eV
ω_v^{cc}	2.289 Å^{-1}	V_a^o	6.670 eV
ω_a^{cc}	2.397 Å^{-1}	b_1	1.800 Å^{-2}
ω_v^{ch}	1.375 Å^{-1}	b_2	1.088 Å
ω_a^{ch}	2.070 Å^{-1}	b_3	15.000 Å^{-2}
σ_v^{cc}	1.307 Å	b_4	1.062 Å
σ_a^{cc}	1.203 Å	b_5	2.200 Å^{-2}
σ_v^{ch}	1.088 Å	b_6	1.088 Å
σ_a^{ch}	1.061 Å		

The $G_{CCH4}(\theta_5,R_3)$ and $G_{CCH4}(\theta_7,R_3)$ represent the bending interactions, which have the same functional form given by Eqs. 2.40-2.42. The corresponding bending parameters are

$$k_{CCH5} = k_v^o + (k_a^o - k_v^o)S_{13}(R_3), \quad (2.85)$$

$$\theta_{CCH5} = \theta_v^o + (\theta_a^o - \theta_v^o)S_{13}(R_3), \quad (2.86)$$

$$k_7^o = k_a^o S_{15}(R_3), \quad (2.87)$$

$$\text{and } \theta_7^o = \theta_a^o S_{15}(R_3). \quad (2.88)$$

$G(\Phi)$ is the dihedral interaction term which is given by

$$G(\Phi) = V_a^o \sin^3\theta_5 \sin^3\theta_7 \sin^2\Phi \quad (2.89)$$

The values of channel VI parameters are given in the above Table 2.22.

The reaction channel VII represents the three-center H_2 elimination from vinyl bromide. The potential for this channel is written as a sum H_2 potential (V_{HH}) and C=CHBr potential ($V_{HBrC=C}$) as follows:

$$V_{VII} = V_{HH}(R_9) + V_{HBrC=C}(R_1,R_2,R_4,R_{11},R_{12}) \quad (2.90)$$

The $V_{HH}(R_9)$ term is a simple Morse potential for H_2 and the $V_{HBrC=C}(R_1,R_2,R_4,R_{11},R_{12})$ potential is fitted to the *ab initio* data described in the previous section. The functional form of $V_{HBrC=C}$ is

$$V_{HBrC=C}(R_1,R_2,R_4,R_{11},R_{12}) = T_{CC}(R_1) + T_{CH3}(R_2) + T_{CBr}(R_{12})$$

$$+ T_{CCH3}(\theta_4) + T_{CCBr}(\theta_2) + T(\Phi) \quad (2.91)$$

where $T_{CC}(R_1)$, $T_{CH3}(R_2)$ and $T_{CBr}(R_{12})$ are Morse potentials whose well depths, curvatures and equilibrium distances are denoted by δ,κ and ρ respectively. The bending potential is written in the same way as vinyl bromide, where the bending force constants are written λ_{CCH} and λ_{CCBr} respectively. The equilibrium angles are taken to be 120.0° in both cases. $T(\Phi)$ has the same functional form as $G(\Phi)$ with the magnitude parameter

being defined by χ. The values of all the parameters for the channel VII are given in Table 2.23.

Table 2.23
Parameters for the Channel VII potential

Parameter	Value	Parameter	Value
δ_{CC}	5.7716 eV	ρ_{CC}	1.310 Å
δ_{CH}	4.6190 eV	ρ_{CH}	1.088 Å
δ_{CBr}	3.3390 eV	ρ_{CBr}	1.800 Å
κ_{CC}	2.289 $Å^{-1}$	λ_{CCH}	1.400 eV/rad^2
κ_{CH}	1.975 $Å^{-1}$	λ_{CCBr}	3.600 eV/rad^2
κ_{CBr}	1.720 $Å^{-1}$	χ	6.670 eV

Once the analytical surface is developed, the vibrational frequencies (see Table 2.11) can be calculated at the equilibrium geometry. The vibrational frequencies are directly proportional to the curvatures at that point. Most of the vibrational frequencies from the above surface are higher than the experimental frequencies. This type of error is generally seen in *ab initio* calculations which predict the vibrational frequencies that are too high by 10% or less. Therefore, we need to modify the above potential, so that we obtain frequencies in better agreement with the experimental frequencies. From this point onward, we will denote the above global potential as **PES1** whose frequencies are off from the IR and Raman experiments. The modified potential which reproduces the vibrational frequencies close to experiment will be denoted as **PES2.**

The new global potential energy-surface, PES2, is developed by modifying the above potential energy-surface (PES1). We keep the functional form of PES2 same as that of PES1. Values of parameters those change the curvatures at the equilibrium geometry are varied to obtain a good agreement to the experimental frequencies. The

parameters that define PES2 are given in Table 2.14. Examination of Table 2.14 for PES2 parameters shows that the values of the α parameters of the Morse potentials, force constants (k) for bending potentials and V_i^o for the dihedral potentials are changed from the PES1 parameters. Also the λ^k, μ^k parameters are changed to ensure that the surface remains smooth and goes to zero when the bonds are stretched to a large distance from the equilibrium values (see Table 2.3). As the parameters are varied to obtain PES2, additional calculations are conducted to ensure that PES2 has same potential barriers for all the reaction channels as PES1.

The switching functions in Eq. 2.1 connect different reaction channels smoothly. By varying the values of the switching function parameters, one can change the topology of the global potential energy-surface. These parameters determine the barrier for different reaction channels. They also define the transition-state geometry and its frequencies. In this study, no effort has been made to fit the transition-state geometries and frequencies to the *ab initio* results. However, we can change the values of the switching function parameters to study how the transition-state geometries and frequencies, affect the reaction dynamics of vinyl bromide.

It is worth while to mention here that in PES2, we have added another angular term for <HCH angle to the PES1 to fit the low frequencies vibration in better agreement than that of PES1. For the angle <HCH, we have used the two switching functions for two C-H bonds whose functional form is similar to Eq 2.42. In Figure 2.17, the plot of the angle bending motion is shown.

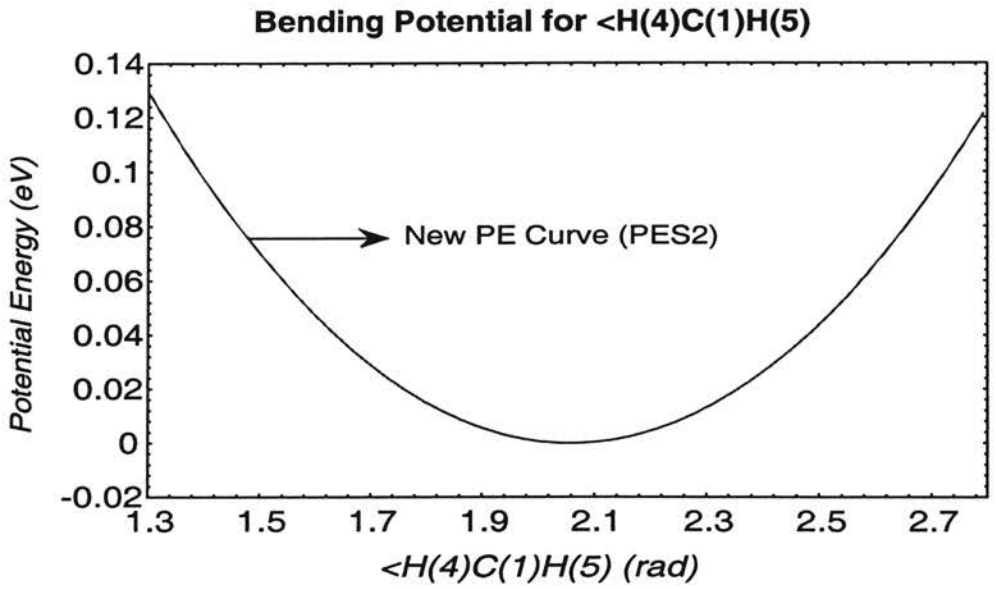

Figure 2.17 Bending potential for the angle <HCH

To construct PES3, we have systematically varied the values of the parameters of PES2. Every time we change the values of switching function parameters, the barrier heights change. To study the sensitivities of the dissociation dynamics to the transition-state geometry and frequency, we ensure that the barrier heights for different channels remain unchanged. This has been done in an iterative way after changing each parameter. We develop a different surface whose functional form is same as that of PES2. However, it has a different set of values of switching function parameters. This potential will be denoted as PES3. The values of these sets of switching parameters are given in Table 2.3.

C. Properties of Analytical surfaces

The minimum-energy structures for the reactants and products in each of the reaction channels for the global PES are located using a damped trajectory method[10]. In this method, the atoms are initially placed in a configuration near to the local minimum being sought. The kinetic energy of each atom is set to zero and Hamiltonian equations of motions for the system are numerically integrated until the total kinetic energy of the system attains a maximum value. At this point, the integration is stopped and the momentum components of all atoms are once again set to zero. This procedure is repeated until the system potential energy converges to a local minimum. We have continued the iterations until the system potential converges to eight significant digits.

The equilibrium energies obtained from global potential energy-surfaces are given in the Table 2.24 relative to the separated atoms. Note that for all potential surfaces, the equilibrium energies remain the same because we do not change the dissociation energies for the bonds. Therefore, in the Table 2.24 only the equilibrium energies for any one of the three PESs are reported. The calculated ΔE values for various reaction channels are listed in Table 2.25 and compared to the experimental and theoretical results. The results obtained from the analytical PES are in good agreement with the experimental and theoretical results. The corresponding equilibrium geometries obtained from global PES are given in Table 2.26 and compared to the experimental results.

Table 2.24

Equilibrium energies for different reactants and products from the global potential-energy surface (Zero-point energies not included)

Molecule	Total potential (eV)
H_2C=CHBr	-22.9275 (PES2)
H_2C=CH	-19.8189
HC≡CH	-17.5473
HBR	-3.9180
HC≡CBr	-15.8838
H_2C=CBr	-18.0500
H_2C=C	-15.5644
C=CHBr	-13.7296
H_2	-4.7450

Table 2.25

Energies of reactions[a]

	ΔE(eV)		
	Global potential		
Reaction	PES1	expt/theory	ref
$C_2H_3Br \rightarrow C_2H_3 + Br$	2.973	3.101, 3.161	19, 3
$C_2H_3Br \rightarrow H_2C$=C + HBr	3.012	2.923	20
$C_2H_3Br \rightarrow$ C=CHBr + H_2	3.910	3.990	3
H_2C=C → HC≡CH	-1.982	-1.990	16

The fundamental harmonic vibrational frequencies obtained from a normal mode analysis on the different global PESs are given in the Table 2.27. In case of PES1, most of the frequencies are too large and for PES2 and PES3 the frequencies are fitted to the experimental frequencies as close as possible.

Table 2.26

Comparison of equilibrium geometry obtained from different potential-energy surfaces and experiments.[a]

Variable	PES1	PES2	PES3	Experiment
$C_1=C_2$	1.3225506 Å	1.2928337 Å	1.2928337 Å	1.330 Å
$C_2 - H_3$	1.0706042 Å	1.0684310 Å	1.0684403 Å	1.077 Å
$C_2 - Br$	1.8942693 Å	1.8989525 Å	1.8989594 Å	1.890 Å
$C_1 - H_4$	1.0779619 Å	1.0771227 Å	1.0771096 Å	1.083 Å
$C_1 - H_5$	1.0710218 Å	1.0685600 Å	1.0685557 Å	1.085 Å
$C_1C_2H_3$	123.5908941°	123.5897296°	123.5896952°	124.2°
C_1C_2Br	123.7589036°	123.7588861°	123.7588910°	122.5°
$C_2C_1H_4$	119.5196851°	119.5397462°	119.5397436°	118.7°
$C_2C_1H_5$	122.2690615°	122.2874206°	122.2874213°	121.3°
BrC_2H_3	112.6502023°	112.6513844°	112.6514138°	113.3°
$H_4C_1H_5$	118.2112535°	118.1728331°	118.1728351°	120.0°
$H_4C_1C_2H_3$	0.000°	0.000°	0.000°	0.000°
$H_5C_1C_2H_3$	180.0°	180.0°	180.0°	180.0°
$H_4C_1C_2Br$	180.0°	180.0°	180.0°	180.0°
$H_5C_1C_2Br$	0.000°	0.000°	0.000°	0.000°

[a] Subscript on each atom indicates the atom number in Fig. 2.1

Table 2.27

Comparisons of fundamental vibrational frequencies for vinyl bromide obtained from different surfaces.

	Frequency (cm^{-1})			
Mode #	PES1	PES2	PES3	Exp.
12	3520	3135	3136	3113
11	3478	3087	3085	3086
10	3386	3015	3008	3027
9	1765	1603	1603	1604
8	1375	1396	1396	1373
7	1142	1231	1231	1256
6	1130	1022	1022	1006
5	1053	953	953	942
4	986	902	902	902
3	593	603	603	613
2	581	570	571	583
1	335	340	340	344

The potential barrier for the various reaction channels are obtained from the analytic surfaces using a combination of grid search and constrained, damped trajectory methods[18]. For HBr elimination, a two-dimensional search over C–Br and C–H distances is executed. Similarly for H_2 elimination, a two-dimensional grid search is executed over the two dissociating C–H bonds. At each node in the grid, a sequence of constrained, damped trajectory cycles[18] are executed in which the virtual forces required to hold the two bond distances of the grid fixed are incorporated. These damped trajectory cycles permit all atoms to relax to the most stable configuration associated with each grid point. The saddle points are determined by iteration to the point at which all first derivatives of the potential are zero to the three or more significant digits and normal mode analysis yields exactly one imaginary frequency.

The potential for the Br atom dissociation from the ground state of vinyl bromide rise monotonically for all the three surfaces. A similar result is obtained in the *ab initio* calculations[3] which fail to locate a saddle point for the dissociation.

The reaction profile for three-center HBr elimination obtained from all three surfaces rises monotonically to the product state. In Figure 2.18, we have plotted the reaction profile for three-center HBr elimination for all three surfaces. There is no back reaction barrier in any case. We have tabulated the potential barrier for three different surfaces in Table 2.28. Note that the reaction coordinate curvature, C, decreases in the order $C_{PES1} > C_{PES2} > C_{PES3}$.

The reaction profile three-center H_2 elimination is qualitatively similar to that for three-center HBr elimination. There is no back reaction barrier and the barrier rises monotonically to the product state. The barrier for three-center H_2 elimination on three

different surfaces is given in Table 2.28. The reaction profiles for three-center H_2 elimination on three different surfaces are plotted in Fig 2.19.

Table 2.28
Calculated potential barriers for different reaction channels.

Reaction	Potential barriers (eV)			
	PES1	PES2	PES3	*ab initio* theory / expt.
$C_2H_3Br \rightarrow C_2H_3 + Br$	3.109	3.109	3.109	3.101
$C_2H_3Br \rightarrow H_2C{=}C + HBr$	3.456	3.457	3.456	3.196
$H_2C{=}C \rightarrow HC{\equiv}CH$	0.017	0.017	0.017	<0.088
$C_2H_3Br \rightarrow C{=}CHBr + H_2$	4.459	4.459	4.459	4.618

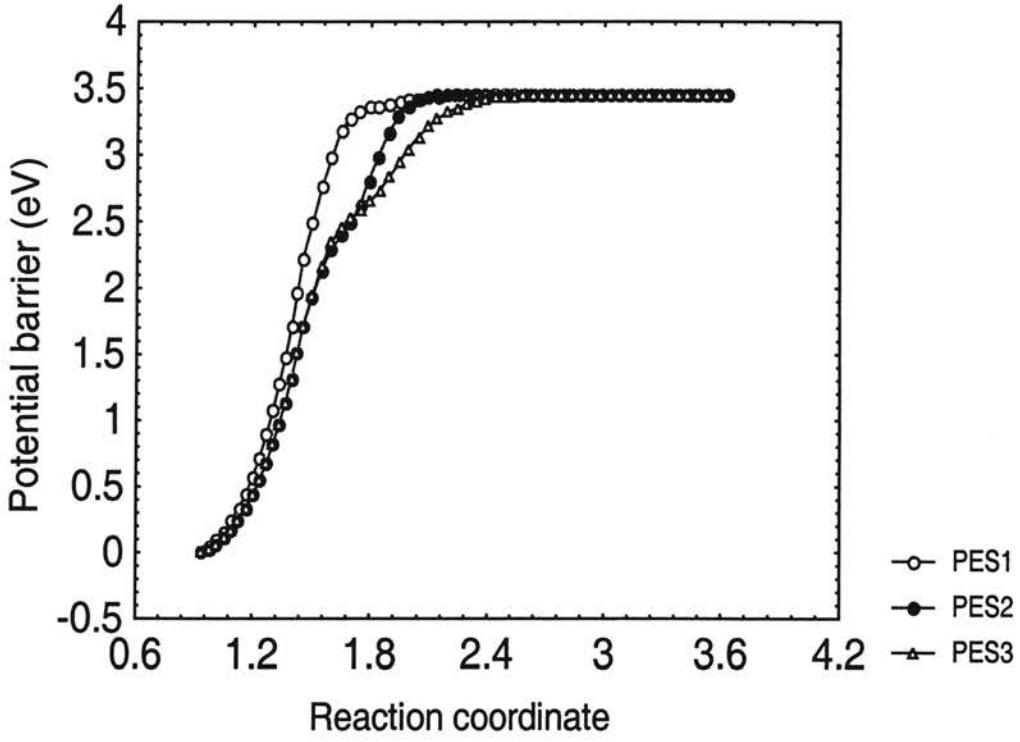

Figure 2.18

The plot of potential barrier vs. reaction coordinate for three-center HBr elimination where reaction coordinate is taken as the distance between C atom number 2 and the middle point of HBr.

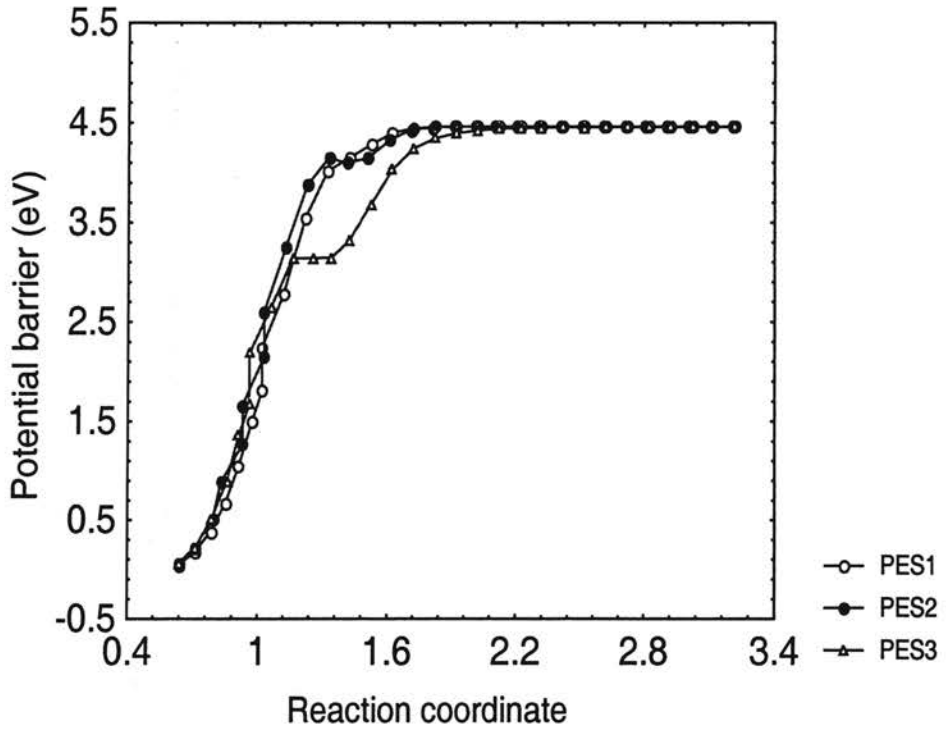

Figure 2.18

The plot of potential barrier vs. reaction coordinate for three-center H_2 elimination where reaction coordinate is taken as the distance between C atom number 1 and the middle point of H_2.

REFERENCES

1. M. J. Frisch, G. W. Trucks, H. B. Schlegel, P. M. W. Gill, B. G. Johnson, M. A. Robb, J. R. Cheeseman, T. Keith, G. A. Petersson, J. A. Montgomery, K. Raghavachari, M. A. Al-Laham, V. G. Zakrzewski, J. V. Ortiz, J. B. Foresman, J. Cioslowski, B. B. Stefanov, A. Nanayakkara, M. Challacombe, C. Y. Peng, P. Y. Ayala, W. Chen, M. W. Wong, J. L. Andres, E. S. Replogle, R. Gomperts, R. L. Martin, D. J. Fox, J. S. Binkley, D. J. Defrees, J. Baker, J. P. Stewart, M. Head-Gordon, C. Gonzalez, and J. A. Pople, *Gaussian* 94, Revision E.2; Gaussian, Inc., Pittsburgh PA, 1995.

2. S. Huzinaga, J. Andzelm, M. Klobukowski, E. Radzio-Andzelm, Y. Sakai and H. Tatewaki, *Gaussian Basis Sets for Molecular Calculations,* Elsevier, Amsterdam, 1984.

3. S. A. Abrash, R. W. Zehner, G. J. Mains and L. M. Raff, *J. Phys. Chem.* **99**, 2959 (1995).

4. P. M. Agrawal, D. L. Thompson, L. M. Raff, *J. Chem. Phys.* **89**, 741 (1988).

5. R. Viswanathan, D. L. Thompson, L. M. Raff, *J. Chem. Phys.* **79**, 2857 (1983).

6. P. M. Agrawal, D. L. Thompson, L. M. Raff, *J. Chem. Phys.* **92**, 1069 (1990).

7. L. M. Raff, *J. Phys. Chem.* **91**, 3266 (1987).

8. L. M. Raff, *J. Phys. Chem.* **92**, 141 (1988).

9. L. M. Raff and R. W. Graham, *J. Phys. Chem.* **92**, 5111 (1988).

10. L. M. Raff, *J. Chem. Phys.* **90**, 6313 (1989).

11. L. M. Raff, *J. Chem. Phys.* **93**, 3160 (1990).

12. L. M. Raff, *J. Chem. Phys.* **95**, 8901 (1991).

13. L. M. Raff, *J. Chem. Phys.* **97**, 7459 (1992).

14. T. D. Sewell, W. H. Scharnz, D. L. Thompson and L. M. Raff, *J. Chem. Phys.* **95**, 8089 (1991).

15. M. P. Sudhakaran and L. M. Raff, *Chem. Phys.* **95**, 165 (1985)

16. R. Krishnan, M. J. Frisch, J. A. Pople and P. v. R. Schleyer, *Chem. Phys.* **79**, 408 (1981)

17. (a) Y. Osamura, H. F. III. Schaefer, S. K. Gray and W. H. Miller, *J. Am. Chem. Soc.* **103**, 1904 (1981). (b) B. J. Smith, R. Smernik and L. Radom, *Chem. Phys. Lett.* **188**, 589 (1992). (c) Ph. Halvick, D. Liotard and J. C. Rayez, *Chem. Phys.* **177**, 69 (1993)

18. L. M. Raff and D. L. Thompson, The Classical trajectory Approach to Reactive Scattering. In *Theory of Chemical Reaction Dynamics*; M. Baer, Ed.CRC Press: Boca Raton, FL,Vol III, 1 (1985).

19. (a) A. M. Wodtke, E. J. Hintsa, J. Somorjai, Y. T. Lee, *Isr. J. Chem.* **29**, 383 (1989).
(b) A. M. Wodtke, Y. T. Lee, *J. Phys. Chem.* **89**, 4744 (1985).

20. H. Okabe, *J. Chem. Phys.* **62**, 2782 (1975).

CHAPTER III

STUDIES OF GAS-PHASE GROUND-STATE DISSOCIATION DYNAMICS OF VINYL BROMIDE ON THREE DIFFERENT POTENTIAL-ENERGY SURFACES

A. Methods and Procedures:

The dissociation dynamics of vinyl bromide on three different potential-energy surfaces have been investigated at several internal energies in the range of 4.5–6.44 eV, in excess of zero-point energy using classical trajectory methods[1].

The initial states for the trajectories are prepared by first inserting zero-point energy into the vinyl bromide normal modes using projection methods[2-4](detailed discussion of these methods are given in chapter IV). For a given potential-energy surface, Hamilton's equations of motion determine the dynamics of the system. For a system of N atoms, Hamilton's equations are,

$$\frac{\partial H(p,q)}{\partial p_i} = \dot{q}_i \qquad \text{(for i = 1, 2, ...3N)} \tag{3.1}$$

$$\frac{\partial H(p,q)}{\partial q_i} = -\dot{p}_i \qquad \text{(for i = 1, 2, ...3N)} \tag{3.2}$$

where H(p,q) is the Hamiltonian of the system, and q and p are the set of 6N generalized coordinates and momenta respectively. In the general case, there are 6N-coupled

differential equations of motion that must be integrated for a period of time that is sufficiently long to permit investigation of the important features of the dynamics. Depending on the time period and increment, the calculation can be computationally intensive.

After inserting the zero-point energy into the normal modes, Hamilton's equations of motion are integrated for a randomly chosen time period t_p given by

$$t_p = \xi\tau, \tag{3.3}$$

where ξ is a random number chosen from a distribution that is uniform on the interval [0,1] and τ is the characteristic period of the lowest frequency vibrational mode in vinyl bromide. This procedure serves to randomize the vibrational phase angles for each trajectory. The numerical integrations are carried out using a forth-order Runge-Kutta procedure with a fixed step size of 2.038×10^{-16} s. Subsequent to the above integration, the desired excitation energy E is inserted into vinyl bromide using projection techniques.[2-4] In all calculations, E is randomly partitioned among the twelve available vibrational modes with the initial rotational energy set to zero.

With the above initial states, trajectories are integrated until reaction occurs or until an upper limit of time t_{max} is exceeded. Final states are determined using a combinations of distance and energy criteria.

The total unimolecular dissociation rate-coefficient at each energy, k(E), is obtained by fitting the decay curve to a first-order rate expression. In making these decay plots, the zero of time is taken to be the time required for the first reaction to occur.

B. Results.

a) Total Vinyl Bromide Decomposition Rates.

We have calculated the total decomposition rates of vinyl bromide on the three potential-energy surfaces, PES1, PES2 and PES3, that have been described in detail in Chapter II. We find that a first-order rate law accurately describes the total decomposition rates with excitation energy E initially distributed randomly over twelve vibrational modes of the molecules. Typical decay plots are shown in Figures 3.1a–3.1c on three potential-energy surfaces at different excitation energies. These plots are obtained from the results of 400 trajectories with t_{max} = 250 t.u. (1 t.u. = 0.01019 ps). The lines in the decay plots are the least-square fit to the data. The negative slopes of these lines yield the total decomposition rates. The total decomposition rate coefficients on three PESs at different excitation energies are tabulated in the Table 3.1 along with their average values. The average values are calculated for the comparison of rate coefficients obtained from different potential-energy surfaces with different topological features to understand the effects of various topological features on the total decomposition rate. We have also presented the results obtained from previous calculations on an empirical potential-energy surface (EPS) by Abrash *et al*[6]. The probable errors in the slopes are given inside parenthesis and calculated using the following equation[5];

$$P_b = r_e\sqrt{\frac{n}{D}} \qquad (3.4)$$

where r_e is defined as

$$r_e = 0.6745\sqrt{\frac{\sum (y_i - y_i(\text{calc.}))^2}{(n-2)}} \qquad (3.5)$$

and

$$D = n\sum x_i^2 - (\sum x_i)^2 \qquad (3.6)$$

n is the total number of data points which is fitted with a equation of line.

Table 3.1

Comparisons of the total decomposition rate coefficients of vinyl bromide at different energies on three potential-energy surfaces with their mean values and the same reported by Abrash *et al*[6] are given as EPS. In the parenthesis the error limits are given which are calculated using equation 3.4.

Energy	Rate coefficient (ps^{-1})				
(eV)	PES1	PES2	PES3	Average	EPS
4.50	0.932(±9.87E-5)	0.893(±6.31E-5)	0.736(±4.80E-5)	0.854	0.350
5.00	1.492(±2.21E-4)	1.551(±1.43E-4)	1.354(±1.80E-4)	1.466	0.540
5.50	2.061(±3.41E-4)	3.013(±2.98E-4)	2.208(±3.41E-4)	2.427	1.040
6.00	2.709(±6.42E-4)	3.984(±8.42E-4)	3.445(±6.62E-4)	3.379	1.490
6.44	4.553(±7.58E-4)	4.652(±1.15E-3)	4.995(±5.81E-4)	4.733	2.110

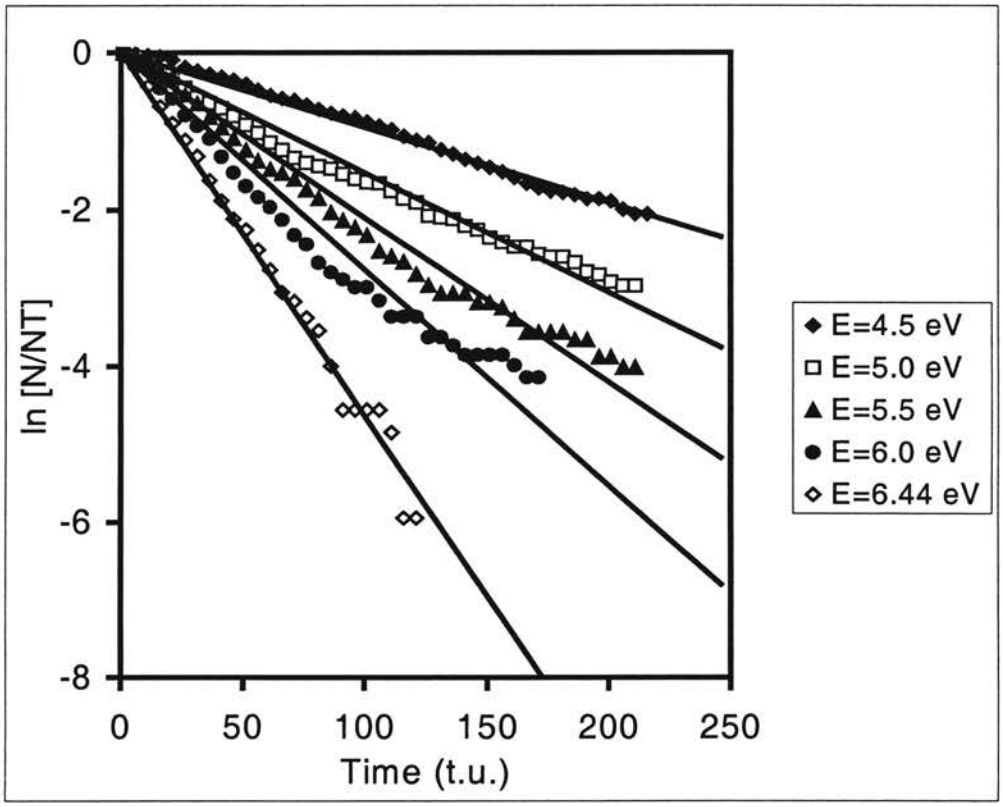

Figure 3.1a

Logarithmic plots of ln[N/NT] versus time at different excitation energies for 400 trajectories on PES1 where N is the number of unreacted trajectories and NT is the total number of trajectories. Lines in the above plot are the linear fit to the data points. The slopes of lines yield rate coefficients. Time is given in molecular time units where 1 t.u. = 0.01019 ps.

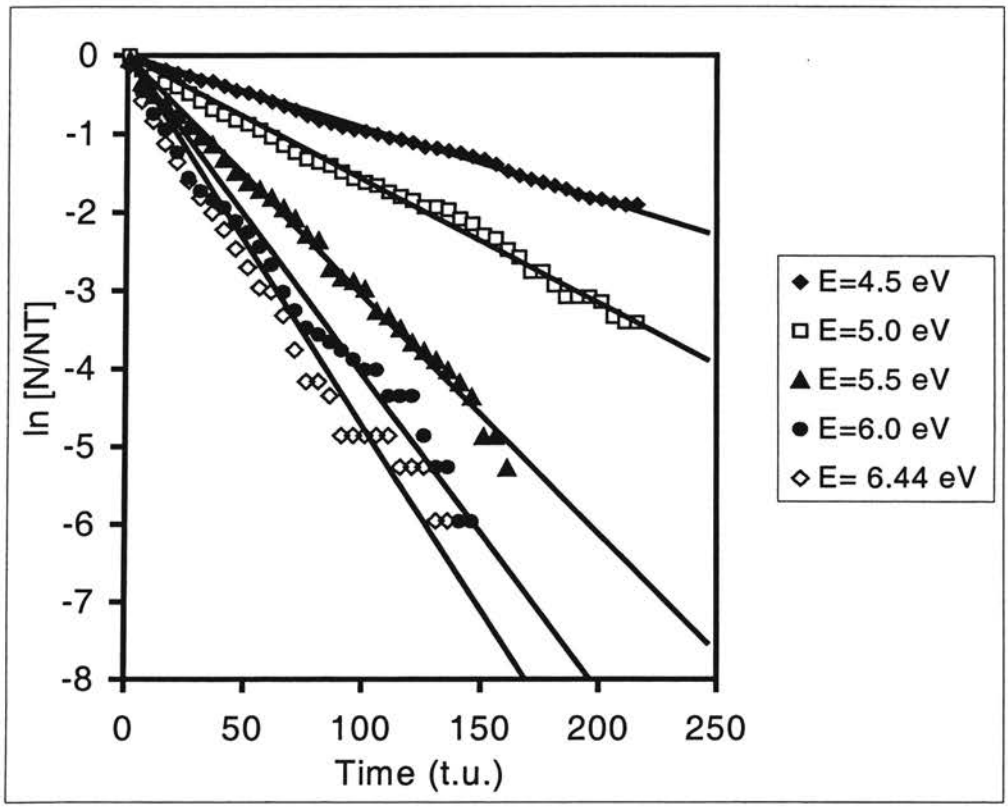

Figure 3.1b

Logarithmic plots of ln[N/NT] versus time at different excitation energies for 400 trajectories on PES2 where N is the number of unreacted trajectories and NT is the total number of trajectories. Lines in the above plot are the linear fit to the data points. The slopes of lines yield rate coefficients. Time is given in molecular time units where 1 t.u. = 0.01019 ps.

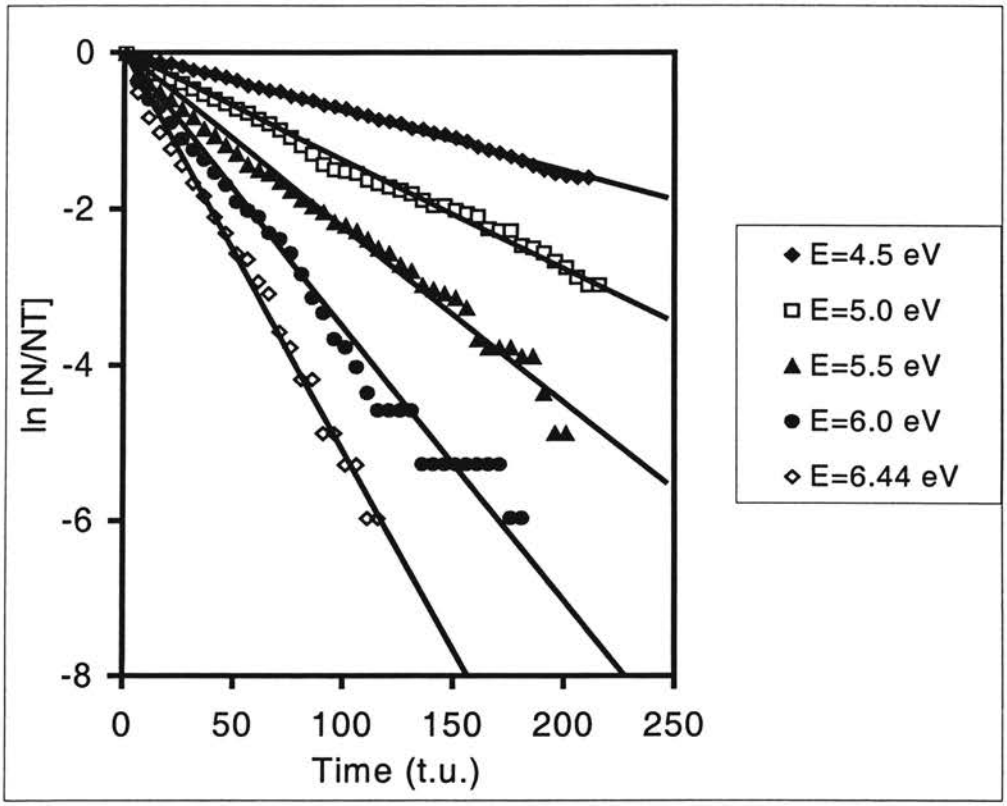

Figure 3.1c

Logarithmic plots of ln[N/NT] versus time at different excitation energies for 400 trajectories on PES3 where N is the number of unreacted trajectories and NT is the total number of trajectories. Lines in the above plot are the linear fit to the data points. The slopes of lines yield rate coefficients. Time is given in molecular time units where 1 t.u. = 0.01019 ps.

It is evident that slopes of these fitted lines increase with increase in excitation energy on a particular PES. Figure 3.2 shows the variations of k(E) with energy on three PESs. Lines connecting the points are drawn for visual clarity.

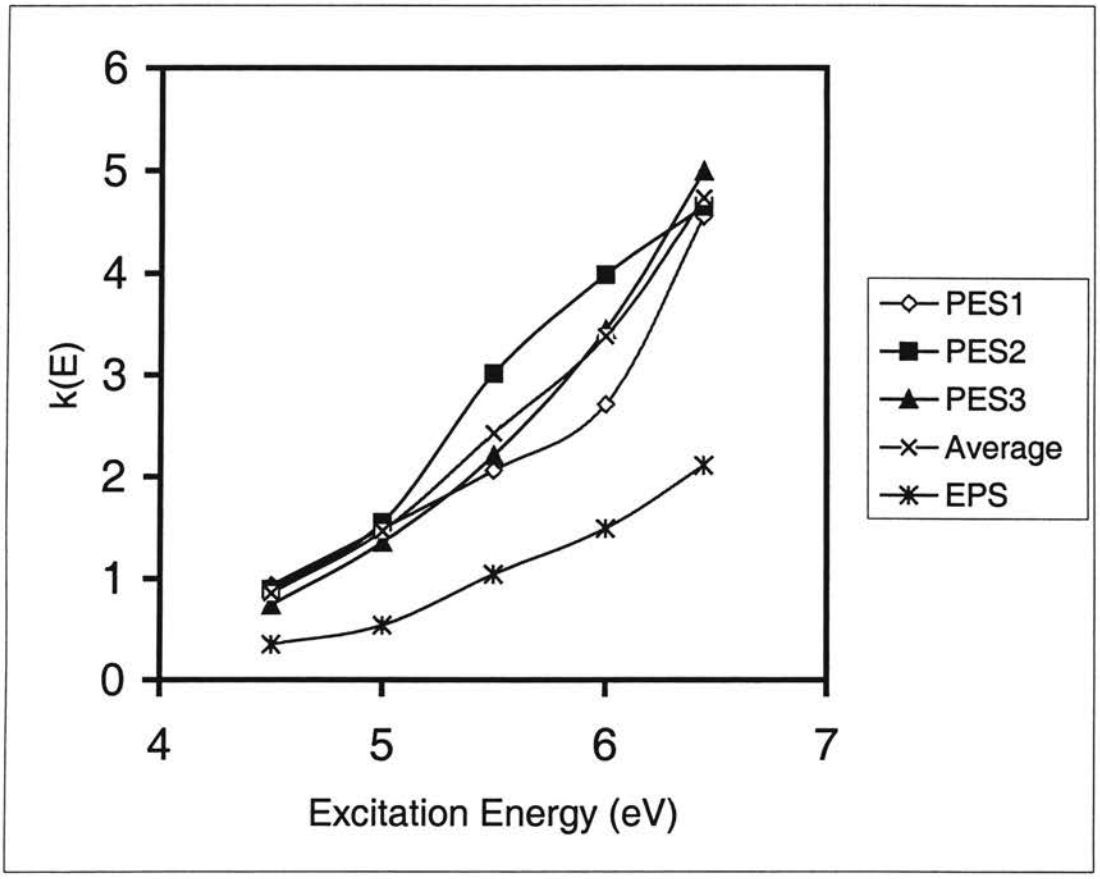

Figure 3.2

Plot of k(E) (ps^{-1}) vs excitation energy (eV) for 400 trajectories on three different potential-energy surfaces. The average values of k(E) at a particular excitation energy is also plotted along with the k(E) obtained from the calculation by Abrash *et al.*[6] on EPS. The computed points are connected with straight lines to enhance the visual clarity of the plots.

A closer look to the Table 3.1, Figures 3.1a–c and 3.2 indicates that the decomposition rate almost doubles when the excitation energy changes from 6.0 eV to 6.44 eV for PES1. It is worthwhile to mention at this point that we have developed the PES1 by fitting the results from *ab initio* calculations. In PES1 the vibrational frequencies are overestimated compared to the experimental values. We have fitted the results obtained from *ab initio* calculations which indicates the proper variations of potential energy with respect to the bond stretching, angle bending and dihedral-angle torsion. In case of PES2 we have changed the curvatures of the PES with respect to each bond stretching, angle bending and torsional terms, so that we get a good agreement between the calculated and experimental vibrational frequencies. While the vibrational frequencies are fitted to the experimental values as close as possible, the dissociation energy for each bond and the equilibrium geometry is kept unaltered. The parameters of switching functions are readjusted to keep the energy barrier for all the reaction channels under this investigation almost the same. When we compare the results obtained from PES1 and PES2 then we can find out the effects of curvatures of the PES and slopes of the potential barrier on the total decomposition rates.

For PES2, the rate coefficient almost doubles when the excitation energy changes from 4.5 eV to 5.0 eV and from 5.5 eV to 6.0 eV. The comparisons of the rate coefficients obtained from PES1 and PES2 indicate that initially, at 4.5 eV decomposition rate of vinyl bromide on PES1 is slightly more than that PES2. The decomposition rate on PES2 becomes higher than that on PES1 above 5.0 eV of excitation energy. Because the PES2 has less steep slope of reaction barrier than that of PES1.

We have taken the PES2 and modified it with new switching function whose functional forms are different from the PES1 and PES2. Then parameters of the switching functions are adjusted to keep the barrier almost the same for all the reaction channels under present investigation. This will enable us to investigate the effects of switching functions and the curvature of the reaction path on the dynamics of dissociation.

Results in Table 3.1 indicate that the rate coefficients obtained from PES3 almost double for the excitation energy change from 4.5 to 5.0 eV and 5.5 to 6.0 eV. Similar trends have been observed for PES2. However, the crossover of values of rate coefficient curves for PES2 and PES3 occur at an energy between 6.0 eV to 6.44 eV. Although PES3 has a less steeper slope of reaction barrier than that of PES2, the rate coefficients obtained from PES2 are higher than those obtained from PES3 for all the energy except for 6.44 eV where the rate coefficient becomes higher than that obtained from PES2 and PES1. At excitation energy of 6.44 eV, the results can consistently be explained in terms of the slope of the reaction barrier.

Comparisons of the rate coefficients obtained from PES1, PES2 and PES3 with the average values indicate that the decomposition of vinyl bromide on all the above three surfaces vary a little. When compared the rate coefficients obtained from EPS[6] and average values, it is observed that the rate coefficients obtained from EPS are half of the average values at a particular energy. The EPS is developed by Abrash *et al*[6] empirically by fitting the available *ab initio* and spectroscopic data. To date there is no experimental results available to compare the total decomposition rate of vinyl bromide in gas phase. All of the above facts suggest that it is very important to do the *ab inito* calculations to

obtain how exactly the potential energy varies with stretching of bonds and bending of angle and dihedral angles.

b) Branching Ratios.

Thermal gas-phase decomposition of vinyl bromide exhibits many dissociation channels. All the possible dissociation channels are listed in Table 2.1, in Chapter II. However, to make the model potential-energy surface simple, we have only considered the important dissociation channels such as three-center HBr elimination, three-center H_2 channel, Br atom and H atom channels.

The branching ratios for various reaction channels of vinyl bromide are computed at different energies on three potential-energy surfaces, PES1, PES2 and PES3. These values are give in Tables 3.2 –3.4 and Figures 3.3a – 3.3c. In Tables 3.2 –3.4, error values are given inside the parenthesis. These errors are calculated using the following equation[5]

$$\Delta = \left[\frac{N - N_R}{N N_R} \right]^{1/2} \times 100 \qquad (3.7)$$

where N is the total number of successful trajectories and N_R is the total number of reactive trajectories. Note that if the N_R is large the error (Δ) is less and vice versa.

In the case of PES1, when the excitation energy is 4.5 eV, the major dissociation channel is three-center HBr elimination. Small amounts of Br and H atoms are also observed at this excitation energy. At E = 5.0 eV, besides the above mentioned reaction channels, we begin to observe some three-center H_2 elimination channel. At E = 6.0 eV,

the computed HBr/H_2/Br/H ratios are 85.68/8.22/1.59/3.18. Finally, at E = 6.44 eV the H + Br atom-dissociation channel opens. Figure 3.3a shows a plot of percentage yields versus excitation energy on PES1.

Table 3.2

Computed branching ratios for various reaction channels of vinyl bromide as a function of excitation energy on PES1. Error limits are computed using Eq 3.7.

Excitation	Percentage yield of product				
Energy (eV)	HBr	H_2	Br	H	H+Br
4.50	81.57(±2.39)	0.00	1.26(±44.44)	4.30(±23.73)	0.00
5.00	89.23(±1.76)	0.51(±70.53)	2.56(±31.21)	2.56(±31.21)	0.00
5.50	87.40(±1.92)	4.88(±22.37)	2.57(±31.21)	3.34(±27.76)	0.00
6.00	85.68(±2.11)	8.22 (±17.21)	1.59(±40.49)	3.18(±28.40)	0.00
6.44	85.04(±2.15)	6.82 (±18.93)	2.89(±29.71)	4.72(±23.01)	0.26(±99.74)

Table 3.3

Computed branching ratios for various reaction channels of vinyl bromide as a function of excitation energy on PES2. Error limits are computed using Eq. 3.7.

Excitation	Percentage yield of product				
Energy (eV)	HBr	H_2	Br	H	H+Br
4.50	72.17(±3.15)	0.00	1.84(±37.45)	11.08(±14.38)	0.00
5.00	84.48(±2.16)	0.00	1.78(±37.51)	10.43(±14.78)	0.00
5.50	85.35(±2.10)	1.29(±44.43)	5.14(±21.78)	8.99(±16.12)	0.00
6.00	89.69(±1.72)	1.03(±49.74)	3.87(±25.32)	5.41(±21.22)	0.00
6.44	88.34(±1.85)	0.78(±57.51)	5.70(±20.70)	4.66(±23.01)	0.52(±57.51)

Table 3.4

Computed branching ratios for various reaction channels of vinyl bromide as a function of excitation energy on PES3. Error limits are computed using Eq. 3.7.

Excitation	Percentage yield of product				
Energy (eV)	HBr	H_2	Br	H	H+Br
4.50	72.63(±3.10)	0.51(±70.53)	4.35(±23.72)	2.30(±32.95)	0.00
5.00	85.90(±2.05)	1.03(±49.74)	5.13(±21.78)	2.82(±29.72)	0.00
5.50	89.34(±1.74)	1.52(±40.51)	6.60(±18.95)	1.78(±37.46)	0.00
6.00	91.05(±1.59)	2.56(±31.22)	4.35(±23.72)	2.05(±37.46)	0.00
6.44	86.01(±2.03)	2.54(±31.22)	11.12(±14.21)	0.25(±99.87)	0.00

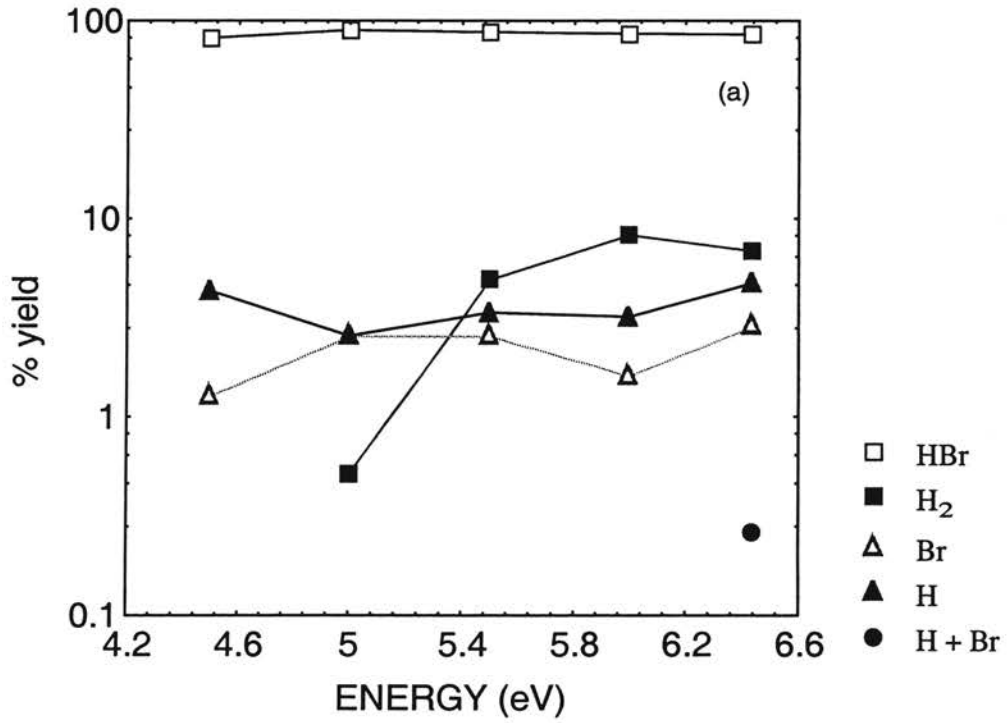

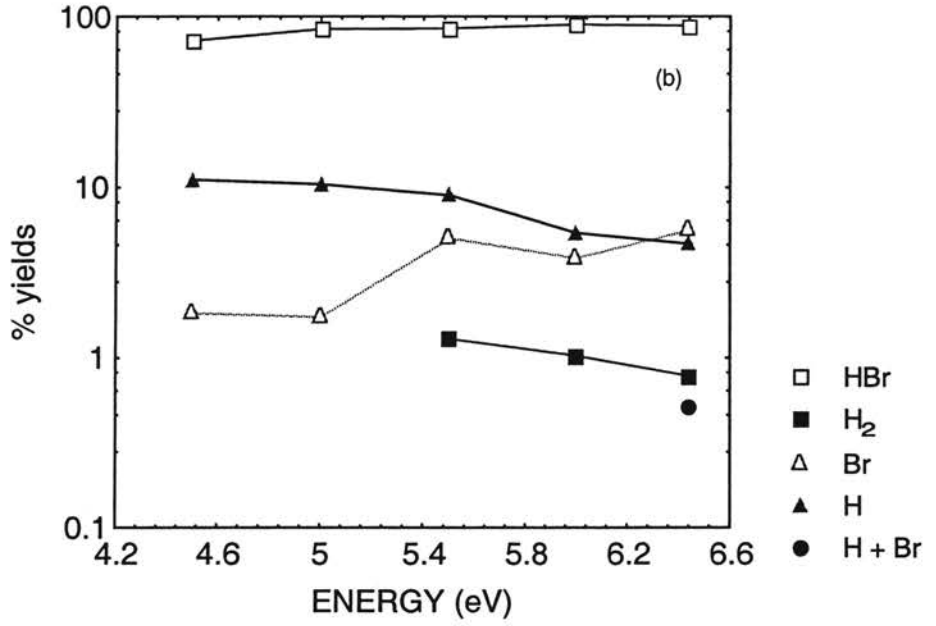

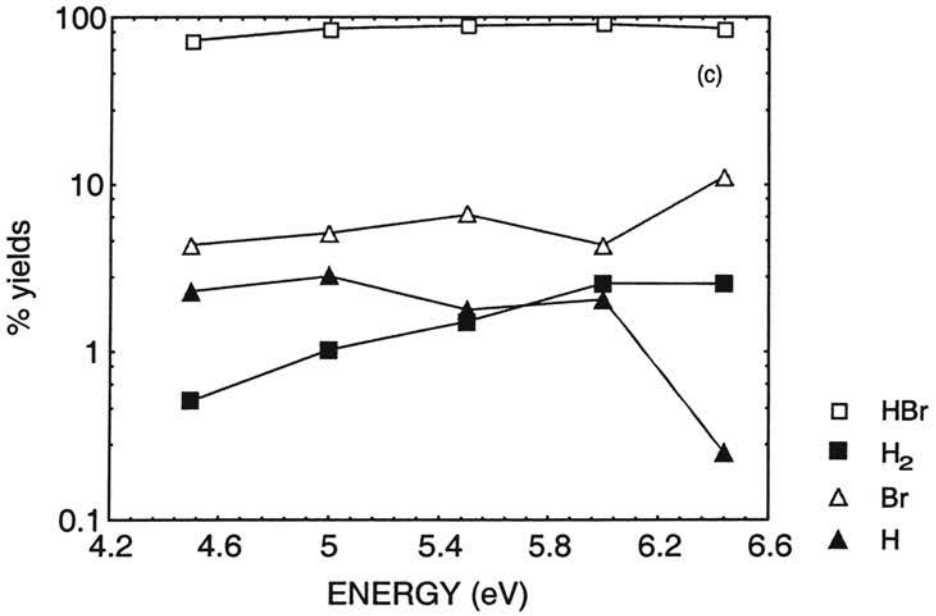

Figures 3.3a-c: The computed branching ratios for various decomposition channels of vinyl bromide as a function of excitation energy on potential-energy surfaces

PES1, PES2 and PES3 respectively. The computed points are connected with straight lines to enhance the visual clarity of the plots.

On potential surface PES2 at E = 4.5 eV, there are three open reaction channels, HBr, Br and H atom dissociation. On this PES, the three-center H_2 elimination channel opens at an excitation energy E = 5.5 eV. At E = 6.0 eV, the computed HBr/H_2/Br/H ratios are 89.69/1.03/3.87/5.41. H + Br atom dissociation is seen only at the highest energy investigated (6.44 eV) as is the case for dissociation on PES1, Figure 3.3b shows the variations of percentage yields versus excitation energy on PES2.

For PES3 at E = 4.5 eV, there are four open channels namely, HBr, H_2, Br and H atom. At E = 6.0, the computed HBr/H_2/Br/H ratios are 91.05/2.56/4.35/2.05. However, no H + Br atom dissociation channel is observed on PES3 even at E = 6.44 eV. Figure 3.3c shows the plot of percentage yields versus excitation energy for PES3.

Comparisons of branching ratios obtained from PES1, PES2 and PES3 indicate that the most important dissociation channel of vinyl bromide in gas phase on all the above PES is the three-center HBr elimination at all the excitation energy from 4.5 eV to 6.44 eV. These results are in qualitative agreement with the shock tube measurements reported by Saito *et al.*[7] who found that, over the temperature range 1300 – 2000 K, vinyl bromide decomposition proceeds solely via molecular elimination of HBr. The results in the Table 3.2 – 3.4 lead the same conclusion. However, the activation energy reported by Saito *et al.*[7] (1.80±0.069 eV) is too low compared to our energy barrier (3.457 eV).

The three-center H_2 elimination occurs at 5.0 eV for PES1 and 5.5 eV for PES2. Furthermore, three-center H_2 elimination is more in PES1 than in PES2. The statistical errors calculated for the percentage yields are small for three-center HBr elimination. But

for other dissociation channels these errors are large (see Table 3.2-3.4). At E = 6.44 eV, H + Br atom dissociation occurs on both PES1 and PES2. At all the energy (4.5 eV to 6.44 eV) we observe Br and H atom dissociation.

Comparisons of the percentage yields on PES2 and PES3 indicate similar trends as that of PES1 and PES2. The major dissociation channel on PES3 is three-center HBr elimination. We observe three-center H_2 elimination, Br and H atom dissociation at all the energy ranging from 4.5 eV to 6.44 eV. However, we observe no H+Br atom dissociation at 6.44 eV as has been observed on PES1 and PES2. Our present simulation results are quite different from those obtained by Abrash *et al.*[6] who observed that at higher energy three-center H_2 elimination channel becomes more important than three-center HBr elimination. Furthermore, they did not observe any H + Br atom dissociation as we have observed on PES1 and PES2 (although the statistical error is huge for this channel).

c) Ground State Dissociation Mechanisms.

The current molecular dynamics studies have been carried out to investigate the effects of different topological features of PES on the ground-state dissociation mechanisms. The dissociation of vinyl bromide in the gas phase occurs almost exclusively by three-center HBr elimination process for all the PES (PES1, PES2, PES3).

At present, none of the experimental studies of vinyl bromide decomposition have determined the principal mechanism of the HBr elimination channel. Such information could be obtained if the experiments were carried out with isotope substituted vinyl

bromide (D_2C=CHBr or H_2C=CDBr). Theoretical investigations by Abrash *et al.*[6] predicted that with D_2C=CHBr, over 99% of the product will be HBr and with H_2C=CDBr, slightly less than 99% yield of DBr due to isotope effects.

From the present classical trajectory simulations on three surfaces (PES1, PES2 and PES3) we observe three different mechanisms for HBr elimination on each surface. The details of three different types of three-center HBr elimination on PES1 are shown in Figures 3.4 a-c. As all the surfaces undergo similar types of dissociation mechanism for three-center HBr elimination, we have presented only the results obtained from PES1 in the Figures 3.4a-c. Figures 3.4a-c show the details of the time variations of the C–Br, H–Br and C–H distances on the –CHBr moiety. Each of these curves is displaced upward by 1 Å for visual clarity except the curve for H–Br. Numerical notation corresponds to the definitions given in Table 2.2. Time is given in molecular time units (1 t.u. = 0.01019 ps).

It is apparent from figure 3.4a that C–H and C–Br bonds break simultaneously to form the H–Br bond. In this case the molecular HBr elimination occurs at $t \approx 57$ t.u. The slow oscillation of C–H distance subsequent to elimination is the result of HBr rotation. Generally such rotation is observed after the reaction as a result of the asymmetric transition state.

A second type of mechanism for three-center HBr elimination can be seen in Figure 3.4b where H atom first dissociates and binds with the Br atom which is still bonded to the C atom. Finally at $t \approx 47$ t.u. C–Br bond dissociates and molecular HBr is formed. The difference in the frequencies of HBr between $t \approx 13$ t.u. to 47 t.u. and $t > 47$ t.u. confirms the above situation. When Br atom is simultaneously bonded to C and H

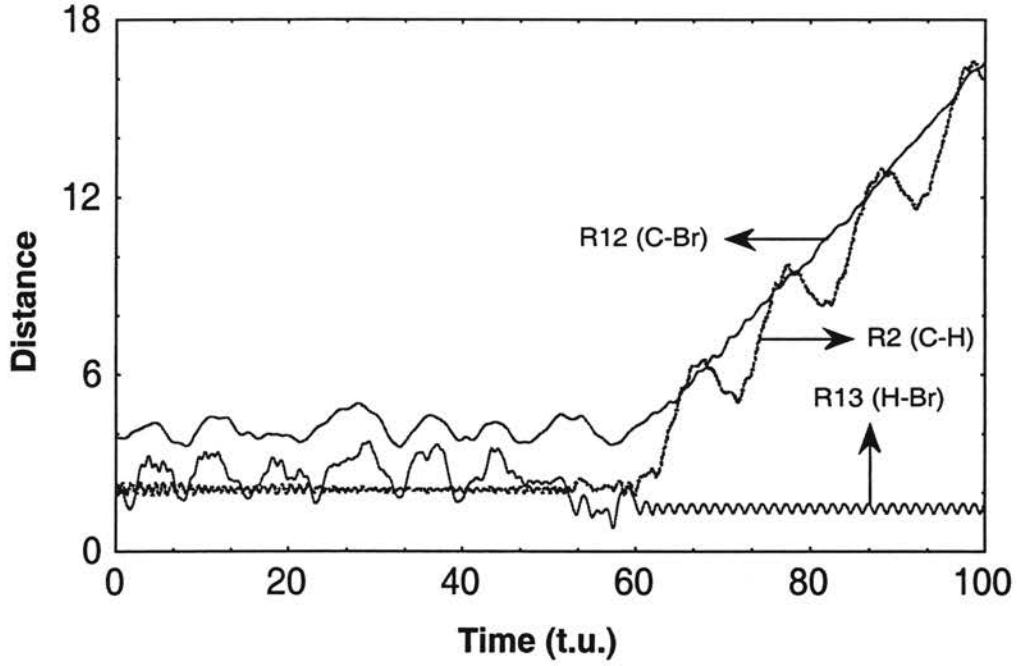

Figure 3.4a

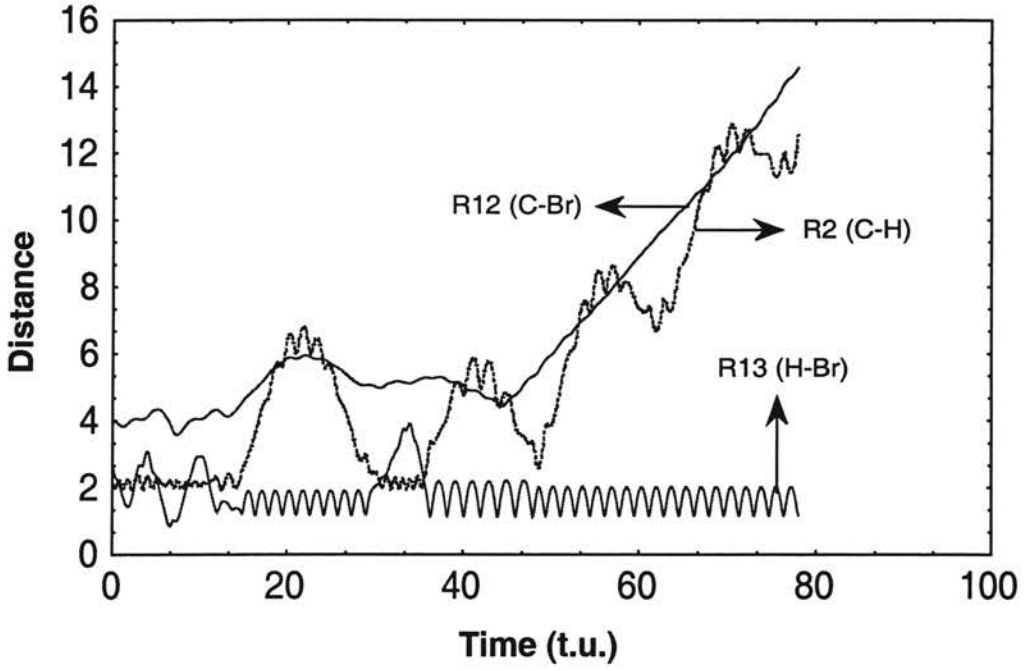

Figure3.4b

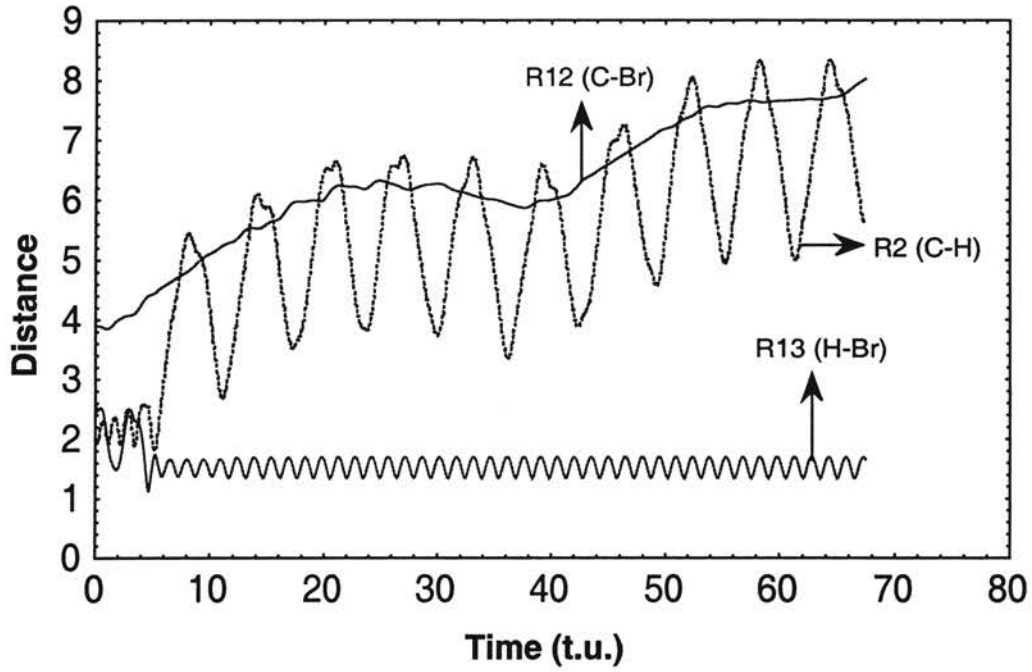

Figure 3.4c

Mechanistic details of three typical three-center HBr elimination from vinyl bromide at an excitation energy 6.44 eV obtain from PES1. The C – H and C – Br bond distances are displayed upward by 1 Å to enhance visual clarity (except H – Br distance). Time is given in units of 0.01019 ps. Distance notation is defined in Table 2.2.

atom, HBr bond will have different vibrational frequency compare to when Br atom is only boned to H atom not the C atom. This type of mechanism is not unusual. This type of mechanism for $C_2H_4F_2$ system where H atom dissociates and bond with the F atom which is still bonded to the C atom is reported in the literature[2,3,8]. We have also observed a slow oscillation of C–H distances which indicates the rotation of molecular HBr subsequent to the dissociation. Between t ≈ 13 t.u. and 47 t.u. the slow oscillations of C–H distance indicate the bending motion of <CBrH angle.

Figure 3.4c represents the third type mechanism for three-center HBr elimination where both the H and Br atoms dissociate and HBr forms a very weakly bonded van der Walls complex with the vinylidene. At t ≈ 10 t.u., this complex dissociates. We also observe the slow oscillations of C–H distance indicating the rotation of molecular HBr after the elimination. In all of the above mechanisms, after the HBr elimination the resulting vinylidene rearranges to acetylene.

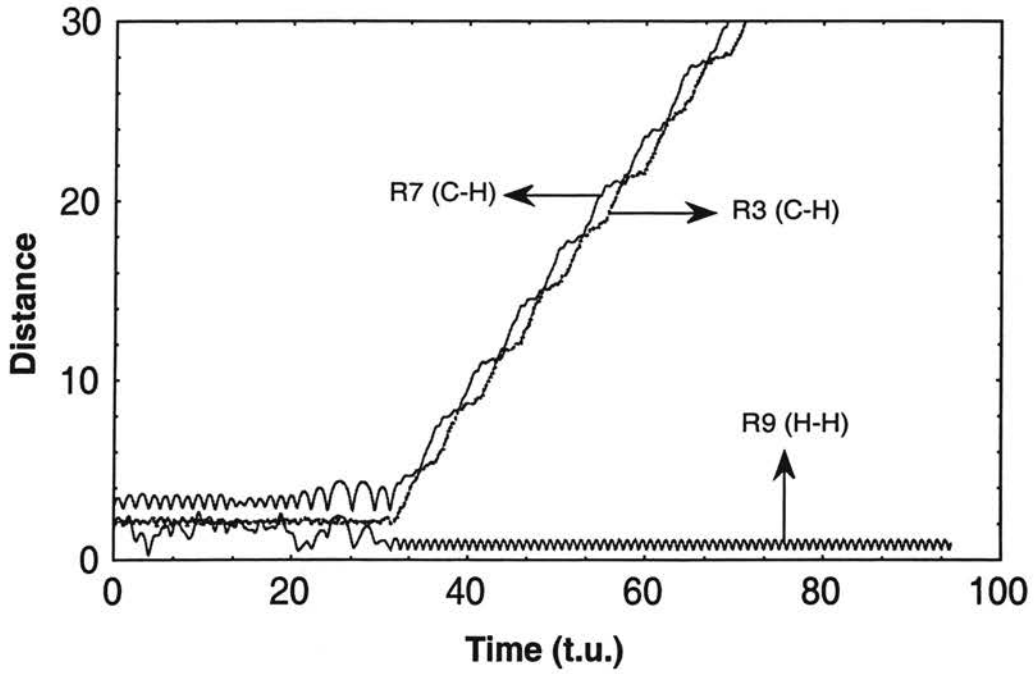

Figure 3.5

Mechanistic details of a typical three-center H_2 elimination for vinyl bromide at an excitation energy of 6.44 eV obtained from PES1. The plot shows the time variations of C – H bonds and H – H distances as a function of time where R3 and R7 are displace upward by 1 Å to enhance visual clarity. Time is given in units of 0.01019 ps. Distance notation is defined in Table 2.2.

The mechanism for three-center H_2 elimination is similar in all the three different surfaces. So we have presented only the results obtained form classical trajectory studies on PES1. Unlike three-center HBr elimination, three-center H_2 elimination occurs via one mechanism. Figure 3.5 shows the time variations of C–H(R3), C–H(R7) and H–H distances. It is clear from the Figure 3.5 that simultaneously both the C–H bonds dissociate and H_2 is formed at $t \approx 35$ t.u.. The resulting C=CHBr rapidly rearranges to bromoacetylene.

Abrash *et al.*[6] have observed only one type mechanism for three-center HBr elimination for EPS (empirical potential-energy surface). In contrast, our current studies indicate three types of mechanism for three-center HBr elimination on all the PES (PES1, PES2 and PES3). Our mechanism for three-center H_2 elimination is similar to that observed by Abrash *et al.*[6]

The above results indicate that mechanisms for the gas-phase dissociation of vinyl bromide on ground state remain the same for all the surfaces with different topological features. However, the difference in the mechanisms observed by Abrash *et al.*[6] and present studies demands the necessity of developing potential-energy surface with accurate variations of potential energy with stretching of bonds, bending of angles and torsion of dihedral angles for polyatomic systems.

d) HBr Vibrational Energy Distribution For Three-center HBr Elimination.

We have also calculated the vibrational energy distribution for the molecular HBr which is produced via three-center HBr elimination from vinyl bromide on all three

PESs under current studies. The center of mass for the whole system remains stationary during the dissociation of vinyl bromide. So the total energy (E_{tot}^{HBr}) for dissociating HBr can be written as

$$E_{internal}^{HBr} = E_{rot}^{HBr} + E_{vib}^{HBr} \tag{3.8}$$

where E_{rot}^{HBr}, E_{vib}^{HBr} are the rotational and vibrational energies of HBr. Eq. 3.8 assumes vibrational and rotational to be separable. To obtain the distribution for HBr vibrational energy, we need to separate the rotational motion from the relative vibrational motion.

From the final state analysis of the classical trajectory studies we know the final positions and momenta of $H(x_H,y_H,z_H,px_H,py_H,pz_H)$ and $Br(x_{Br},y_{Br},z_{Br},px_{Br},py_{Br},pz_{Br})$ atoms. Let us assume that the dissociating HBr is vibrating along an unit vector ($\hat{R}$) which is given as

$$\hat{R} = \frac{(x_{Br}-x_H)\hat{i}+(y_{Br}-y_H)\hat{j}+(z_{Br}-z_H)\hat{k}}{\sqrt{(x_{Br}-x_H)^2+(y_{Br}-y_H)^2+(z_{Br}-z_H)^2}} \tag{3.9}$$

where $\hat{i}, \hat{j}$ and $\hat{k}$ are the unit vectors along the mutually perpendicular Cartesian axis. The relative velocity of H atom with respect to Br atom can be expressed as

$$\hat{V}_{rel} = (V_x^{Br} - V_x^H)\hat{i} + (V_y^{Br} - V_y^H)\hat{j} + (V_z^{Br} - V_z^H)\hat{k} \tag{3.10}$$

where V_x^{Br} and V_x^H are the velocity components of the Br and H atom respectively along the x direction. Similarly, the superscript on V denotes the velocity of the atom and the subscript denotes the Cartesian component of the velocity.

Now the projection of the relative velocity vector $\hat{V}_{rel}$ on the unit vector $\hat{R}$ will give us the velocity (V_{vib}) purely due to vibration of HBr.

$$V_{vib} = \hat{V}_{rel} \bullet \hat{R} = |V_{rel}||R|\cos\theta \qquad (3.11)$$

where the θ is angle between the relative velocity vector and unit vector in the direction of vibration. Then the kinetic energy for the vibration (T_{HBr}) is

$$T_{HBr} = 0.5\mu V_{vib}^2 \qquad (3.12)$$

So the total vibrational energy for HBr will be

$$E_{HBr} = T_{HBr} + V_{HBr} + D_e \qquad (3.13)$$

where V_{HBr} is the potential energy for HBr and D_e is the dissociation energy for HBr.

The vibrational energy of HBr is calculated for all the trajectories that produce three-center HBr elimination. Total excitation energy is divided into several range and number of trajectories in a certain velocity ranges are counted. Then, number of trajectories versus vibrational energy (eV) of HBr are plotted in Figure 3.6a-c for three different PESes. These trajectory results are classical so we obtain a continuous distribution of HBr vibrational energies on each surface. In the figures 3.6a-c, the points are the trajectory data and the curves are the nonlinear least-squares fit to the function

$$P(E_v) = A*\exp(-E_v/kT) \qquad (3.14)$$

to these data. A and T are treated as parameters to be adjusted to the data. In figures 3.7a-c, we have plotted $\ln(P(E_v))$ versus E_v. If the distribution is Boltzmann, this should yield a straight line except for the statistical errors present in the trajectory calculations. From these least-squares fits, we obtain an equation for the classical distribution. These equations are shown at the top of each plot.

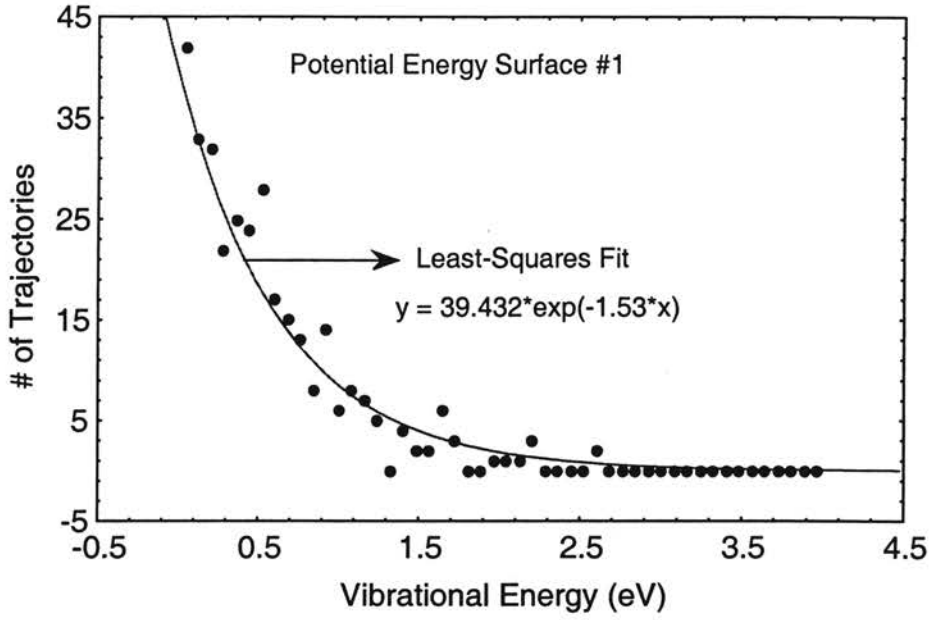

Figure3.6a

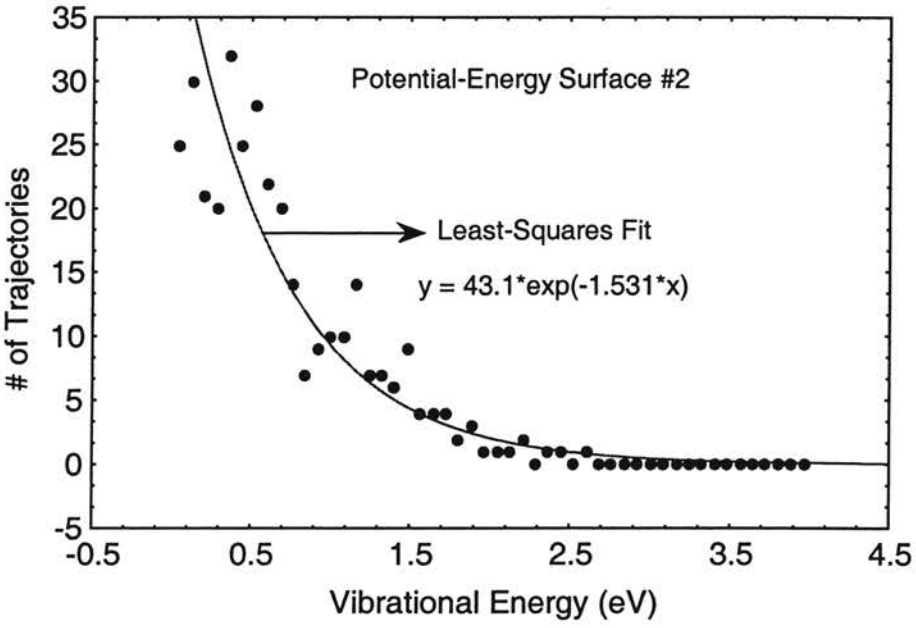

Figure 3.6b

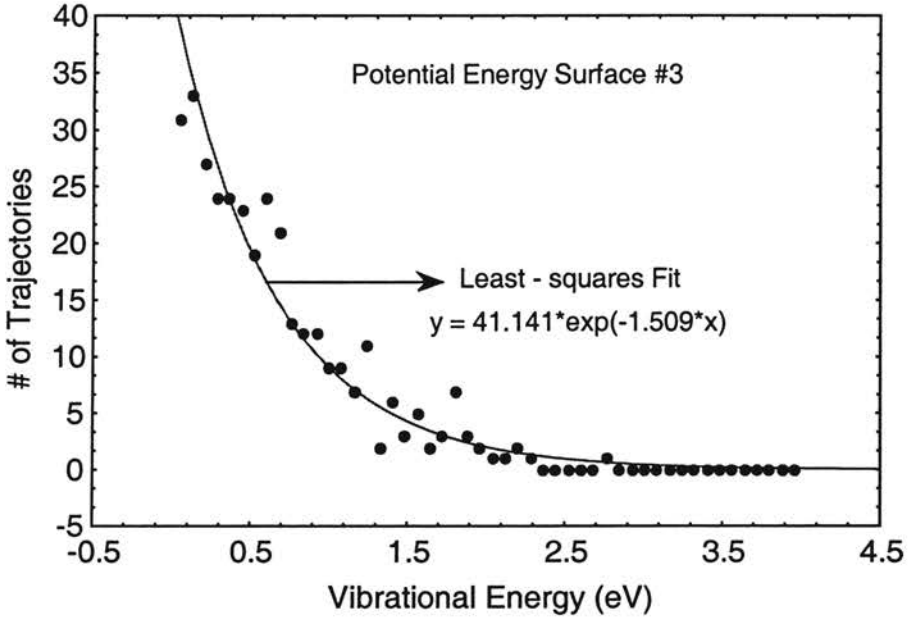

Figure3.6c

Figures 3.6a-c are the plots of number of trajectories versus vibrational energy (eV) obtained from PES1, PES2 and PES3 respectively. The • are the calculated data points. The lines in the above plots are the least-squares fit to the data points and the fitted equations are also shown in figures.

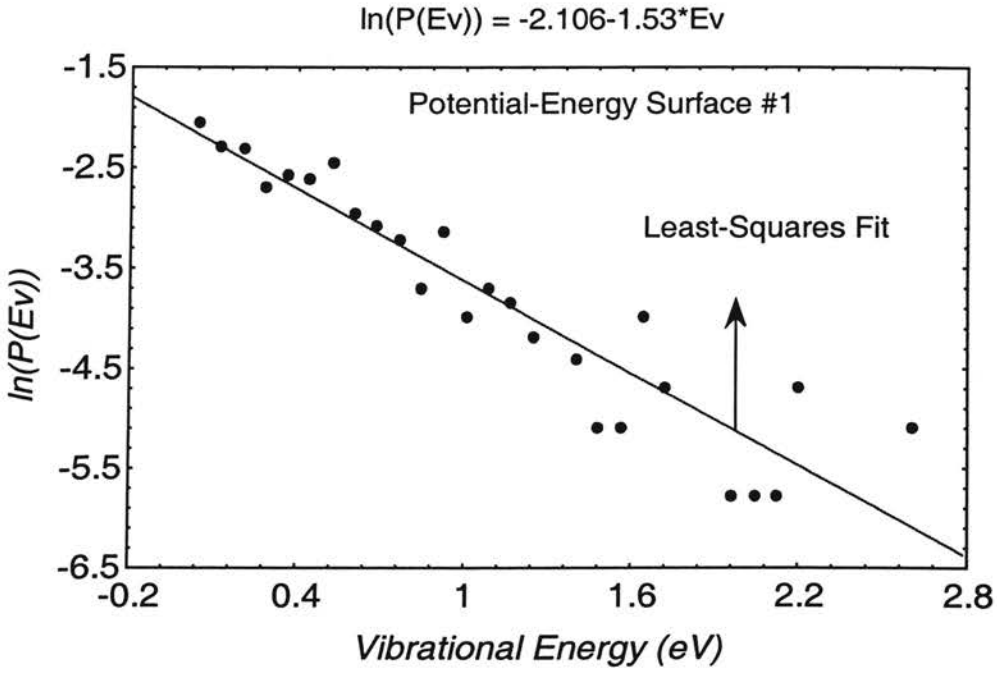

Figure3.7a

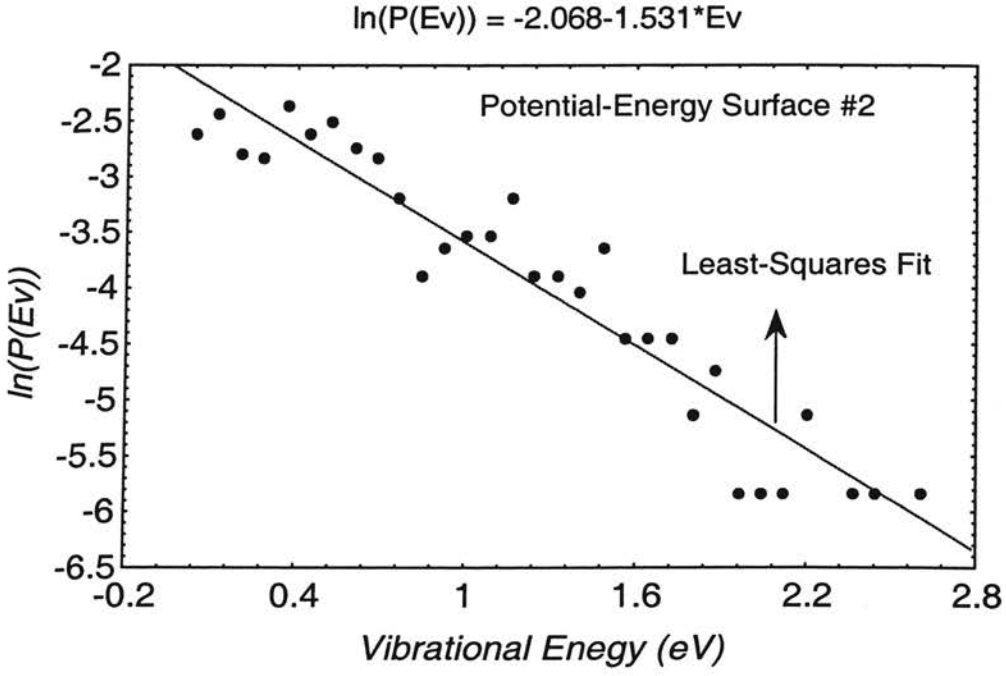

Figure 3.7b

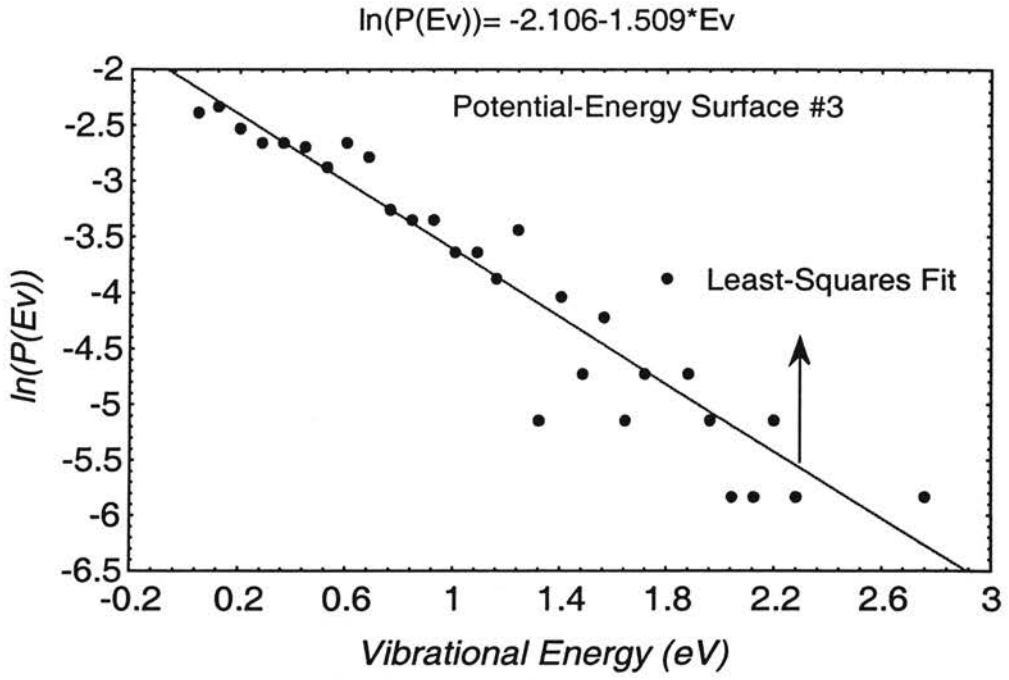

Figure 3.7c

Figures 3.7a-c are the plots of $\ln(P(E_v))$ versus E_v for PES1, PES2 and PES3 respectively at an excitation energy 6.44 eV. The •'s are the *ab initio* data and the line is the least-squares fit to the data. The equation of the fitted line is shown on the top of each plot.

Recently Dai *et al.*[9] have carried out the photolysis experiments on vinyl bromide at 193 nm (6.44 eV). They have fitted the vibrational energy distribution of HBr with Botlzmann distribution. To compare the vibrational energy-distribution of HBr obtained from present classical trajectory calculations we have 'bin' the classical energies so that they become quantized as are experimental data. This is done in the following manner:

Let the energy of the v<u>th</u> HBr vibratonal state be

$$E_v = (v+0.5)h\nu_o - (v+0.5)^2 w_e x_e \qquad (3.15)$$

Where ν_o is the measured fundamental vibrational frequency of HBr and $w_e x_e$ is the measured anharmonicity factor. These values are taken from Herzberg's compilation[10]. We assume that any trajectory that yields an energy, E, in the range $E_v \leq E < E_{v+1}$ is in the vth vibrational quantum state. Using least-squares fits from the classical distribution functions, the number range, N_v, is given by

$$N_V = \int_{E_v}^{E_{v+1}} A \exp(-E/kT) dE \tag{3.16}$$

Finally, to compare the experimental data, we must normalize both distributions in the same manner. That is, we multiply the N_v values by a constant, c, requires that

$$\sum_{v=1}^{6} c N_v = 1 \tag{3.17}$$

This gives the value of c and provides us a normalized distribution of cN_v values. We execute the same operations with the experimental data i.e., we normalize the experimental relative populations such that we have

$$\sum_{v=1}^{6} c N_v^{\exp} = 1 \tag{3.18}$$

where N_v^{exp} are the relative populations. These calculations yield the relative populations at an excitation energy 6.44 eV. In Table 3.5 we have tabulated the relative populations obtained from three different surfaces and experiments.

Table 3.5

Comparisons of relative normalized populations obtained from trajectory calculations on three potential-energy surfaces with those from photolysis experiments[9] at an excitation energy E_{ex} = 6.44 eV.

Normalized relative population	PES1[a]	PES2[a]	PES3[a]	Expt[b]
v = 1	0.406	0.406	0.403	0.409
v = 2	0.246	0.246	0.246	0.247
v = 3	0.161	0.160	0.161	0.151
v = 4	0.087	0.087	0.088	0.084
v = 5	0.061	0.061	0.062	0.060
v = 6	0.039	0.039	0.040	0.039

[a] indicates the results obtained from trajectory calculations and [b] indicates the results obtained from photolysis experiments (Ref: 9).

To obtain an effective temperature from our calculated data, we have fitted the normalized relative populations at 6.44 eV excitation energy to the function

$$P(E_v) = A\exp\left[-\frac{(v+0.5)hv_o - (v+0.5)^2 w_e x_e}{kT}\right] \qquad (3.19)$$

with A and T being fitting parameters. The results are the temperatures T = 7084K, 7075K and 7165K from PES1, PES2 and PES3 respectively. Plots of calculated and experimental results are shown in the Figure 3.8. Some of the points in the Figure 3.8, superimposed on each other which makes it difficult to visualize them. The excellent agreement between calculated and experimental results are remarkable. The results obtained from three different PESes differ a little from each other. The vibrational

temperatures obtained from three surfaces are quite in good agreement with the experimental value T_{exp} = 6999K. The vibrational temperature obtained from PES2 matches very close to the experimental value where as the vibrational temperature obtained from PES3 differ the most (by 166K).

Furthermore, the good agreement of HBr vibrational energy distribution with experiments and our calculations indicate that three-center HBr dissociation takes place on ground-state potential-energy surface not from the electronically excited surfaces. However, Br atom dissociation takes place from the excited potential-energy surface.[11]

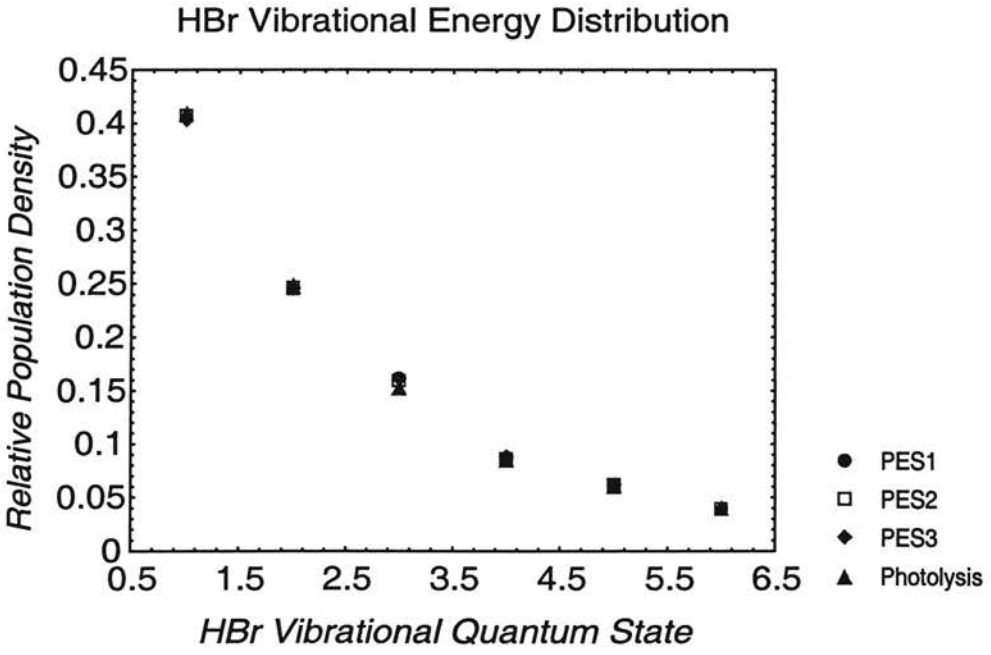

Figure 3.8. Plot of relative population density versus HBr vibrational quantum state obtained from trajectory calculations on three potential-energy surfaces and photolysis experiments at an excitation energy 6.44 eV.

Reference:

1. L. M. Raff and D. L. Thompson, The Classical trajectory Approach to Reactive Scattering. In *Theory of Chemical Reaction Dynamics*; M. Baer, Ed.CRC Press: Boca Raton, FL,Vol III, 1 (1985).

2. L. M. Raff, *J. Chem. Phys.* **90**, 6313 (1989).

3. L. M. Raff, *J. Chem. Phys.* **95**, 8901 (1991).

4. L. M. Raff, *J. Chem. Phys.* **89**, 5680 (1988).

5. H. Margenau and G. M. Murphy, *The Mathematics of Physics and Chemistry*, D. Van Nostrand Company Inc. Princeton, NJ, (1957).

6. S. A. Abrash, R. W. Zehner, G. J. Mains and L. M. Raff, *J. Phys. Chem.* **99**, 2959 (1995).

7. K. Saito, T. Yokubo, T. Fuse, H. Tahara, O. Kondo, T. Higashihara and I. Murakami, *Bull. Chem. Soc. Jpn.* **52**, 3507 (1979).

8. L. M. Raff, *J. Phys. Chem.* **91**, 3266 (1987); L. M .Raff, *J. Phys. Chem.* **92**, 141 (1988); L. M .Raff and R. W. Graham, *J. Phys. Chem.* **92**, 5111 (1988); L. M .Raff, *J. Chem. Phys.* **93**, 3160 (1990); L. M. Raff, *J. Chem. Phys.* **97**, 7459 (1992).

9. Dean-Kuo Liu, Laura Letendre, Hai-Lung Dai, Joshua B. Halpern and Charles D. Pibel, *J. Chem. Phys.* (to be submitted).

10. G. Herzberg, *Spectra of Diatomic Molecule*, D. van Nostrand Co, Inc., New York, (1950).

11. G. J. Mains, L. M. Raff, S. A. Abrash, *J. Phys. Chem.* **99**, 3532(1995).

CHAPTER IV

STUDIES OF INTRAMOLECULAR ENERGY TRANSFER RATES IN VINYL BROMIDE ON THREE POTENTIAL-ENERGY SURFACES

I. Introduction

Intramolecular vibrational energy transfer plays an important role in unimolecular dissociation reactions. The computation of the rates and pathways of intramolecular energy flow for highly coupled polyatomic systems has proven to be difficult. Generally, classical studies of intramolecular energy transfer involve the integration of the Hamilton's equations of motion on a given potential-energy surface. 'Bond' or 'mode' energies are calculated from the results. Intramolecular energy transfer rates and pathways are inferred from the time variation of 'bond' or 'mode' energies.[1] This procedure involves an arbitrary definition of the bond energy which generally assumes a mode separability that does not exist. Consequently, all potential and kinetic coupling terms involving the mode coordinates are omitted from the definition. Therefore, one can never be certain whether a variation in the bond energy is due to actual energy transfer or from the other modes or merely to changes in the magnitudes of the omitted coupling terms. It also not possible to be certain that the results themselves are not dependent upon the arbitrary definition adopted for bond and mode energy. It has previously been shown[2] that these problems can be eliminated by analyzing the internal energy flow

from the envelop functions of the temporal variations of the mode kinetic energies computed using a coordinate system that diagonalizes the kinetic energy matrix.

Using this method, we have investigated intramolecular energy transfer rates and pathways on three potential-energy surfaces, PES1, PES2 and PES3 which have been described in Chapter II. Comparison of the results obtained on each of these surfaces will allow us to determine the effects of different topological features of the PES on the intramolecular energy transfer rates and pathways.

II. Computational Methods and Potential-Energy Surface

A) Computational Methods.

To obtain quantitative information about the intramolecular energy transfer dynamics, we have used the projection method[2]. This method involves the calculation of the temporal variation of a diagonal kinetic energy matrix. The energy transfer rates and pathways are extracted from the envelope function of this temporal variation. Since the potential energy is not involved in the analysis, all the problems associated with potential coupling between vibrational modes are eliminated.

Let $\mathbf{L_i}$ (i=1,2,3,…,3N) represent a set of normalized (3N×1) transformation vectors that project the normal mode vibrational coordinates, $\mathbf{Q_i}$ ($1 \leq i \leq 3N-6$), three center-of-mass translations, $\mathbf{Q_i}$ ($3N-5 \leq i \leq 3N-3$), and rotations about the center-of-mass, $\mathbf{Q_i}$ ($3N-2 \leq i \leq 3N$) onto the Cartesian displacements $\mathbf{q_j}$ (j =1,2,3, ….., 3N). At time, t, the

instantaneous Cartesian velocities can be written as a linear combinations of the elements of $\dot{\mathbf{Q}}_i$:

$$\dot{q}_i(t) = \sum_{j=1}^{3N} \dot{Q}_j(t) L_{ij} \qquad \text{for i = 1, 2, 3, ..., 3N} \tag{4.1}$$

Equation 4.1 can be rewritten in the matrix from as

$$\dot{\mathbf{q}}(\mathbf{t}) = \mathbf{L}\dot{\mathbf{Q}}(\mathbf{t}) \tag{4.2}$$

where $\mathbf{L}$ is a (3N × 3N) square matrix whose columns are the normalized projection vectors $\mathbf{L}_i$. $\dot{\mathbf{q}}(\mathbf{t})$ is a (3N × 1) column vector whose elements are the Cartesian velocities and $\dot{\mathbf{Q}}(\mathbf{t})$ is a (3N × 1) column vector whose elements are the normal mode, center-of-mass and rotation velocities. Therefore, the normal mode velocities are given by

$$\dot{\mathbf{Q}}(\mathbf{t}) = \mathbf{L}^{-1}\dot{\mathbf{q}}(\mathbf{t}) \tag{4.3}$$

The kinetic energy T at time t is

$$T(t) = 0.5\sum_{i=1}^{3N} m_i \dot{q}_i^{\,2}(t) \tag{4.4}$$

Substitution of equation 1 yields

$$T(t) = 0.5\sum_{i=1}^{3N} m_i \sum_{j=1}^{3N}\sum_{k=1}^{3N} \dot{Q}_j(t)\dot{Q}_k(t) L_{ij} L_{ik}$$

$$= 0.5\sum_{i=1}^{3N} m_i \sum_{j=1}^{3N} \dot{Q}_j^{\,2}(t) L_{ij}^{\,2} \tag{4.5}$$

since the kinetic energy is diagonal when expressed in terms of the normal mode velocities. So the kinetic energy can be written as

$$T(t) = \sum_{j=1}^{3N} a_j \dot{Q}_j^{\,2}(t) \tag{4.6}$$

provided the mode constant a_j is defined as

$$a_j = 0.5\sum_{i=1}^{3N} m_i L_{ij}^{\ 2} \tag{4.7}$$

Equation 4.6 indicates that the total molecular kinetic energy is the uncoupled sum if the individual mode kinetic energies, $T_i(t)$,

$$T_i(t) = a_i \dot{Q}_i^{\ 2}(t) \tag{4.8}$$

The total energy associated with a given mode alternates between potential and kinetic energy with a frequency characteristic of the mode fundamental. The energy flow from or to the mode can be determined from the slope of the envelope of these oscillations. A large slope of the envelope function indicates a rapid energy transfer and a zero slope of the envelope function indicates no energy transfer. Thus, the energy flow through the molecule may be determined directly from the temporal variation of the envelopes of the mode kinetic energies.

We may also use the time-averaged kinetic energy to obtain an estimate of the average energy in a particular mode. Over the period from t_0 to $t_0 + \Delta t$, the average kinetic energy is given by

$$\langle T_i \rangle = (\Delta t)^{-1} \int_{t_0}^{t_0+\Delta t} T_i(t)dt \tag{4.9}$$

Therefore, the average mode energy over this same period is approximately,

$$\langle E_i(t) \rangle = 2(\Delta t)^{-1} \int_{t_0}^{t_0+\Delta t} T_i(t)dt$$

$$= 2(\Delta t)^{-1} \int_{t_0}^{t_0+\Delta t} a_i \dot{Q}_i^{\ 2}(t) \tag{4.10}$$

where t is time in the interval $t_0 \le t \le t_0+\Delta t$. The time interval Δt is chosen in such a way

that most of the fluctuations in $T_i(t)$ due to beats and interconversion of potential and kinetic energy average out within the same mode.

If the initial excitation energy is inserted into mode i, the temporal variation of $\langle E_i(t) \rangle$ is directly related to the rate of energy flow out of this mode. We have assumed that this energy flow can be adequately described by a first-order rate law. However, this assumption is not rigorously true. Under the above conditions, the intramolecular energy transfer rate coefficient k_i can be determined by fitting the flowing equation

$$\langle E_i(t) \rangle = E_i(0) exp[-k_i t] + (1 - exp[-\alpha_i t]) \langle E_i(\infty) \rangle \qquad (4.11)$$

to the data obtained from equation 4.10. In equation 4.11, k_i, α_i, $\langle E(\infty) \rangle$ are parameters representing the total relaxation rate coefficient of mode i, and an average total rate coefficient for energy transfer into the mode i, and the statistical equilibrium value of $\langle E_i(t) \rangle$ at infinite time, respectively.

B. Potential-Energy Surfaces.

We have used three different potential-energy surfaces with different topological features for the present studies. Potential surface PES1 is developed by fitting the *ab intio* and experimental data as described in Chapter II. This surface over estimates the vibrational frequencies which is apparent from the fact that *ab initio* calculations generally determine the vibrational frequencies with 5-10% error limits. To correct for this we have modified PES1 to obtain PES2 where the fundamental vibrational frequencies are in close agreement with the experimental IR frequencies. Ultimately, we developed PES3 with a new type of switching function by modifying PES2 in such a way

that PES3 has different curvature along the reaction coordinate than PES2. The detailed descriptions of all three potential-energy surfaces are given in Chapter II. In Table 4.1, we summarized the results of normal mode analysis obtained from three PES surfaces and compared with experimental vibrational frequencies[3].

Table 4.1

Descriptions of twelve vibrational normal modes of vinyl bromide

Mode no.	Description of mode	ν^a (cm^{-1})	ν^b (cm^{-1})	ν^c (cm^{-1})	Exp[d] (cm^{-1})
ν_1	C-C-Br bending	335	340	340	344
ν_2	CHBr wag	581	570	571	583
ν_3	C-Br stretch	593	603	603	613
ν_4	CH_2 wag	986	902	902	902
ν_5	CH_2-CHBr torsion	1053	953	953	942
ν_6	C-C-H^5 bending	1130	1022	1022	1006
ν_7	C-C-H^3bending	1142	1231	1231	1256
ν_8	H-C-H bending	1375	1396	1396	1373
ν_9	C=C stretch	1765	1603	1603	1604
ν_{10}	C-H stretch	3386	3015	3008	3027
ν_{11}	C-H stretch	3478	3087	3085	3086
ν_{12}	C-H stretch	3520	3135	3136	3113

Calculated by normal mode analysis on the surface [a] PES1, [b] PES2 and [c] PES3.

[d] Reference 3.

C. Numerical Procedures.

The initial states of the trajectories are prepared in the same manner as described in Chapter III. Initially, vinyl bromide is placed in the equilibrium geometry predicted by the global potential-energy surface. Zero-point energy is inserted into each mode of the

vinyl bromide using equation 4.1 with $\dot{\mathbf{Q}}_i(\mathbf{t})$ for rotation and translation set to zero. Hamilton's equations of motions are then integrated with a randomly chosen period t_p given by

$$t_p = \xi\tau \qquad (4.12)$$

where ξ is a random number selected from a distribution that is uniform on the interval [0,1] and τ is the characteristic period of the lowest frequency vibrational mode. The numerical integration is carried out using forth-order Runge-Kutta procedure with a fixed time step of 0.01 tu (0.0001019 ps). Equation 4.12 effectively averages over the vibrational phases. Subsequent to the above integration, the desired excitation energy, E_{ex}, is inserted to the selected mode k. This is done by first using equation 4.3 to project out the instantaneous normal mode velocities, $\dot{\mathbf{Q}}_i(\mathbf{t_p})$. The velocity, $\dot{Q}_k(\mathbf{t_p})$ is then altered to $\dot{Q}_k'(t_p)$ to reflect the insertion of the excitation energy E_{ex}. The altered velocity is given as

$$\dot{Q}_k'(t_p) = \pm\left\{(a_k)^{-1}\left[a_k \dot{Q}_k^{\,2}(t_p) + E_{ex}\right]\right\}^{1/2} \qquad (4.13)$$

where the sign is chosen randomly. The new Cartesian velocities are computed using equation 4.1. In the current studies, we have taken E_{ex} = 3.0 eV.

The trajectories are integrated for a time period of 450 tu (4.586 ps) to determine the nature of the energy transfer. After every 10th integration step equation 4.3 is used to compute the instantaneous values of the $\dot{\mathbf{Q}}_i(\mathbf{t})$ (i =1,2,3, ..., 3N). The mode kinetic energies are calculated using equation 4.8. Approximate average mode energies at time t^* are obtained from equation 4.10 using Δt =25 tu (0.255 ps) and $t^* = t_0 + \Delta t/2$.

III. Results and Discussions

A. Energy Transfer Rates and Pathways

To compare the results obtained from three PESs with those obtained from the empirical potential-energy surface (EPS)[4], we have initially inserted the excitation energy E_{ex} =3.0 eV in the C-H stretching mode, ν_{10}, and examined the pathways and rates of intramolecular energy flow from this mode to the other modes in vinyl bromide. The temporal variations of the instantaneous mode kinetic energies are computed using Equation 4.8 for each of the three PESs. Figures 1a-1d, 2a-2d and 3a-3d show the variation of instantaneous mode kinetic energies with time for PES1, PES2 and PES3 respectively. Examinations of these figures reveal some of the important qualitative features of the intramolecular energy transfer dynamics for vinyl bromide in the near equilibrium geometry.

i) Energy Transfer Pathways on PES1

Figure 4.1a shows the kinetic energies in the low frequency C-C-Br bending, CHBr wag, and C-Br stretching mode while Figure 1d shows the corresponding results for the high frequency C-H stretching modes. The kinetic energies in the other bending, wags, torsion, and C=C stretching modes are shown in Figures 4.1b and 4.1c. Inspection of the kinetic energy in ν_{10} reveals that the envelope function decreases rapidly to the

near equilibrium levels in 5-10 t.u. indicating a very fast total energy transfer rate out of this mode.

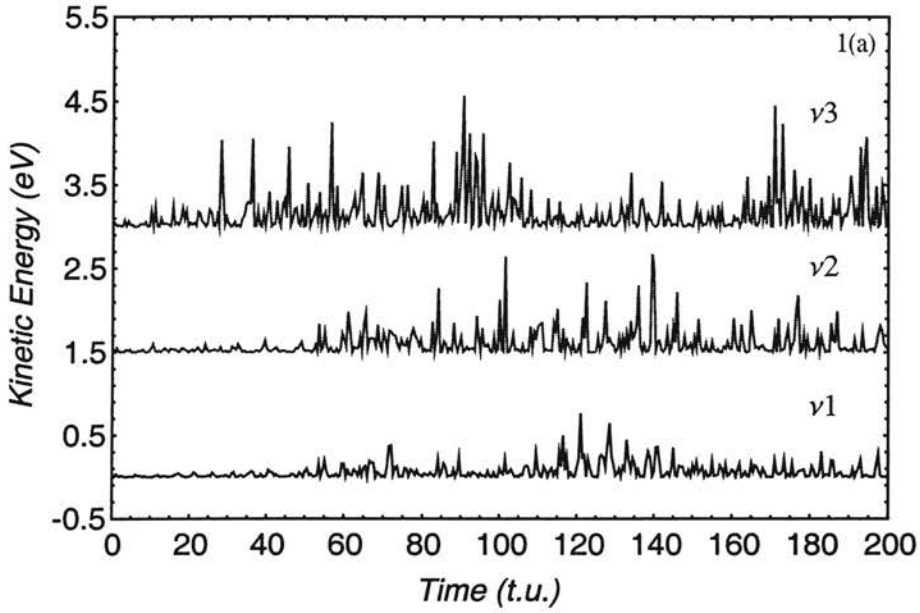

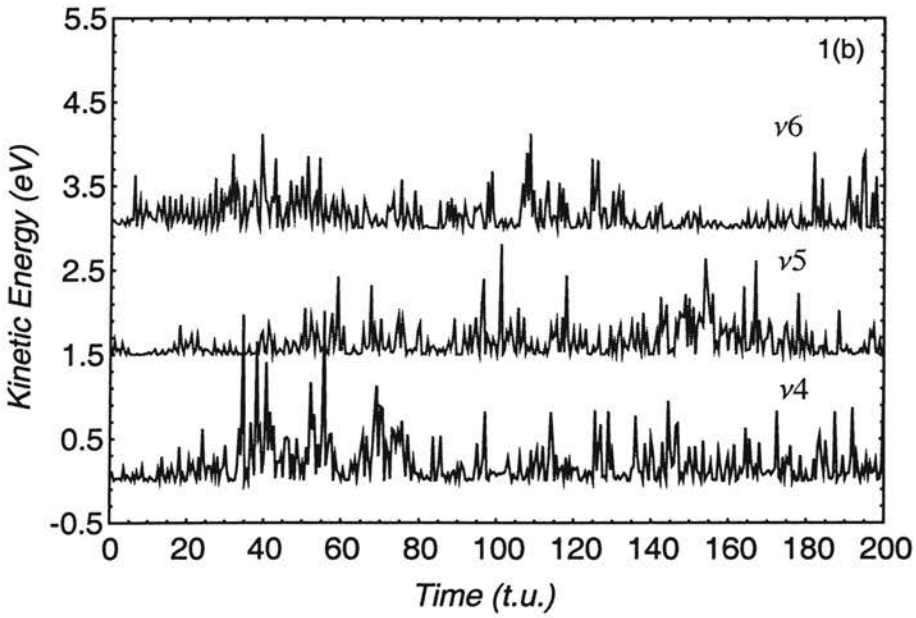

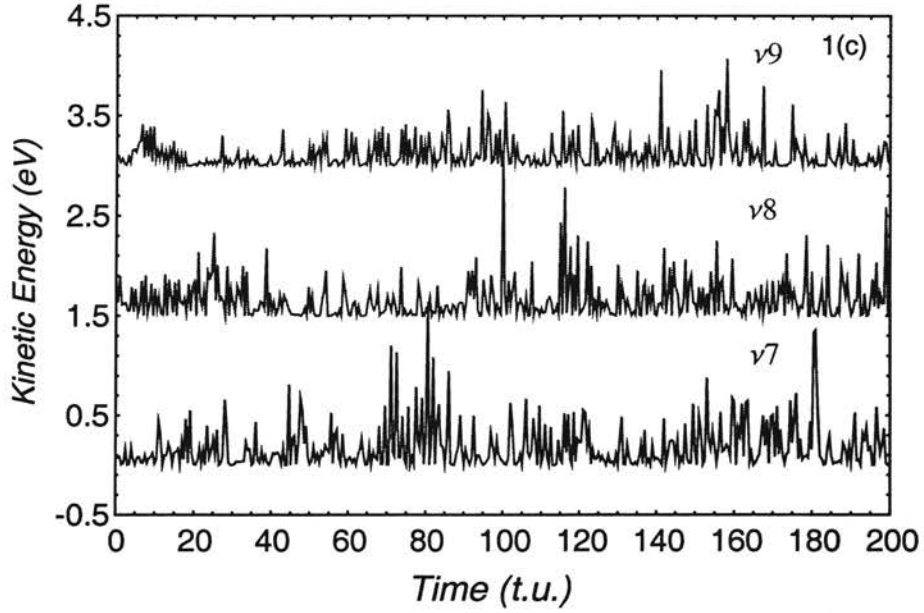

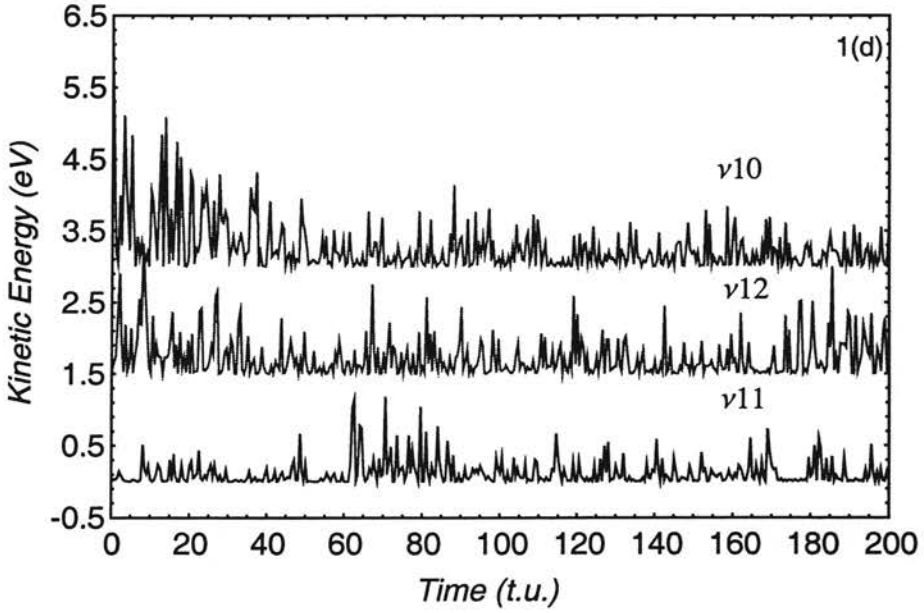

Figures 4.1a-d. Temporal variations of the mode kinetic energy for each of the 12 vibrational modes of vinyl bromide for the case in which 3.0 eV excitation energy is initially partitioned into the C-H stretching mode, ν_{10}, on PES1. Each successive curve is displaced upward by 1.5 eV for visual clarity. 1 t.u. = 0.01019 ps.

The pathways of energy flow from the mode ν_{10} for PES1 can be determined from the results in the Figure 4.1a-d. Apparently, the primary energy transfer pathway from ν_{10} is to ν_{12} since only ν_{12} has a kinetic energy amplitude that increases rapidly over the first 4 t.u. At around 7 t.u., the energy begins to flow into the third C-H stretching mode ν_{11}. The kinetic energy in ν_8 mode also increases over the first 5 t.u.

The secondary pathways for the energy transfer can also be inferred from the plot shown in Figure 4.1. At around 10 t.u., the kinetic energy in the C- C-H bend, ν_6, begins to increase. The C=C stretching mode, ν_9, and the C-C-H[3] bending mode, ν_7, also gain energy at this time.

Around 20 t.u., the CH_2 wag, ν_4, and the C-Br stretch, ν_3, start gaining kinetic energy. Since the kinetic energy in these modes fails to increase significantly during the initial 20 t.u., it is reasonable to conclude that the energy flow is from the C-C-H bending or C=C stretching not from the C-H stretches. All the other modes are essentially inactive during primary, secondary and tertiary phases of the energy transfer.

After 60 t.u., C-C-Br bending, ν_1, CHBr wag, ν_2, and CH_2-CHBr torsion, ν_5, begin to gain energy. These energy transfer processes are probably due to the coupling of these modes with C-Br stretch and CH_2 wag.

ii) Energy Transfer Pathways on PES2

Inspection of Figures 4.2a-d provides us a quantitative description of the pathways for energy transfer from mode ν_{10} to the other modes on PES2. The primary energy transfer pathway from ν_{10} is to ν_{12} followed by ν_{11} which is probably due to the

near resonance between the C-H stretches. This is very similar to the energy transfer dynamics obtained using PES1.

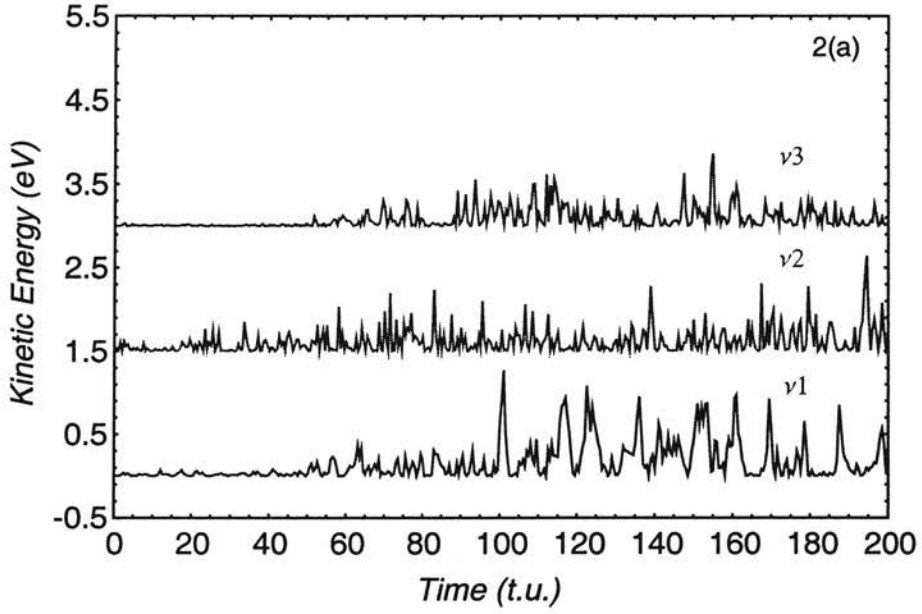

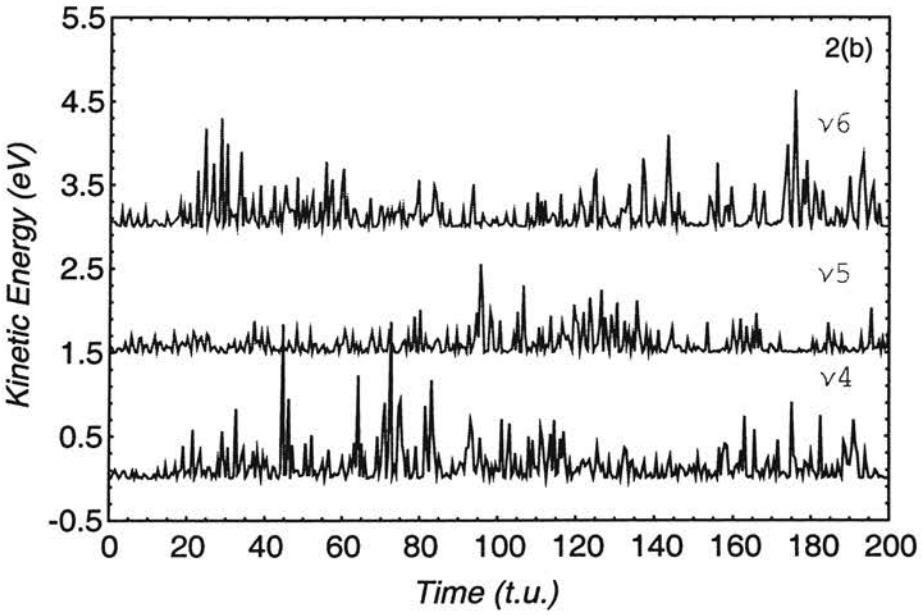

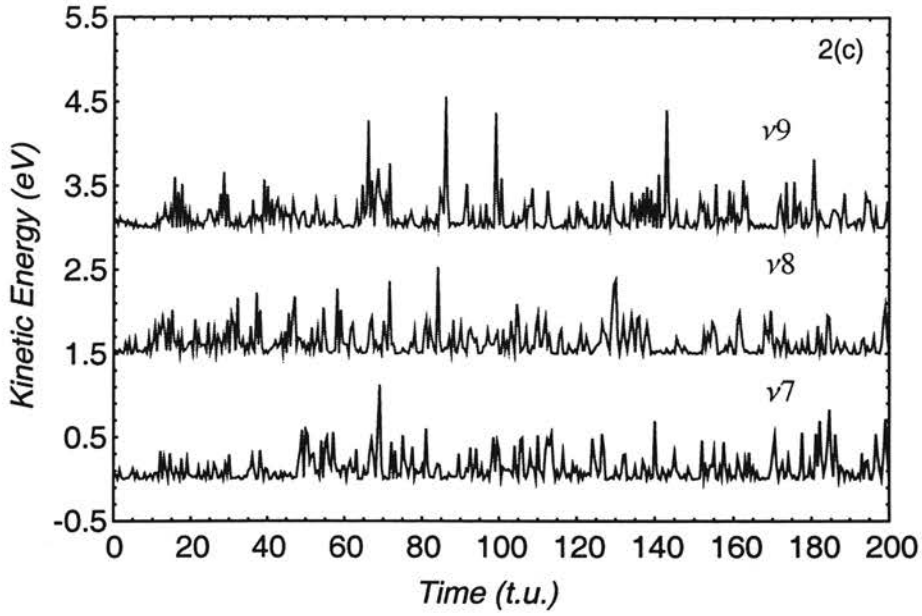

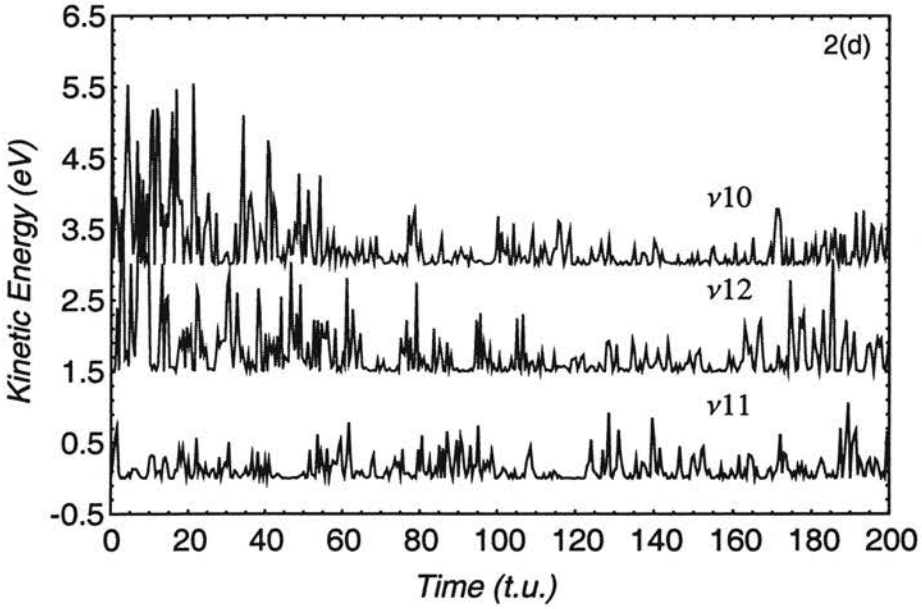

Figures 4.2a-d. Temporal variations of the mode kinetic energy for each of the 12 vibrational modes of vinyl bromide for the case in which 3.0 eV excitation energy is initially partitioned into the C-H stretching mode, ν_{10}, on PES2. Each successive curve is displaced upward by 1.5 eV for visual clarity. 1 t.u. = 0.01019 ps.

The secondary pathways for the energy transfer occur between 10-20 t.u. During this time, ν_7, ν_8 and ν_9 gain kinetic energy which presumably comes from the C-H stretching modes. Thus secondary pathways are very similar to those seen on surface PES1. However, energy transfer to the C-C-H bending mode, ν_6, is now delayed.

Around 20 t.u., ν_4 and ν_6 start gaining kinetic energy. Since during times prior to 20 t.u., these modes fail to gain kinetic energy, we can conclude that energy flow to ν_4 and ν_6 are from ν_8 and ν_9, not from the C-H stretches.

After 60 t.u., ν_1, ν_2, ν_3, ν_5 and ν_7 modes begin to gain kinetic energy. These energy transfer processes are probably due to the coupling of these modes with ν_4 and ν_6 modes.

iii) Energy Transfer Pathways on PES3.

From Figures 4.3a-d, we can determine the qualitative energy transfer pathways from ν_{10} mode to other mode on PES3. The primary energy transfer pathway is from ν_{10} to ν_{12} followed by ν_{11}.

Around 10 t.u., ν_4, ν_7 and ν_8 start gaining kinetic energy. Thus the secondary energy transfer pathways are from the C-H stretches the to CH_2 wag, C-C-H^3 and H-C-H bending modes.

At 20 t.u. , ν_2, ν_5, ν_6 and ν_9 modes become vibrationally excited. Since these modes remain significantly inactive until this time, we conclude that the energy transfer pathways to these modes are from the CH_2 wag, C-C-H^5 and C-C-H^3 bending modes.

After 60 t.u., ν_1 and ν_3 start to gain kinetic energy. This transfer is probably due to coupling between these modes and ν_2, ν_5, ν_6 and ν_9.

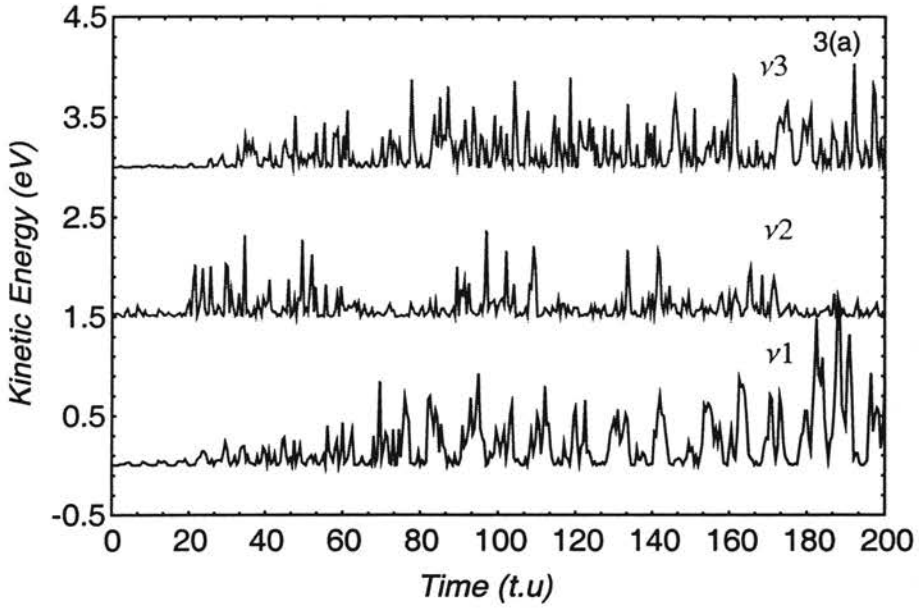

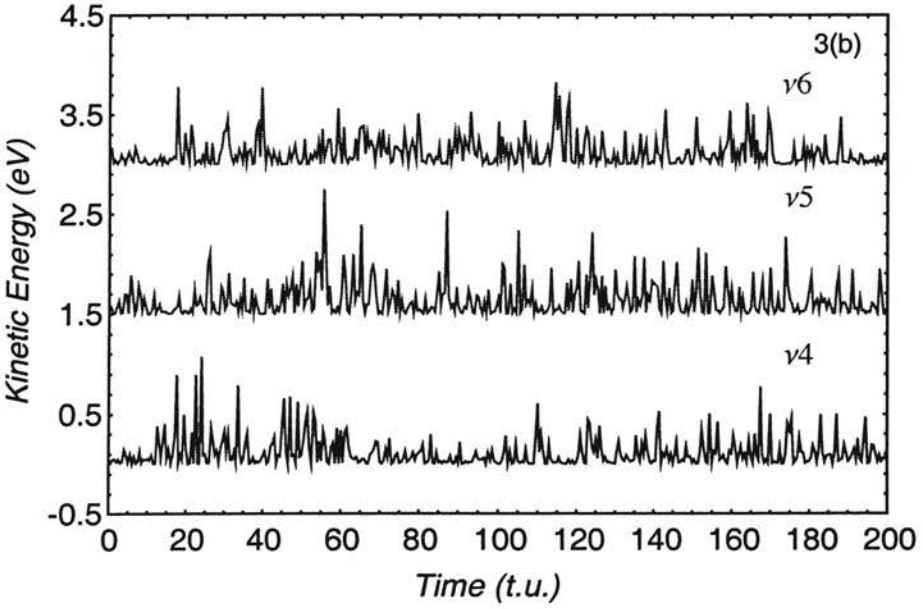

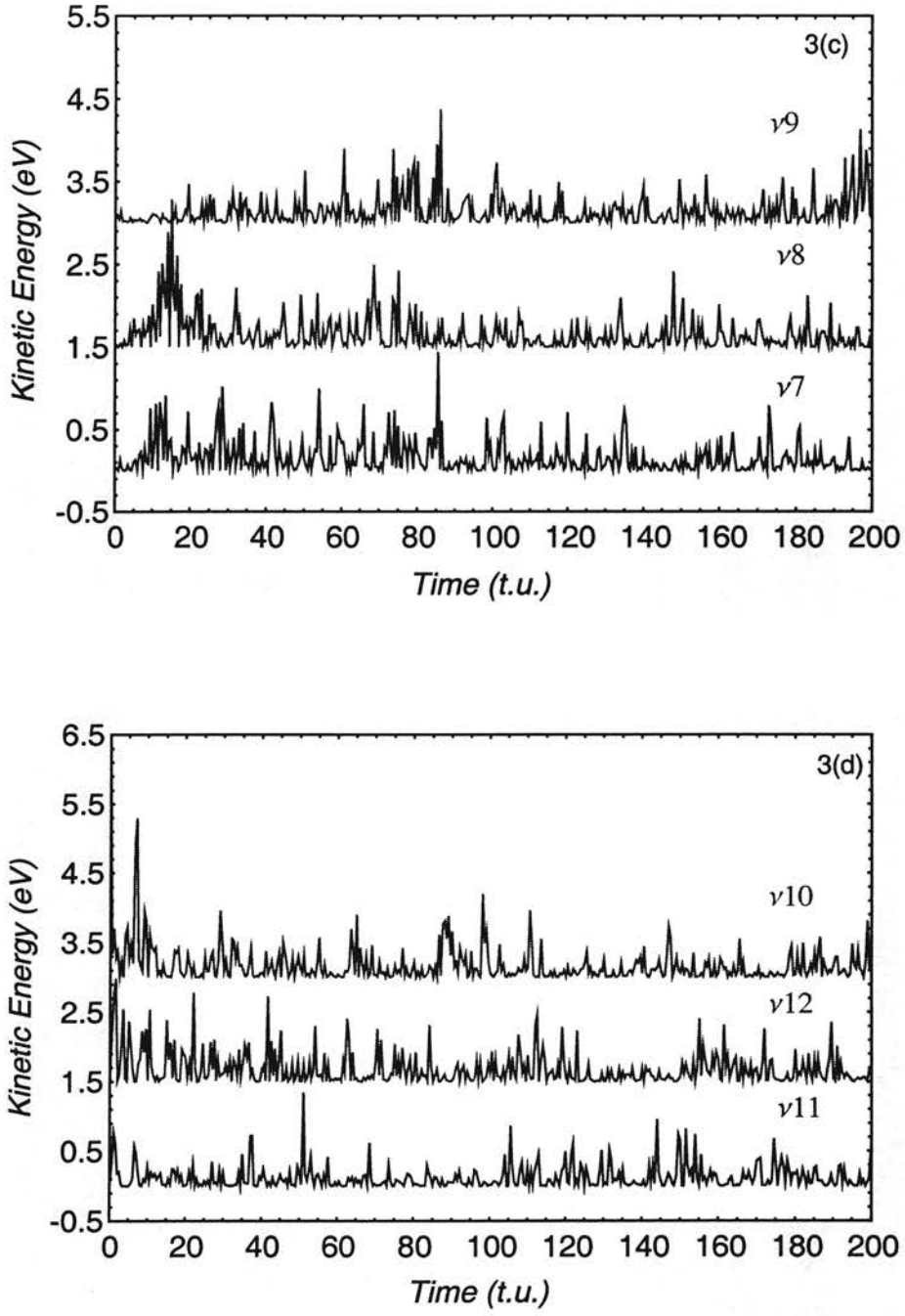

Figures 4.3a-d. Temporal variations of the mode kinetic energy for each of the 12 vibrational modes of vinyl bromide for the case in which 3.0 eV excitation energy is initially partitioned into the C-H stretching mode, ν_{10}, on PES3. Each successive curve is displaced upward by 1.5 eV for visual clarity. 1 t.u. = 0.01019 ps.

iv) Comparisons of the Energy Transfer Pathways Obtained from PES1, PES2, PES3 and EPS.

We have compared the above results and the results obtained by Pan and Raff[5]. The primary energy transfer pathways from ν_{10} to ν_{12} and ν_{11} are same for all the potential-energy surfaces. Other energy transfer pathways (secondary, tertiary and quaternary) show some variations from one PES to another.

The results obtained using surface EPS indicate that mode ν_7 remains inactive whereas the results obtained from the other PESes (PES1, PES2 and PES3) indicate that ν_7 gains energy through either via tertiary (in case of PES1 and PES3) or quaternary (in case of PES2) pathways.

For all surfaces, mode ν_1 gains energy via a quaternary process. For PES1, PES2 and EPS, energy transfer into mode ν_2 is quaternary process whereas for PES3 this transfer is tertiary. Quaternary processes transfer energy in mode ν_3 on both PES2 and PES3. On PES1 and EPS, this transfer appears to be tertiary. Transfer into the torsional mode (ν_5) is either quaternary (PES1 and PES2) or tertiary (PES3 and EPS). The C-C-H[5] bend (ν_6) gains energy in a secondary process from the C-H stretching modes on PES1. In contrast, this transfer is either tertiary (PES2 and PES3) or quaternary (EPS) on the more empirical surfaces. Energy transfer into the H-C-H bend (ν_8) is primary on *ab initio* surface. On PES2 and PES3, there is a delay in this transfer so that it appears to be secondary. On the empirical EPS surface, this transfer occurs only after 60 t.u. have elapsed so that it is quaternary. The C=C stretch (ν_9) gains energy in a secondary event on PES1 and PES2. As the surface becomes more empirical, coupling to this mode

decreases and transfer process becomes either tertiary (PES3) or quaternary (EPS). Energy transfer to the C-C-H[3] bend (ν_7) essentially does not occur on EPS in the first picosecond. In contrast, it is a secondary transfer process on PES1 and PES3. Table 4.2 summarizes these qualitative results.

Table 4.2

Qualitative description of energy transfer pathways in vinyl bromide subsequent to excitation of C-H bond ν_{10} with 3.0 eV of energy

Potential Surface	**PES1**	**PES2**	**PES3**	**EPS**
Primary Processes	$\nu_{10} \rightarrow \nu_{12}$ $\nu_{10} \rightarrow \nu_8$ $(\nu_{10}, \nu_{12}) \rightarrow \nu_{11}$	$\nu_{10} \rightarrow \nu_{12}$ $(\nu_{10}, \nu_{12}) \rightarrow \nu_{11}$	$\nu_{10} \rightarrow \nu_{12}$ $(\nu_{10}, \nu_{12}) \rightarrow \nu_{11}$	$\nu_{10} \rightarrow \nu_{12}$ $(\nu_{10}, \nu_{12}) \rightarrow \nu_{11}$
Secondary Processes	$(\nu_8, \nu_{10}, \nu_{11}, \nu_{12}) \rightarrow \nu_6$ $(\nu_8, \nu_{10}, \nu_{11}, \nu_{12}) \rightarrow \nu_7$ $(\nu_8, \nu_{10}, \nu_{11}, \nu_{12}) \rightarrow \nu_9$	$(\nu_{10}, \nu_{11}, \nu_{12}) \rightarrow \nu_8$ $(\nu_{10}, \nu_{11}, \nu_{12}) \rightarrow \nu_9$	$(\nu_{10}, \nu_{11}, \nu_{12}) \rightarrow \nu_4$ $(\nu_{10}, \nu_{11}, \nu_{12}) \rightarrow \nu_7$ $(\nu_{10}, \nu_{11}, \nu_{12}) \rightarrow \nu_8$	$(\nu_{10}, \nu_{11}, \nu_{12}) \rightarrow \nu_4$
Tertiary Processes	$(\nu_6, \nu_7, \nu_9) \rightarrow \nu_3$ $(\nu_6, \nu_7, \nu_9) \rightarrow \nu_4$	$(\nu_8, \nu_9) \rightarrow \nu_4$ $(\nu_8, \nu_9) \rightarrow \nu_6$	$(\nu_4, \nu_7, \nu_8) \rightarrow \nu_2$ $(\nu_4, \nu_7, \nu_8) \rightarrow \nu_5$ $(\nu_4, \nu_7, \nu_8) \rightarrow \nu_6$ $(\nu_4, \nu_7, \nu_8) \rightarrow \nu_9$	$\nu_4 \rightarrow \nu_3$ $\nu_4 \rightarrow \nu_5$
Quaternary Processes	$(\nu_3, \nu_4) \rightarrow \nu_1$ $(\nu_3, \nu_4) \rightarrow \nu_2$ $(\nu_3, \nu_4) \rightarrow \nu_5$	$(\nu_4, \nu_6) \rightarrow \nu_1$ $(\nu_4, \nu_6) \rightarrow \nu_2$ $(\nu_4, \nu_6) \rightarrow \nu_3$ $(\nu_4, \nu_6) \rightarrow \nu_5$ $(\nu_4, \nu_6) \rightarrow \nu_7$	$(\nu_2, \nu_5, \nu_6, \nu_9) \rightarrow \nu_1$ $(\nu_2, \nu_5, \nu_6, \nu_9) \rightarrow \nu_3$	$(\nu_3, \nu_5) \rightarrow \nu_1$ $(\nu_3, \nu_5) \rightarrow \nu_2$ $(\nu_3, \nu_5) \rightarrow \nu_6$ $(\nu_3, \nu_5) \rightarrow \nu_8$ $(\nu_3, \nu_5) \rightarrow \nu_9$

In broad terms, a comparison of Figures 4.1a-d with Figures in Reference 5 shows that energy transfer on the *ab initio* surface is more globally rapid than is the case for the empirical EPS surface. This is the result of our more systematic evaluation of mode-mode

couplings in the *ab initio* calculations. These results are not incorporated into EPS surface. Examination of Table 4.2 shows that the energy transfer dynamics on PES1 and PES2 are very similar. These surfaces are primarily *ab initio* potentials. When ad hoc changes are made in the reaction coordinate curvature to produce PES3 or if we fit only the barrier heights, product and reactant equilibrium geometries and fundamental frequencies and the thermochemistry of various reaction channels as was done to obtain the EPS surface, significant variations in the energy transfer dynamics arise. The most striking of these is the role played by the C-C-H[3] bending mode (ν_7). This mode is inactive during the first picosecond on the EPS surface whereas it contributes an important energy transfer pathway on the *ab initio* surface. We conclude that computation of intermode coupling are essential if energy transfer dynamics are to be accurately described.

B. First-Order Relaxation Model.

An approximate average total energy, $\langle E_i \rangle$, associated with a particular mode can be calculated using equation 4.10. It is much easier to visualize the temporal variation of $\langle E_i \rangle$ than the envelope of the mode kinetic energy. In Figure 4.4a-c, we represent the typical results for ν_6 and ν_{11} on PES1, PES2 and PES3 respectively, to compare our present results with those obtained from EPS[4]. In each case, 3.0 eV of excitation energy is partitioned into the vibrational mode being examined. In Figures 4.4a-c, the computed points are connected by lines to enhance visual clarity. Inspection of these figures indicates that the decay rate of ν_{11} is almost two times faster than that of ν_6 for surface

PES1. When ad hoc empirical adjustment are made to the experimental vibrational frequencies (PES2) or when the reaction coordinate curvature is arbitrarily altered (PES3), the inequality is reversed and the total relaxation rate out of ν_6 becomes much larger than that for ν_{11}.

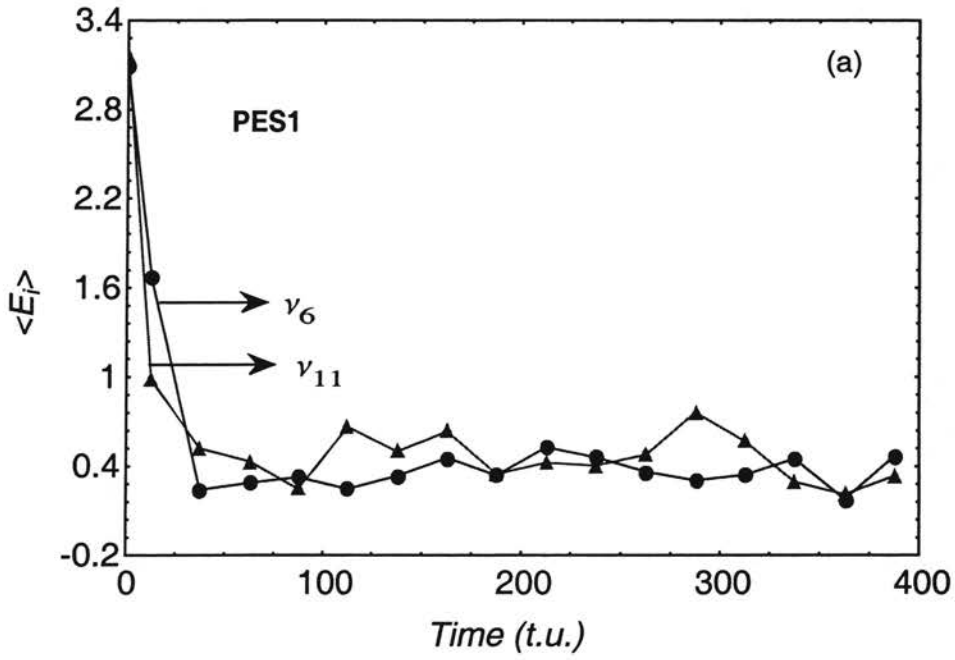

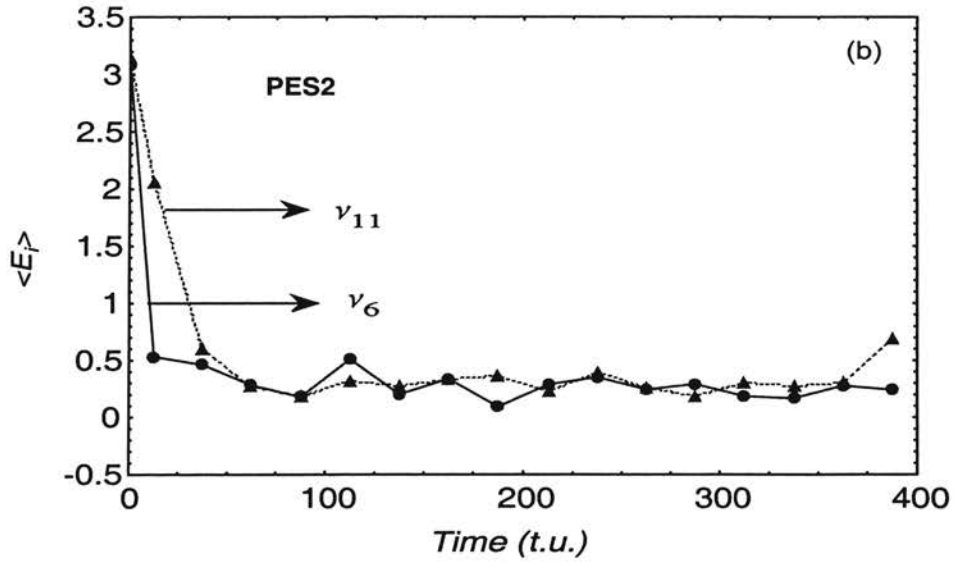

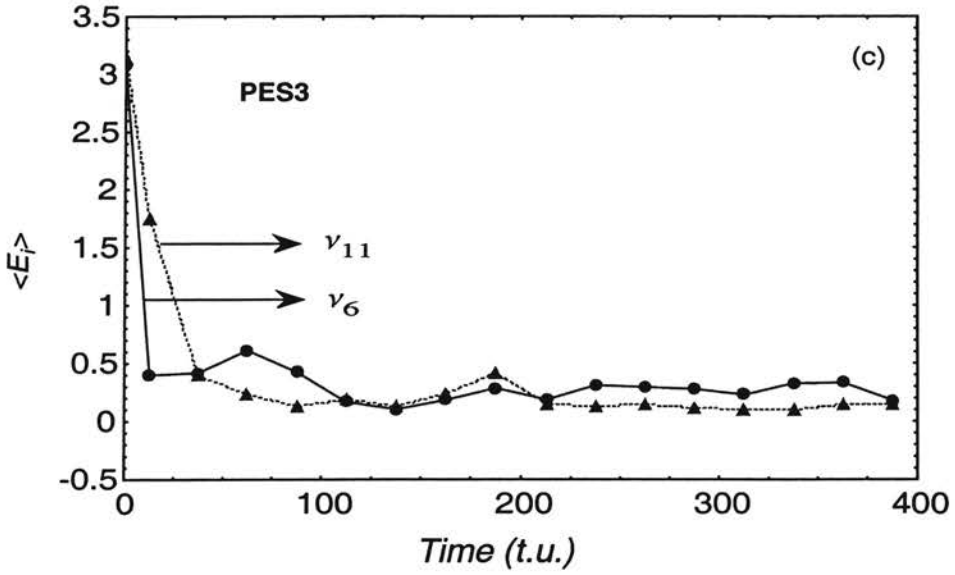

Figure 4.4a-c Decay curves for the average mode energies for initial excitation mode ν_6 and ν_{11} with 3.0 eV in excess of zero point energy for PES1, PES2 and PES3. (a) PES1; (b) PES2; (c) PES3. 1 t.u. = 0.01019 ps.

One can obtain a more quantitative measure of the total relaxation rates by fitting the data obtained from Eq.4.10 to Eq.4.11. In Eq. 4.11, k_i represents the total energy transfer rate coefficient from mode i. Thus we can write

$$k_i = \sum_{\substack{j=1 \\ j \neq i}}^{12} k_{ij} \tag{4.13}$$

where k_{ij} is the mode-to-mode energy transfer rate coefficient from mode i to mode j. Figures 4.5a-c show how well we can fit the data obtained from Eq. 4.10 using Eq. 4.11 for PES1, PES2 and PES3. In each case, 3.0 eV of excitation energy is initially partitioned into C=C stretch (ν_9). The points in the plots are computed using Eq. 4.10. The solid curve is the least-squares fit using Eq. 4.11 to these data points. It is clear from these figures, that the first-order model describes the major features of the energy transfer with sufficient accuracy.

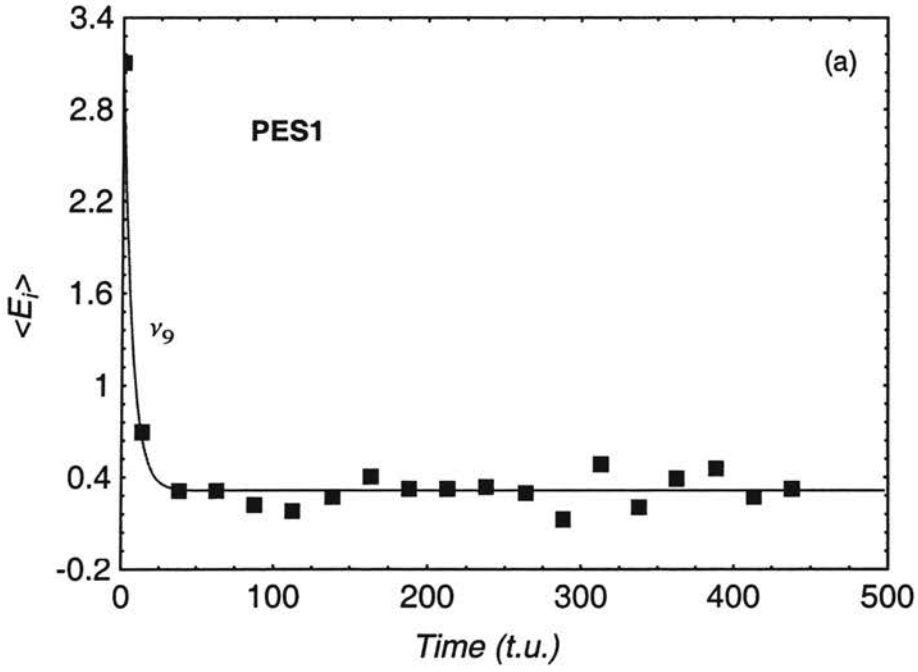

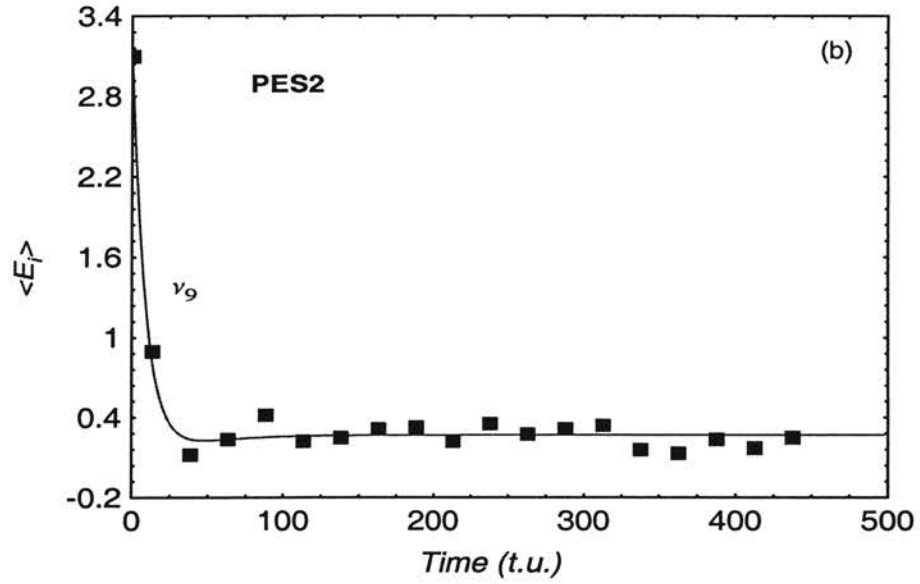

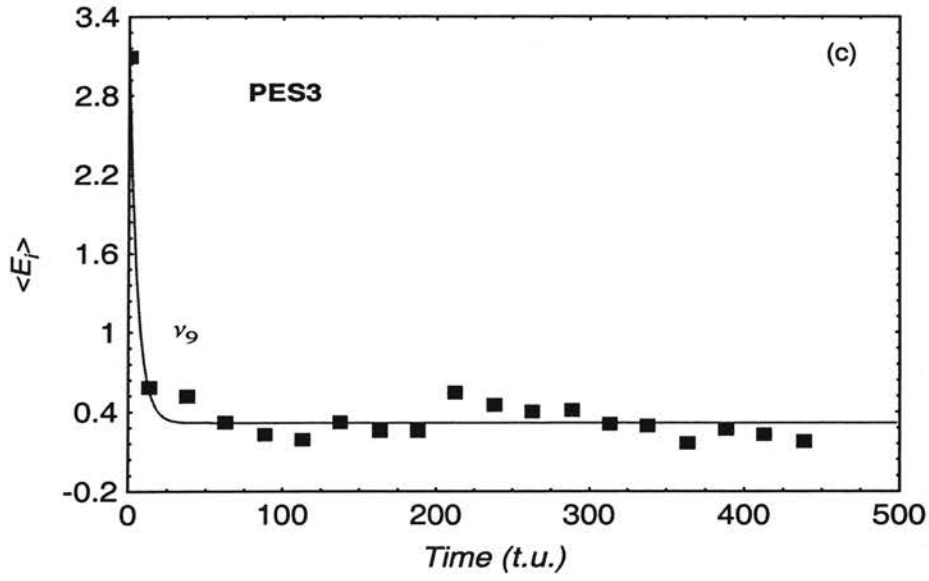

Figure 4.5.a-c Decay curves for the average mode energy for initial excitation of mode ν_9 with 3.0 eV in excess of zero-point energy for PES1, PES2 and PES3 respectively. The points are calculated using Eq. 4.10. The solid line is the least-squares fit to the points using Eq. 4.11. (a) PES1; (b) PES2; (c) PES3. 1 t.u. = 0.01019 ps.

It is possible to determine the major energy transfer pathways and to a lesser extent, the secondary pathways from the results of few trajectories. This is generally not possible for the rate coefficient which requires averaging over results obtained from a large ensemble of trajectories. Previous calculations performed by Pan and Raff[4] indicate that the energy transfer rate coefficient determined from a limited subset of trajectories generally yields a result having the correct order of magnitude. In many cases, the results are accurate to within a factor of 2.

Tables 4.3-6 present a summary of the total relaxation rates for each of the 12 vibrational modes of vinyl bromide in its near equilibrium configuration on PES1, PES2 and PES3 respectively. These rates were computed by fitting Eq. 4.11 to the data obtained from Eq. 4.10. The CH_2 war (ν_4) is the fastest relaxing mode for PES1 and PES3. The CHBr wag (ν_2) is the fastest mode for PES2. For PES1, after ν_4, other modes with relatively large total relaxation rates are ν_3, ν_7, ν_9 and ν_{11}. The slowest relaxing mode for PES1 is the H-C-H bend (ν_8). For PES2, after ν_2, other modes ν_4, ν_5, ν_6 and ν_9 have relatively large total relaxation rates. The slowest relaxing mode for PES2 is the C-H stretch (ν_{11}). For PES3, after ν_4, other modes with significant relaxation rates are ν_2, ν_5, ν_6, ν_7, ν_9 and ν_{10}. The slowest relaxing mode for PES3 is the H-C-H bend (ν_8). The only significant difference between PES1 and PES2 is the curvature of the potential near equilibrium for each of the bonds and angles. These curvature variations produced only 5 to 10% change in the computed fundamental vibrational frequencies on the two surfaces. Yet, these variations produce changes in the mode-to-mode coupling constants that are sufficient to produce an average absolute percent difference between the computed total mode relaxation rate coefficients on PES2 and PES1 of 82%. The most extreme case is

that for relaxation of the CHBr wag (ν_8). The total relaxation rate coefficient for this mode on PES2 is 5.7 times larger than the corresponding value on PES1. It is, therefore, clear that the calculated mode-to-mode IVR rates are a sensitive function of potential curvature near equilibrium. The qualitative nature of the transfer pathways deduced from the envelop functions are much less sensitive.

Table 4.3

Total IVR rate coefficients computed by least-squares fitting of Eq 4.11 to the results obtained using Eq 4.10 for PES1. In each case, 3.0 eV energy in excess of zero-point energy is initially partitioned into the indicated vibrational mode.

Mode i	**$k_i(ps^{-1})$**	**$\alpha_i(ps^{-1})$**	**$<E_i(0)>$ (eV)**	**$<E_\alpha(0)>$ (eV)**
ν_1	8.636	7.949	3.0484	0.2965
ν_2	5.201	6.183	3.0637	0.2907
ν_3	15.996	1.668	3.0644	0.3220
ν_4	20.903	4.612	3.0830	0.3898
ν_5	5.986	6.084	3.0858	0.4236
ν_6	7.556	186.457	3.0889	0.3474
ν_7	17.272	3.729	3.0893	0.3791
ν_8	4.220	1.668	3.0980	0.3254
ν_9	15.505	15.898	3.1111	0.3135
ν_{10}	7.556	7.458	3.1538	0.3410
ν_{11}	13.739	187.144	3.1559	0.4357
ν_{12}	10.010	9.617	3.1568	0.2842

Table 4.4

Total IVR rate coefficients computed by least-squares fitting of Eq 4.11 to the results obtained using Eq 4.10 for PES2. In each case, 3.0 eV energy in excess of zero-point energy is initially partitioned into the indicated vibrational mode.

Mode i	$k_i(ps^{-1})$	$\alpha_i(ps^{-1})$	$<E_i(0)>$ (eV)	$<E_{\alpha}(0)>$ (eV)
ν_1	8.734	88.518	3.0463	0.2179
ν_2	29.637	31.698	3.0603	0.2910
ν_3	8.243	2.257	3.0610	0.2936
ν_4	21.590	4.138	3.0757	0.3818
ν_5	17.076	2.061	3.0779	0.2813
ν_6	18.531	17.861	3.0806	0.2681
ν_7	8.538	1.865	3.0884	0.3051
ν_8	9.715	4.024	3.0942	0.2896
ν_9	10.697	3.140	3.1009	0.2680
ν_{10}	5.496	2.257	3.1385	0.3097
ν_{11}	4.122	0.589	3.1402	0.4165
ν_{12}	8.930	5.790	3.1413	0.3653

Table 4.5

Total IVR rate coefficients computed by least-squares fitting of Eq 4.11 to the results obtained using Eq 4.10 for PES3. In each case, 3.0 eV energy in excess of zero-point energy is initially partitioned into the indicated vibrational mode.

Mode i	$k_i(ps^{-1})$	$\alpha_i(ps^{-1})$	$\langle E_i(0) \rangle$ (eV)	$\langle E_\alpha(0) \rangle$ (eV)
ν_1	9.028	9.519	3.0463	0.2774
ν_2	18.548	18.155	3.0602	0.2819
ν_3	8.243	7.753	3.0610	0.3272
ν_4	48.577	14.132	3.0757	0.3105
ν_5	19.333	83.513	3.0779	0.3200
ν_6	25.417	30.716	3.0806	0.2783
ν_7	12.561	47.203	3.0884	0.3163
ν_8	4.514	0.883	3.0942	0.2858
ν_9	18.548	27.674	3.1009	0.3169
ν_{10}	18.449	25.908	3.1384	0.3118
ν_{11}	5.201	2.061	3.1401	0.1563
ν_{12}	19.823	19.136	3.1413	0.2902

The central focus of this research is to determine to what extent accurate mechanisms, product yields, reaction rates and energy transfer rates can be obtained from more empirical surfaces that fit only reaction channel barrier heights, measured product and reactant equilibrium geometries and fundamental vibrational frequencies and the experimentally determined heats of reaction. Comparison of the results obtained using the *ab initio* potential (PES1) with previously reported calculations[5] that are based on a potential formulated using the above techniques (EPS)[4] permit us to draw to some useful conclusions.

Qualitatively, the energy transfer dynamics are very similar on both PES1 and EPS surfaces. The relaxation times for various modes vary between 0.047 ps to 0.23 ps on PES1. On empirical surface, the range of values is 0.041 ps to 0.15 ps. Examination of the envelop functions of the temporal variations of the mode kinetic energies shows that the energy transfer is not globally rapid relative to the vinyl bromide decomposition rate on either surface.

Table 4.6 gives a more detailed comparison of the calculated total mode relaxation rates with 3.0 eV of excitation energy for the *ab initio* and the EPS surface. The variations of the mode relaxation rate coefficients between the two surfaces is less than 50% for modes ν_1, ν_3, ν_4, ν_7 and ν_9. For modes ν_6, ν_{10}, ν_{11} and ν_{12}, the variation is between a factor of 1.5 to 2.0. The rate coefficients for modes ν_2, ν_5 and ν_8 are a factor of three to four on the empirical surface than on the *ab initio* formulation. These differences are primarily associated with the manner in which the mode-to-mode coupling terms in the potential surfaces are evaluated. For the EPS surface, these coupling terms are empirically chosen with little supporting experimental data. In contrast, the coupling

terms for PES1 are determined from the results of the *ab initio* calculations as described in Chapter II.

In most complex systems, mode relaxation rates can not be experimentally measured. In the most favorable cases, these relaxation rates are obtained with an accuracy that is probably less than a factor of two or three. In view of these facts, we conclude that empirical potential surfaces whose formulation is based upon a limited number of *ab initio* calculations along with experimentally determined activation energies, product and reactant equilibrium geometries and fundamental frequencies and heats of reaction are likely to be sufficiently accurate to ensure that the computed energy transfer rates and pathways are experimentally meaningful.

Table 4.6

Comparison of total IVR rate coefficients on the *ab initio* PES1 and empirical EPS surfaces for the case in which 3.0 eV of excitation energy in excess of zero-point energy is initially partitioned into the indicated mode.

Mode i	**k_i (ps^{-1}) [PES1]**	**k_i (ps^{-1}) [EPS][(a)]**	**$\frac{k_i\ [EPS]}{k_i\ [PES1]}$**
ν_1	8.8	8.7	0.99
ν_2	5.3	15.9	3.00
ν_3	16.3	17.0	1.04
ν_4	21.3	18.6	0.87
ν_5	6.1	24.5	4.02
ν_6	7.7	14.2	1.84
ν_7	17.6	14.2	0.81
ν_8	4.3	17.8	4.14
ν_9	15.8	14.2	0.90
ν_{10}	7.7	13.1	1.70
ν_{11}	14.0	6.5	0.46
ν_{12}	10.2	16.5	1.62

(a) References 3 and 4

References:

1. K. L. Bintz, D. L. Thompson, J. W. Brady, *Chem. Phys. Lett.,* **131**, 398 (1986); Y.Guan and D. L. Thompson, *J. Chem. Phys.*, **88**, 2355 (1988); T. Uzer, J. T. Hynes, W. P. Reinhardt, *Chem. Phys. Lett.,* **117**, 600 (1985); T. Uzer, J. T. Hynes, W. P. Reinhardt, *J. Chem. Phys.,* **85**, 5791 (1986); B. G. Sumpter, D. L. Thompson, *J. Chem. Phys.*, **86**, 2805 (1987), **86**, 3301 (9987); P. R. Stannard, W. M. Gelbart, *J. Phys. Chem.*, **85**, 3592 (1981).

2. L. M. Raff, *J. Chem. Phys.*, **89**, 5680 (1988).

3 (a) H. Okabe, *J. Chem. Phys.* **62,** 2782 (1975); (b) H. Okabe, *J. Chem. Phys.* Ref. Data **11**, 2-101 (1982); (c) L. M. Sverdlov, M. A. Kovner, E.P. Krainov, *Vibrational Spectra of Polyatomic Molecules,*Wiley, New York, 414-426 (1974).

4. S. A. Abrash, R. W. Zehner, G. J. Mains and L. M. Raff, *J. Phys. Chem.* **99**, 2959 (1995).

5. Ran Pan and L. M. Raff, *J. Phys. Chem.* **100**, 8085 (1995).

2

VITA

Asif Rahaman

Candidate for the Degree of

Doctor of Philosophy

Thesis: EFFECTS OF MULTIDIMENSIONAL POTENTIAL-ENERGY SURFACE TOPOLOGY ON THE UNIMOLECULAR DISSOCIATION OF VINYL BROMIDE

Major Field: Chemistry

Biographical:

Education: Graduated from Diamond Harbor High School, Diamond Harbor, West Bengal, India in March, 1988; received Bachelor of Science Degree in Chemistry form Calcutta University, Calcutta, India, in March, 1991 and Master of Science in Chemistry from Indian Institute of Technology, Kanpur, India, in June, 1993. Completed the requirements for the Doctor of Philosophy with a major in Physical Chemistry at Oklahoma State University, Department of Chemistry in July, 2000.

Experience: Research Assistant, Indian Institute of Technology, Kanpur, India, July 1993 to May, 1995; Research Assistant and Teaching Assistant at Oklahoma State University, August, 1995 to May, 2000; Research Assistant in Department of Chemical Engineering from May, 2000 to July, 2000.

Professional Membership: Phi Lambda Upsilon
American Chemical Society